

BIOINSPIRED NANOPARTICLES FOR NEAR INFRARED BIOMEDICAL IMAGING

Ph.D. Thesis

By

SUMAN BISHNOI



**DEPARTMENT OF BIOSCIENCES AND BIOMEDICAL
ENGINEERING
INDIAN INSTITUTE OF TECHNOLOGY
INDORE**

AUGUST 2021

BIOINSPIRED NANOPARTICLES FOR NEAR INFRARED BIOMEDICAL IMAGING

A THESIS

*Submitted in partial fulfillment of the
requirements for the award of the degree*

of
DOCTOR OF PHILOSOPHY

by
SUMAN BISHNOI



**DEPARTMENT OF BIOSCIENCES AND BIOMEDICAL
ENGINEERING
INDIAN INSTITUTE OF TECHNOLOGY
INDORE**

AUGUST 2021



INDIAN INSTITUTE OF TECHNOLOGY INDORE

CANDIDATE'S DECLARATION

I hereby certify that the work which is being presented in the thesis entitled **BIOINSPIRED NANOPARTICLES FOR NEAR INFRARED BIOMEDICAL IMAGING** in the partial fulfilment of the requirements for the award of the degree of **DOCTOR OF PHILOSOPHY** and submitted in the **DEPARTMENT OF BIOSCIENCES AND BIOMEDICAL ENGINEERING, Indian Institute of Technology Indore**, is an authentic record of my own work carried out during the time period from July 2015 to August 2021 under the supervision of Dr. Debasis Nayak, Associate Professor, BSBE, IIT Indore and Dr. Sharad Gupta, Associate Professor, BSBE, IIT Indore

The matter presented in this thesis has not been submitted by me for the award of any other degree of this or any other institute.

Suman
21/06/2021

Signature of the student with date:
(SUMAN BISHNOI)

This is to certify that the above statement made by the candidate is correct to the best of my/our knowledge.

Debasis Nayak
21/6/21

Signature of Thesis Supervisor with date
(DR. DEBASIS NAYAK)

Sharad Gupta
21/6/21

Signature of Thesis Supervisor with date
(DR. SHARAD GUPTA)

SUMAN BISHNOI has successfully given his/her Ph.D. Oral Examination held on 08 July 2022

Debasis Nayak
08.07.22

Signature of Thesis Supervisor with date
(DR. DEBASIS NAYAK)

Sharad Gupta
08/07/2022

Signature of Thesis Supervisor with date
(DR. SHARAD GUPTA)

ACKNOWLEDGEMENTS

The day has finally come when I will pen down this paper. My heart will be forever grateful for the strength and countless blessings I have received from Almighty, as well as the good wishes and support received from my friends and family. From the beginning of this journey, it has been a roller coaster ride for me.

First and foremost, I would like to express my heartfelt gratitude to my mentors Dr. Debasis Nayak and Dr. Sharad Gupta, who plays a magnificent role in transforming my research career and providing kind support in every aspect during my Ph.D. I gained valuable experience working with them through my research and in being a good person. Their support, inspiration, faith, advice, and discussion have enabled me to reach this milestone.

It is my privilege and honor to express my gratitude to my father (Bhakhar Ram Bishnoi), and my mother (Indra Bishnoi), for their sacrifices, support, and encouragement. It would have been impossible to carry out this endeavor without the support of my beloved husband, Mr. Surendra Kumar. In continuing this journey, I owe much to his inspirational and constant drive to realize my potential. In addition to listening to my research findings, he provides constructive critiques from a societal aspect. He helps me become a more positive person through every discussion we have. Thanks to my son Mukund Bishnoi for providing me with a positive environment, relieving me of work stress, and enabling me to learn endlessly every day. My family members made a significant contribution to this thesis. I want to express my deep gratitude to my brother (Ashok Bishnoi), my sister-in-law (Savita) and my niece (Rhea) for their continual moral supports. My father-in-law (Bansi Ram Bishnoi) and My mother-in-law (Vimala) treated me like their daughter and supported me throughout my ups and downs. Without their encouragement and support, it would not be possible to pursue my doctorate.

I would like to acknowledge the Council of Scientific and Industrial Research (CSIR), India, for financial assistance during my Ph.D.

I take this opportunity to thank my PSPC members Dr. Prashant Kodgire and Dr. Srivathsan Vasudevan, for their valuable suggestions and progress evaluation throughout my Ph.D. I thank my research collaborator, Dr. Shantibhusan Senapati, Institute of Life Sciences, Bhubaneswar, for conducting in vivo bioimaging.

A flower necessitates sunlight and air to blossom; likewise, my journey would not be possible without my colleagues. I am extremely thankful to Mr. Anurag Mishra, Dr. Basant Pravas Sahu, Dr. Prativa Majee, Mr. Prashant Kharey, Mr. Ramesh Kumar, Mr. Ritudhawaj Tiwari, Mr. Sanchit Neema, Miss Saumya Jaiswal and Mrs. Shruti Pyasi for creating a positive workplace environment. I like to extend my thanks to my friends Dr. Anshu Kumari and Mr. Subi Sugathan for helping me in my tough times. It is a pleasure to have the support of Ms. Sheeba Rehman, Mr. Prajwal Kinake, Mr. Vishal Jain, Dr. Tejendra Dixit, and Ms. Kalpana Kumari. Anytime I needed, they were there to help, whether it be assisting me in performing experiments or sharing valuable insights. I would further thank Dr. Surjendu Bikas Dutta and Mr. Soumya Kanti De for sharing their valuable knowledge of techniques and scientific discussions. It is giving me immense pleasure to thank Dr. Tridib Sarma and Dr. Neha Thakur for helping me during dynamic light scattering (DLS) measurements. I want to acknowledge the Sophisticated Instrumentation Center (SIC) at the Indian Institute of Technology Indore (IITI). In addition, I wish to acknowledge Dr. Ravindra Kumar and Mr. Kinny Pandey for their support in the provision of characterization facilities.

My most sincere thanks also go to the Head and DPGC convener of the Department of Bioscience and Biomedical Engineering, IIT Indore, for their encouragement and support throughout my Ph.D. journey. I am extremely grateful to all faculties of BSBE for their contributions to gain new insight into my research through various courses taught during my course work.

My thanks extend to all the members of the Department of Biosciences and Biomedical Engineering. Mr. Arif Patel, Mr. Murphy B Ganveer and Mr. Gaurav Singh for their supportive nature. Sincere gratitude to Dr. Shilpa and the health center staffs at IITI for caring for my health conditions during my doctoral studies. Last but not least, I wish to thank staff members of IITI for providing comfort and convenience during my Ph.D. In addition to this, several people contributed either directly or indirectly to completing this successful journey. I wish I could thank everyone, but time and space constrain me.

Suman Bishnoi

DEDICATION

*This thesis is dedicated to my
family members*

SYNOPSIS

The visualization and detection of deeply buried biological features at cellular size remains a major clinical challenge in disease diagnosis. In this regard, molecular imaging represents the upcoming advancement in biomedicine as it enables real-time visualization and characterization of physiological processes at both cellular and molecular levels. Unfortunately, the conventional imaging modalities routinely used in clinics, such as ultrasound, X-ray computed tomography, magnetic resonance imaging, etc., fail to address the aforementioned challenges. Despite offering a high penetration depth throughout the tissue, these techniques have a low spatial resolution, especially in soft tissue. As a result, identifying small tumor masses developed at the initial stage of cancer remains below their threshold value. On the other hand, the optical imaging techniques offer a high spatial resolution, enables visualization of the biological processes at the subcellular level; though, they are not suited for deep-tissue penetration. Nonetheless, the optical imaging in the near-infrared (NIR) region promises high spatial resolution and deeper penetration depth due to low endogenous absorption, low photon scattering, and negligible autofluorescence from the surrounding tissue. Therefore, NIR fluorescence imaging enabling high spatial resolution is advantageous for early-stage disease diagnosis and other biomedical applications. In this direction, several NIR active exogenous contrast agents such as quantum dots, carbon nanotubes, semiconducting polymers, and small-molecule organic dyes have been developed during the last few years. However, the applications of these exogenous contrast agents in optical imaging are limited due to their cytotoxicity and other unfavorable attributes. Therefore, using a biocompatible NIR active contrast agent for optical imaging is crucial for disease diagnosis and treatment. Indocyanine green (ICG) is the United States Food and Drug Administration (FDA) approved NIR active dye used in clinics for the last 60 years. The ICG facilitates deep tissue optical visualization as it has excitation and emission wavelengths in the NIR range (780/810 nm), as shown in **Fig. a**. Despite having suitable optical properties, free ICG has not been used to the fullest for biomedical applications due to its poor

optical stability, concentration-dependent aggregation, photo- and thermal-degradation and short circulation time in the body. These limitations of ICG could be overcome by encapsulating it within the nanoparticles (NPs), which will enhance its optical stability. Therefore, the development of an efficient nanocarrier is an utmost need for the site-specific delivery of an optically active form of ICG.

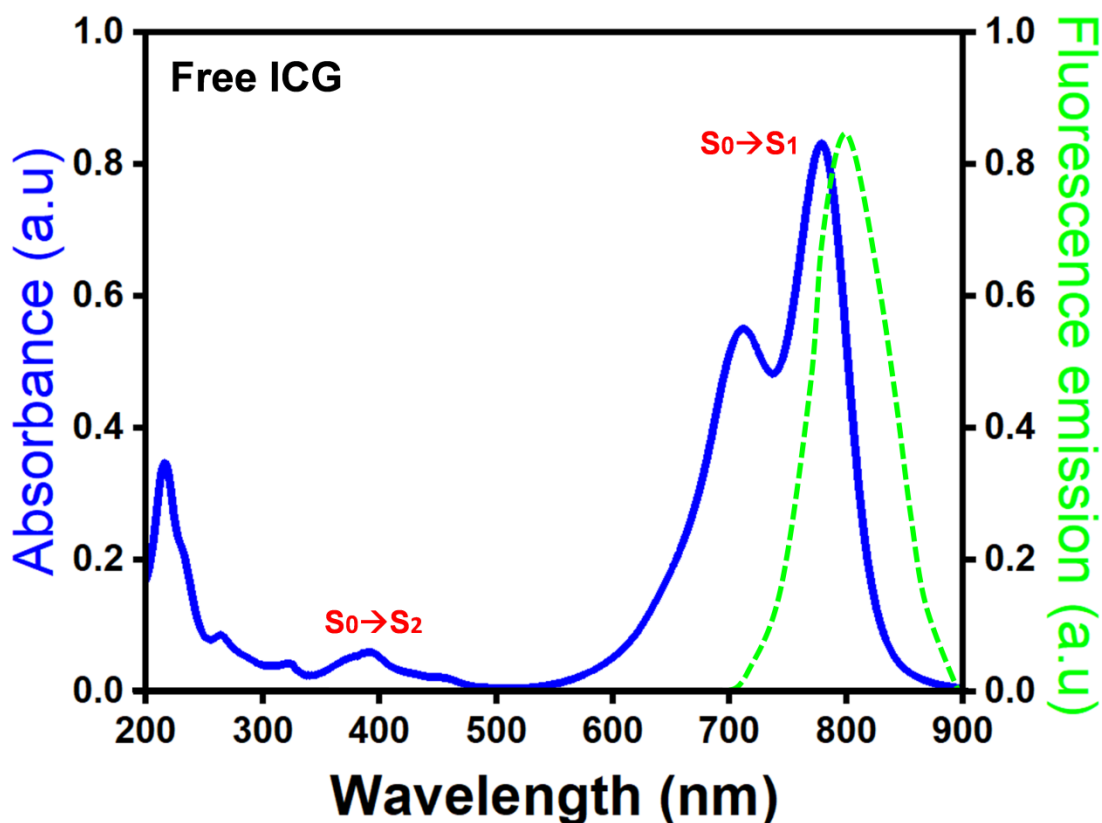


Figure a. The absorption and emission spectrum of ICG) dye, depicting its ground state (S_0), first singlet excited state (S_1) and second singlet excited state (S_2).

In this regard, bio-nanotechnology offers excellent prospects by bridging the gap between medicine and engineering to advance disease diagnosis and therapy. This emerging field enabled the synthesis and functionalization of NPs for various

biomedical applications such as bioimaging, drug delivery, treatment, etc. The significance of the NPs delivery system lies in the potential of reducing side effects of the contrast agent by targeting specific cells, protecting them from premature degradation, enhancing solubility, and showing sustained and controlled release. In recent years, a wide range of synthetic NPs such as liposomes, polymers, metallic, and protein-based NPs are being explored for bioimaging and therapeutics. However, these NPs are restricted by their structural heterogeneity, potential immunogenicity, instability, low delivery efficiency, rapid clearance, and toxicity. Thus, to make a clinical impact, there is a need to engineer biocompatible and biodegradable NPs for their use as a drug delivery system (DDS). Motivated by nature that uses vesicles for transportation from one cell to another, the concept of vesicles as a DDS is explored and implemented to develop synthetic and biomimetic vesicles. Interestingly various delivery systems mimicking vesicular structures, such as liposomes, niosomes, exosomes, cell membrane-derived, and bacterial outer membrane-based vesicles, have been exploited as therapeutic modalities for biomedical applications. Moreover, the liposomal product, Doxil, has been approved and successfully used for the treatment of Kaposi's sarcoma and ovarian cancer. However, the instability of phospholipids, high production cost, and requirement of special storage conditions limit the usage of liposomes as a DDS. Furthermore, the virus structural protein based nanovesicles can also be employed as a DDS to deliver cargoes to specific cells or tissues as they are naturally evolved to enter and deliver genetic material into host cells. Also, the ease of customization and structural tailoring ability make viruses/virus-like structures the preferred choice for the delivery application. In addition, such structural engineering and quality control could not be achieved using synthetic NPs.

In this direction, this thesis focuses on fabricating novel bioinspired vesicular nanopatform encapsulating ICG for deep tissue bioimaging, as shown in **Fig. b**. Here, non-ionic surfactant-based synthetic niosomes and biomimetic vesicular stomatitis virus glycoprotein (VSV-G) based viral nanoparticles (VNPs) are fabricated and exploited as a novel platform for ICG encapsulation. The fabricated nanoparticles ICGNiosomes (ICGNios) and NIR active viral nanoconstructs (NAVNs) improved optical stability, cellular uptake, and circulation half-life of ICG. Also, ICG loaded

NIR active nanoparticles are biocompatible and enabled deep tissue *ex vivo* and *in vivo* NIR imaging. Subsequently, NAVNs are exploited further for deep tissue multiphoton bioimaging using the nonlinear excitation properties of ICG. The two-photon excitation fluorescence (TPEF) imaging using NAVNs provides better spatial resolution and visualization of the cellular microstructure of chicken breast tissue. Thus, NAVNs encapsulating ICG hold excellent promise for deep-tissue NIR and multiphoton imaging in clinical and preclinical studies.

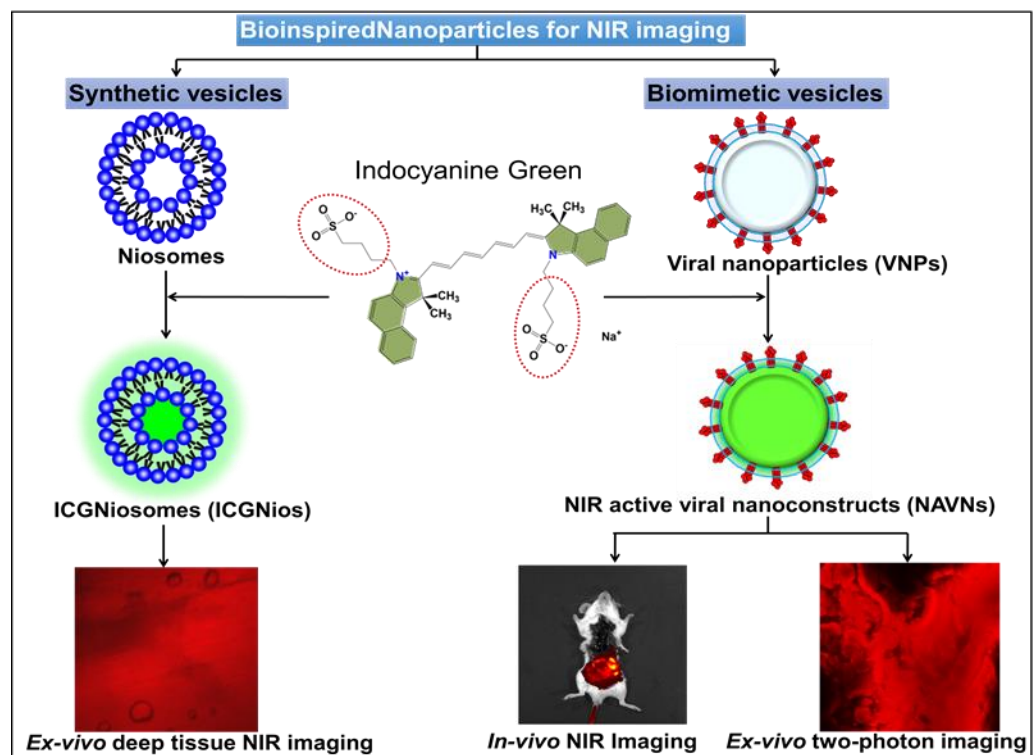


Figure b. Fabrication of bioinspired synthetic niosomes and biomimetic viral nanoparticles (VNPs) to encapsulate NIR active ICG for deep tissue bioimaging.

This thesis aims to contribute to bioimaging techniques and diagnostics by enhancing the optical properties of NIR-active ICG dye via encapsulation within biologically inspired nanoparticles. Here in this study, the bioinspired synthetic

niosomes and biomimetic viral nanoparticles are used to encapsulate ICG and are evaluated for their performance for deep tissue NIR and multiphoton imaging. This thesis is divided into six chapters, as summarized below:

Chapter 1 gives a general introduction to the conventional imaging modalities and the significance of the NIR optical imaging technique for early-stage disease diagnosis. Afterwards, a comprehensive discussion of the importance of NIR exogenous contrast agents for high-sensitive deep tissue imaging is provided. Subsequently, this chapter details the importance and limitation of the US FDA-approved NIR dye ICG for deep tissue imaging. Additionally, a brief discussion of the available nano constructs for encapsulating ICG has been provided. This chapter further describes the importance of bioinspired synthetic niosomes NPs, and biomimetic vesicular stomatitis virus (VSV) based VNPs as a nanocarrier for encapsulation of ICG to overcome its limitation and to facilitate considerable advancement to deep tissue imaging for diagnostics.

Chapter 2 describes the materials and methods used for the research work. This chapter explains the details of nanoparticle fabrication, characterization, *ex vivo* imaging, *in vivo* animal studies, and specifications of the instruments used for experimental measurements.

Chapter 3 describes the fabrication of novel NIR active synthetic niosomes for deep tissue bioimaging. ICG is a clinically approved NIR contrast agent used in medical diagnosis. However, ICG has not been used to its fullest for biomedical imaging applications due to its aqueous instability, concentration-dependent aggregation, low fluorescence quantum yield, photo and thermal degradations leading to quenching of its fluorescence emission. This chapter presents a bioinspired synthetic niosomal formulation, ICGNiosomes (ICGNios), that encapsulates and protects ICG from degradation. Interestingly, the ICGNios exhibited high fluorescence emission and absorbance with a bathochromic shift at a longer wavelength than free ICG. Moreover, ICGNios displayed an anti-aggregation mechanism even at a higher

concentration of ICG. Additionally, ICGNios nanoparticles are biocompatible and biodegradable and readily uptaken by the cells. Furthermore, ICGNios show enhanced fluorescence signal and clear tissue architecture through ~1 cm thick chicken breast tissue than free ICG. The overall results suggest that ICGNios could offer a promising platform for high contrast deep tissue *in vivo* imaging to visualize inaccessible tissue microstructures for disease diagnosis and therapeutics.

Chapter 4 explores the fabrication of bioinspired and biomimetic viral nanoparticles (VNPs) encapsulating ICG for *in vivo* bioimaging. The viruses are naturally evolved to gain access to the host cells to deliver their genetic material bypassing the endosomal mediated degradation of the payload. Therefore, for efficient cellular uptake and faster intracellular delivery of theranostic agents, VNPs are best suited as an effective drug delivery system (DDS). As a proof-of-concept, we bioengineered the vesicular stomatitis virus glycoprotein (VSV-G)-based NIR active viral nanoconstructs (NAVNs) encapsulating ICG for NIR bioimaging. The NAVNs are nano-size membrane-bound spherical vesicles having intrinsic cellular-fusogenic properties of VSV-G. Additionally, *in vitro* and *in vivo* cytotoxicity studies showed the biocompatibility and safety of VSV-G VNPs for its use as a delivery platform for biomedical applications. Further, NIR imaging displayed higher fluorescence emission in NAVNs treated cells than free ICG treated cells, suggesting enhanced cellular uptake and delivery of ICG by NAVNs. Moreover, the *in vivo* biodistribution study of ICG loaded NAVNs in BALB/C mice showed that NAVNs enhanced circulation and retention time of ICG for two days. The overall findings highlight the effectiveness of VSV-G-based VNPs as an efficient nanocarrier for NIR fluorescence imaging.

Chapter 5 presents the use of fabricated VSV-G-based NAVNs for two-photon deep-tissue bioimaging. The two-photon excited (TPE) fluorophores require simultaneous excitation by two photons of the NIR range for deep tissue penetration and to obtain optical images with high spatial resolution. ICG is the only FDA-approved NIR contrast agent exhibiting the second excited singlet (S_2) state mediated

two-photon excitation property, which is advantageous for two-photon bioimaging. In this chapter, the two-photon fluorescence imaging efficacy of ICG loaded NAVNs is demonstrated in *in vitro* and *ex vivo* models. The two-photon *in vitro* imaging displayed superior contrast in the cells incubated with NAVNs, suggesting their efficient binding and cellular uptake compared to the free form of ICG. Additionally, two-photon *ex vivo* imaging using NAVNs enables visualization of clear cellular microstructures in chicken breast tissue up to ~350 μm tissue depth. This study suggests that NAVNs displaying superior fluorescence emission in two-photon imaging could be an ideal contrast agent for deep tissue high-resolution imaging for disease diagnosis.

Chapter 6 summarizes the significant findings of this thesis and presents the future perspective of this work towards clinical applications.

LIST OF PUBLICATIONS

(A) Publications from Ph.D. thesis work:

A1. In Refereed Journals: 3

1. **Bishnoi, S.**; Tiwari, R.; Gupta, S.; Byrareddy, S.; Nayak, D. Oncotargeting by Vesicular Stomatitis Virus (VSV): Advances in Cancer Therapy. *Viruses* 2018, 10 (2), 90. <https://doi.org/10.3390/v10020090>. (IF 5.048)
2. **Bishnoi, S.**; Kumari, A; Rehman, S; Minz, A; Senapati, S; Nayak, D; Gupta, S. Fusogenic Viral Protein-based Near-infrared Active Nanocarriers for Biomedical Imaging. *ACS Biomaterials Science & Engineering* 2021, <https://doi.org/10.1021/acsbomaterials.1c00267>. (IF 4.749)
3. **Bishnoi, S.**; Rehman, S; Dutta, S; De, SK; Chakraborty, A; Nayak, D; Gupta, S. Optical property enhancing novel near-infrared active niosomes nanoformulation for deep tissue bioimaging. *ACS Omega* 2021, 6, 35, 22616–22624. <https://doi.org/10.1021/acsomega.1c02632> (IF 3.512)

A2. Patent: 1

4. **Bishnoi, S.**; Kumari, A; Gupta, S; Nayak, D. ‘Near-infrared fluorescence-based bioimaging, Method and composition thereof’; App. Number 202021051280. (Published)

A3. Unpublished Work: 2

5. **Bishnoi, S.**; Kumari, A; Rehman, S; Nayak, D; Gupta, S. Membrane Fusogenic Viral protein based Near-infrared active Theranostic Agent for Deep Tissue Two-photon bioimaging. (Under preparation)
6. **Bishnoi, S.**; Rehman, S; Dutta, S; Nayak, D; Gupta, S. Anti-quenching near infrared active niosomes for high contrast optical imaging. (Under preparation)

(B) Other publications during Ph.D.:

B1. In refereed Journals: 3

7. Roy, A.; Srivastava, M.; Saqib, U.; Liu, D.; Faisal, S. M.; Sugathan, S.; **Bishnoi, S.**; Baig, M. S. Potential Therapeutic Targets for inflammation in Toll-like Receptor 4 (TLR4)–Mediated Signaling Pathways. *Int. Immunopharmacol.* 2016, 40, 79–89. <https://doi.org/10.1016/j.intimp.2016.08.026>. (IF 4.932)
8. Thakur, N.; Sharma, B.; **Bishnoi, S.**; Mishra, S.; Nayak, D.; Kumar, A.; Sarma, T. K. Multifunctional Inosine Monophosphate Coordinated Metal-Organic Hydrogel: Multi-Stimuli Responsiveness, Self-Healing Properties and Separation of Water from Organic Solvents. *ACS Sustain. Chem. Eng.* 2018. <https://doi.org/10.1021/acssuschemeng.8b00963>. (IF 8.198)
9. Thakur, N.; Sharma, B.; **Bishnoi, S.**; Jain, S.; Nayak, D.; Sarma, T. K. Biocompatible Fe³⁺ and Ca²⁺ Dual Cross-Linked G-Quadruplex Hydrogels as Effective Drug Delivery System for PH-Responsive Sustained Zero-Order Release of Doxorubicin. *ACS Appl. Bio Mater.* 2019, 2, 3300–3311. <https://doi.org/10.1021/acsabm.9b00334>.
10. Jaiswal S.; Roy R.; Dutta SB.; **Bishnoi S.**; Kar P.; Joshi A.; Nayak D.; Gupta S. Role of Doxorubicin on the Loading Efficiency of ICG within Silk Fibroin Nanoparticles. *ACS Biomaterials Science & Engineering.* <https://doi.org/10.1021/acsbiomaterials.1c01616>. (IF 4.749)
11. Emerging Biomedical Applications of the Vesicular Stomatitis Virus Glycoprotein. Rehman S.; **Bishnoi S.**; Roy Rajarshi.; Kumari Anshu.; Harikrishnan J, Gupta S.; Kar P.; Pattnaik AK and Nayak D*. Manuscript ID: ao-2022-03517c. (Under Review) (IF 3.512)

TABLE OF CONTENTS

ACKNOWLEDGEMENTS	i
LIST OF PUBLICATIONS	xv
LIST OF FIGURES	xxiii
LIST OF TABLES	xxx
ABBREVIATIONS	xxxiii
NOMENCLATURE	xxxvii
Chapter 1	1
Introduction	1
1.1 Conventional clinical bioimaging modalities	1
1.1.1 Positron emission tomography (PET)/Single-photon emission computed tomography (SPECT)	1
1.1.2 Computer tomography (CT)	2
1.1.3 Magnetic resonance imaging (MRI)	2
1.1.5 Emerging preclinical modalities	5
1.2 Importance of near-infrared (NIR) imaging	5
1.3 Importance of ICG for NIR imaging	7
1.3.1 Structure of ICG	7
1.3.2 Optical properties of ICG	8
1.3.3 Aggregation of ICG in aqueous solution	9
1.4 Biomedical imaging applications of ICG	11
1.4.1 NIR photoacoustic (PA) imaging	12
1.4.2 NIR fluorescence (NIRF) imaging	13
1.4.3 Multimodal imaging	14
1.4.4 Multiphoton bioimaging	16
1.5 Shortcomings of ICG	17
1.6 Nanoencapsulation of ICG	17

1.7 Bioinspired nanoparticles	19
1.8 Aim of the thesis	20
1.9 Thesis organization	21
Chapter 2	23
Materials, Methods, and Instrumentations	23
2.1 Introduction	23
2.2 Materials	23
2.3 Methods	24
2.3.1 Niosome preparation	24
2.3.2 Encapsulation efficiency estimation of ICG within Niosomes	24
2.3.3 Morphological characterization	25
2.3.4 Spectroscopic investigation	25
2.3.5 Fluorescence quantum yield calculation (Φ_s)	26
2.3.6 Photostability study	26
2.3.7 Storage stability study	27
2.3.8 Cell culture	27
2.3.9 MTT assay	27
2.3.10 In vitro NIR bioimaging using free ICG and ICGNios	28
2.3.11 Ex vivo NIR imaging for tissue depth penetration	28
2.3.12 Construction of plasmid and bacterial strain	28
2.3.13 Cell culture and VNPs purification	29
2.3.14 Western blot analysis	29
2.3.15 Fabrication of NAVNs	30
2.3.16 Quantification of EE	30
2.3.17 Morphological characterization	30
2.3.18 Spectroscopic analysis	30
2.3.19 Photostability study of NAVNs	31
2.3.20 In vitro release study of NAVNs	31
2.3.21 VSV-G VNPs cellular uptake assay	31
2.3.22 MTT assay	31

2.3.23 NIRF bioimaging	32
2.3.24 VSV isolation	32
2.3.25 Plaque assay	32
2.3.26 Determination of immune response gene expression by quantitative real-time PCR (qRT-PCR)	33
2.3.27 Animal experiment and histopathological Evaluation	34
2.3.28 In vivo NIR imaging and biodistribution study	34
2.3.29 Spectroscopic analysis	34
2.3.30 Two-photon excitation (TPE) fluorescence imaging of free ICG and NAVNs treated HeLa cells	35
2.3.31 TPE fluorescence imaging of chicken breast tissue	35
2.4 Instrumentation and techniques	36
2.4.1 Western blotting	36
2.4.2 Quantitative real-time polymerase chain reaction (qRT-PCR)	37
2.4.3 UV-Vis-NIR absorption spectroscopy	39
2.4.4 Fluorescence spectroscopy	40
2.4.5 Dynamic light scattering (DLS) spectroscopy	42
2.4.6 Field-emission scanning electron microscopy (FESEM)	44
2.4.7 Transmission electron microscopy (TEM)	45
2.4.8 Fluorescence microscopy	46
2.4.9 Multiphoton fluorescence microscopy	48
2.4.10 Cell culture	50
2.4.11 Plaque assay	51
2.4.12 MTT assay	52
Chapter 3	55
Optical Property Enhancing Novel Near-infrared Active Niosomes Nanoformulation for Deep Tissue Bioimaging	55
3.1 Introduction	55
3.2 Results and discussions	57
3.2.1 Morphological characterization of Niosomes and ICGNios	58
3.2.2 Encapsulation efficiency (EE) of ICGNios	59
3.2.3 Biochemical characterization of free ICG and ICGNios	60

3.2.4 Excitation Emission Matrix (EEM) of ICGNios	62
3.2.5 Interaction of ICG with the individual components of niosomes	63
3.2.6 Spectral characteristics of ICGNios encapsulating high concentration of ICG	64
3.2.7 Optical and storage stabilities of ICGNios	65
3.2.8 Biosafety of ICGNios	66
3.2.9 In vitro NIR bioimaging using ICGNios	67
3.2.10 Ex vivo deep tissue NIR imaging	68
3.3 Summary	69
Chapter 4	71
Fusogenic Viral Protein-Based Near-Infrared Active Nanocarriers for Biomedical Imaging	71
4.1 Introduction	71
4.2 Results and discussions	73
4.2.1 Morphological characterization of VNPs and NAVNs	75
4.2.2 Encapsulation efficiency	77
4.2.3 Biochemical characterization	77
4.2.4 Photostability comparison between free ICG and NAVNs	78
4.2.5 In vitro release study of ICG	79
4.2.6 Cellular uptake of VNPs	81
4.2.7 In vitro cellular toxicity and uptake study	82
4.2.8 Innate immune response study of NAVNs	83
4.2.9 In vivo cytotoxicity study of VSV-G VNPs	85
4.2.10 In vivo biodistribution of NAVNs	86
4.3 Summary	88
Chapter 5	89
Membrane Fusogenic Viral Protein-based Fluorescent Nanocarrier for Two-Photon Bioimaging	89
5.1 Introduction	89
5.2 Results and discussions	91

5.2.1 Spectroscopic analysis of NAVNs	91
5.2.2 In vitro TPE fluorescence imaging using NAVNs	93
5.2.3 Ex vivo TPE fluorescence imaging of chicken breast tissue	94
5.2.4 Z-stack of TPE fluorescence imaging of NAVNs treated chicken breast tissue	96
5.3 Summary	97
Chapter 6	99
Conclusion and Scope of Future Work	99
6.1 Conclusion	99
6.2 Scope of Future Work	101
Appendix A	105
References	107

LIST OF FIGURES

Figure 1.1 A comparison of the depth of penetration and resolution of current biomedical imaging techniques. PET, positron emission tomography; SPECT, Single-photon emission computed tomography; CT, computed tomography; MRI, magnetic resonance imaging; US, ultrasound; PAI, photoacoustic imaging, OCT, optical coherence tomography.[15].....3

Figure 1.2 Imaging modalities using distinct wavelength of electromagnetic spectrum. MRI, PET, SPECT, CT, NIR near-infrared, PA: photoacoustic, OCT.[22]4

Figure 1.3 The absorption spectrum of light with wavelengths of around 650-900 nm depicts the tissue optical window for deeper penetration due to minimal absorption in this range by the biological components HbO₂, Hb, and H₂O.....6

Figure 1.4 Chemical structure of ICG dye. The ICG comprises two hydrophobic polycyclic rings (benzindotricarbocyanin) linked by carbon chains, each containing a sulfate group (blue dotted box) linked by carbon chain, making it hydrophilic.8

Figure 1.5 Absorption ($\lambda_{\max(ab)} = 780 \text{ nm}$) and emission spectra ($\lambda_{\max(em)} = 810 \text{ nm}$) of ICG dye in water.9

Figure 1.6 Illustration of the absorption (blue) and fluorescence (pink) spectra of H-aggregates arranged in “head-to-head” orientation and J- aggregates associated in “head-to-tail” orientation formed by ICG monomers.....11

Figure 1.7 Schematic of NIR photoacoustic (PA) imaging. A pulse of laser is used to irradiate the chromophore-tagged biological tissue, causing it to produce ultrasonic waves originating from photo absorbers based on thermoelastic expansion. An ultrasound transducer detects the signal that is used to form images of tissue structures.....13

Figure 1.8 Overview of ICG as a potential agent for multimodal imaging applications. MRI: magnetic resonance imaging, CT: computed tomography, PA: photoacoustic, SPECT: Single-photon emission computed tomography, FL: fluorescence US: ultrasound..... 15

Figure 1.9 Mechanism of NIR two-photon excited (λ_{ex} 790 nm and λ_{em} 575-630 nm) ICG dye for multiphoton bioimaging..... 17

Figure 1.10 Different surface modifications and functionalization strategies used to load or conjugate ICG to a variety of nanostructures, such as silicon, micelles, liposomes, nanogel, carbon nanotubes, albumin-based, polymer-based, lipid-based nanoparticles. 19

Figure 1.11 A schematic representation depicting different bioinspired and biomimetic drug delivery systems fabricated by synthetic (lipids, calcium phosphate, hydrogel) and biologically derived (cell, virus, bacteria, fungus, biomacromolecules) materials..... 20

Figure 2.1 Schematic illustration of western blotting technique. For the western blotting technique, the desired purified protein is separated by gel electrophoresis according to its molecular mass. The proteins are transferred from the SDS gel onto a membrane. Afterward, the membrane with proteins is incubated with the gene specific primary antibody followed by HRP tagged secondary antibody The secondary antibody catalyzes an enzymatic reaction with the substrate, which is detectable through a digital imager..... 37

Figure 2.2 A schematic depicting the qRT-PCR principle. The template RNA is converted to cDNA by reverse transcriptase and amplified using PCR by denaturation of cDNA at 95 °C, annealing the primers and probe to the denatured cDNA at 60 °C followed by the final extension at 72 °C. The RNA is quantified by the intensity of fluorescent signals produced during amplification of cDNA..... 38

Figure 2.3 Ray diagram depicting the working of the absorption spectroscopy. The absorption spectrophotometer uses a light source and an excitation monochromator to select a specific wavelength of light that hits the sample. The sample reflects or transmits light. A detector is used to detect the intensity of light transmitted or reflected.....39

Figure 2.4 Schematic depiction of the fluorescence spectroscopy setup. The spectrofluorometers consist of light sources, monochromators, optical filters, and detectors to record fluorophore's excitation and emission spectra.....42

Figure 2.5 Schematic of the working principle of DLS for particle size information. The sample contained in a cuvette is illuminated with a laser. Interaction with the sample scatters incident light in every direction. At a certain angle, the scattered light is detected which is used to calculate the particle size and diffusion coefficient.....44

Figure 2.6 Ray diagram of working principle of the FESEM. FESEM produces images of specimens using a focused beam of electrons. A primary electron beam generates secondary electrons and backscattered electrons as it strikes the sample. Detectors capture these electrons and produce signals to create images of the sample.45

Figure 2.7 Schematic of working principle of typical TEM system. In TEM, electrons are transferred from a gun to the sample, providing a broad or focused beam of light. The ray diagram illustrates the illumination system located above the sample. The stage and objective lens are central components, along with the intermediate and projector lenses.46

Figure 2.8 Schematic of working principle of fluorescence microscope. An inverted setup using mercury and xenon lamps is shown. In a typical experimental design, the excitation light is centered on the backside of the aperture of the lens to produce uniform light distribution within the sample. The fluorescence emission is collected using an objective lens, uncoupled from excitation light with a dichroic mirror, and imaged using detector (CCD camera).....48

Figure 2.9 Schematic of an Olympus confocal laser scanning microscope equipped with a MaiTai laser for multiphoton bioimaging. The acronym is AOM: Acoustic optical modulator, DM: Dichroic mirror, RXD1: BA420-460nm, RXD2: BA 495-540, RXD3: BA380-560nm, and RXD4 BA575-630nm. 50

Figure 2.10 Illustration of a plaque assay method for virus quantification. This assay involves infecting host cells with varying dilutions of a virus particles, and covering it using semisolid media, like agar, for preventing indiscriminate spreading of virus. 52

Figure 2.11 Graphic illustration of the principle of MTT assay. MTT involves the reduction of tetrazolium salts to formazan crystals by viable cells, where the number of cells directly correlates with the optical density. 53

Figure 3.1 Schematic representation of the preparation of niosomes and ICGNios by thin-film hydration method. Tween 80, Span 80, and cholesterol are dissolved in chloroform followed by the formation of thin-film by evaporating chloroform using rotary evaporation at 37 °C. Niosomes and ICGNios are fabricated by hydration of the thin-film of non-ionic surfactants using DI water and ICG dissolved in DI water. 58

Figure 3.2 Morphological characterizations of niosomes and ICG Niosomes (ICGNios). (a) Scanning electron microscopy (SEM) image of niosomes, (b) SEM image of ICGNios (c) Transmission electron microscopy (TEM) image of ICGNios. Scale bar 200 nm. (d-e) Dynamic light scattering (DLS) measurement of niosomes and ICGNios depicting hydrodynamic diameter (Dh) and polydispersity index (PDI) of niosomes and ICGNios. 59

Figure 3.3 Biochemical characterizations of free ICG, niosomes, and ICGNiosomes (ICGNios). (a) Absorption spectra of free ICG, niosomes, and ICGNios. (b) The fitted absorption spectrum of ICGNios with R²=99.86%. (c) The fitted absorption spectrum of free ICG with R²=99.43%. (d) Fluorescence emission spectra of free ICG, niosomes, and ICGNios. All fluorescence spectra were smoothed. 62

Figure 3.4 Excitation-emission matrix (EEM) of (a) Free ICG (3 μM), (b) ICGNios constituting 3 μM ICG and (c) Niosomes.63

Figure 3.5 Spectroscopic characterization of individual components of niosomes (Span 80, tween 80 and cholesterol) with ICG. (a) Digital photographs of free ICG, cholesterol/ICG, tween 80/ICG and span 80/ICG blends. (b) Absorption spectra of free ICG, tween 80/ICG and span 80/ICG. (c) Fluorescence emission spectra of free ICG, tween 80/ICG and span 80/ICG.....64

Figure 3.6 Antiquenching spectral characteristics of ICGNios compared to free ICG. (a) Absorption spectra and (b) fluorescence emission of free ICG and ICGNios constituting equivalent concentrations (80 μM and 100 μM) of ICG.....65

Figure 3.7 Photostability and storage stability of the ICGNios vs. free ICG. a) Photostability (%) of ICGNios and free ICG under exposure of ambient light at room temperature. (b) Storage stability (%) of ICGNios and free ICG incubated at 4 $^{\circ}\text{C}$ in the dark condition.....66

Figure 3.8 Biocompatibility and NIR imaging of niosomes, ICGNios, and free ICG in Hela cells (a) MTT assay of niosomes and ICGNios; where PC is positive control (b) Fluorescence imaging of Hela cells; The DAPI staining nuclei are shown in blue colour, and ICG fluorescence emission is displayed in red colour. Scale bar: 20 μm and (c) Mean fluorescence emission intensity plot of control, free ICG and ICGNios.68

Figure 3.9 Ex vivo deep tissue enhanced NIR imaging of chicken breast tissue of ICGNios vs. free ICG. (a) Picture of capillary tubes filled with water, free ICG, and ICGNios placed over chicken tissue sample with the thickness of ~ 1 cm (b) Bright field and NIR bio bioimaging of CT filled with water, free ICG and ICGNios (column 1 and 2) and chicken breast tissue with CT filled with water, free ICG and ICGNios (column 3 and 4). Scale bar 100 μm . (c) Mean fluorescence intensity plot of chicken breast tissue placed beneath the CT filled with water, free ICG and ICGNios.69

Figure 4.1 Schematic of bioengineering of VNPs and fabrication of NAVNs. (a) VSV-G gene cloned in pCAG mammalian expression vector. (b) Transformation and amplification of plasmid in DH5 α . (c) Transfection of pCAG-VSVG in HEK293T cells. (d) VNP pellet after final purification by ultracentrifugation. (e) Western blot analysis for detection of VSV-G protein using an anti-VSVG polyclonal antibody. (f) Fabrication of NAVNs by incubation of VNPs with ICG; inset: chemical structure of ICG where the sulfonate group is circled in dotted red color and the polycyclic ring is highlighted by yellow color. 75

Figure 4.2 Morphological characterization of VNPs and NAVNs. (a and d) TEM image of VNPs and NAVNs. (b and e) Dynamic light scattering (DLS) of VNPs and NAVNs with an average diameter of 175 and 180 nm with a polydispersity of 0.258 and 0.236. (c and f) Zeta potential of VNPs and NAVNs. 77

Figure 4.3 Biochemical characterization, photostability, and drug release study of free ICG and VSV-G-based nanoconstructs. (a) Absorption spectra of water, free ICG (9 μ M), VNPs (10 μ g/mL), and NAVNs displaying a reduction in absorption peak in NAVNs. (b) Emission spectra of water, free ICG (9 μ M), VNPs (10 μ g/mL), and NAVNs with a reduction in fluorescence emission of NAVNs. (c) Photostability study of free ICG and NAVNs for 72 h shows ~60% optically active ICG encapsulated within VNPs in comparison with less than 20% of free ICG. (d) Drug release behavior of NAVNs for 24 h depicting the controlled release pattern of ICG. 80

Figure 4.4 Cellular uptake of VSV-G VNPs by HeLa cells detected by immunofluorescence assay using the VSV-G polyclonal primary antibody and FITC-tagged secondary antibody. The Hoechst staining nuclei are displayed in blue color, and FITC emission is displayed in green color. Scale bar: 5 μ m and magnification 10 \times 81

Figure 4.5 (a) In vitro cytotoxicity study showing the biocompatibility of VSV-G-based nanoconstructs in HeLa cells incubated with different concentrations of VNPs and NAVNs for 24 h. (b) NIR images of HeLa cells incubated with free ICG (3 μ M) and

NAVNs (equivalent to free ICG) for 4 h displaying the high cellular uptake of NAVNs. The Hoechst staining nuclei are displayed in blue color, and ICG emission is displayed in red color. Scale bar: 20 μm and magnification 40 \times . (c) Fluorescence emission intensity plot of NIR images of HeLa cells treated with ICG and NAVNs (equivalent to free ICG) depicting ~ 1.5 -fold enhancement in fluorescence intensity in NAVN-treated cells than free-ICG-treated cells.83

Figure 4.6 Relative immune gene expression of IFN β , IFN γ , and IRF3 in NIH/3T3 cells treated with wild-type VSV and NAVNs for 24 h depicting a negligible immune response by bioengineered VSV-G VNPs. Normalization of all samples was done by the housekeeping gene β -actin.84

Figure 4.7 (a) Histopathology study of mice injected with control (PBS) and VNPs (1 mg/kg) at different time points showing the normal architecture of H&E-stained visceral organs in all treated groups, demonstrating the safety of VNPs. Magnification 40 \times . (b) Time-dependent body weight measurements of control and VNPs-treated mice showing no significant difference in all treated groups.86

Figure 4.8 In vivo whole body NIR imaging of biodistribution of free ICG and NAVNs injected intravenously in BALB/c mice. (a) NIR fluorescence image of mice after 24 h post injection of ICG and NAVNs. (b) NIR fluorescence image of mice after 48 h post injection of ICG and NAVNs. (c) NIR fluorescence image of mice dissected after 48 h post injection of NAVNs.87

Figure 5.1 Spectroscopic analysis of free ICG and NAVNs (a) absorption spectra, (b) Jablonski diagram depicting mechanism of possible transitions from and to S_0 state to excited states, (c) fluorescence emission spectra upon 680 nm excitation (d) fluorescence emission spectra upon 420 nm excitation.92

Figure 5.2 Cellular uptake study of NAVNs by TPE bioimaging. (a) TPE (λ_{ex} 790 nm) fluorescence images of HeLa cells treated with NAVNs and free form of ICG, first column signifies bright field images, and the second column signifies TPE fluorescence images ($S_2 \rightarrow S_0$ state transition) captured using multiphoton imaging

system with 40× objective, scale bar, 20 μm. (b) MFI of TPE (λ_{ex} 790 nm) fluorescence images of control, free ICG, and NAVNs treated HeLa cells..... 94

Figure 5.3 (a) Visible light image of three different chicken breast tissue cuboid of ~350 μm thickness used for treatment with 1× PBS, free ICG and NAVNs. (b) TPE fluorescence images of control, free ICG and NAVNs treated chicken breast tissue excited with λ_{ex} 790 nm, λ_{em} 575-630 nm. Magnification 10×, scale bar 100 μm (c) MFI of TPE fluorescent images (λ_{ex} 790 nm) of control, free ICG, and NAVNs treated chicken breast tissue. 95

Figure 5.4 Uptake analysis of NAVNs by chicken breast tissue (a) ex vivo TPE fluorescence images at different depths as indicated. (b) 3D surface plot of Z-stack image. (c) 3D visualization of Z-stack image. (d) Z-projection image with average intensity. (e) fluorescence intensity profile throughout the tissue depth (350 μm).... 97

Figure 6.1 Application of bioinspired and biomimetic ICG encapsulated NPs for in vivo deep tissue NIR and multiphoton bioimaging. 102

Figure 6.2 Vector map of VSV-G displaying insertion of cRGD peptide at N-terminal of VSV-G for the synthesis of VSVGRGD VNPs. 103

LIST OF TABLES

<i>Table 2.1</i> The primers utilized for PCR amplification of VSV-G gene.	29
<i>Table 2.2</i> The sequence of IFN β , IRF3, IFN γ and β -actin gene primers used for qRT-PCR.....	33
<i>Table 3.1</i> ICG encapsulation efficiency (EE) using the different concentrations of ICG for ICGNios fabrication.....	60

ABBREVIATIONS

Near infrared	NIR
Indocyanine green	ICG
Food and Drug Administration	FDA
Nanoparticles	NPs
Drug delivery system	DDS
Vesicular stomatitis virus glycoprotein	VSV-G
Viral nanoparticles	VNPs
NIR active viral nanoconstructs	NAVNs
Two photon excitation fluorescence	TPEF
Vesicular stomatitis virus	VSV
Three-dimensional	3D
Positron emission tomography	PET
Single photon emission tomography	SPECT
Magnetic resonance imaging	MRI
Computed tomography	CT
Ultrasound	US
Fluorodeoxyglucose	FDG
Fluorethymidine	FLT
Ultraviolet	UV
Signal to noise ratio	SNR
Quantum dots	QDs
Hypsochromic aggregates	H-aggregates
Jelly aggregates	J-aggregates
Photoacoustic	PA
Poly(lactic-co-glycolic acid)	PLGA
Magnetic carbon nanoparticles	MCNPs
Red blood cells	RBCs
De-ionized	DI

Ethylenediaminetetraacetic acid	EDTA
Human embryonic kidney	HEK
Human cervical cancer cell	HeLa
National Centre for Cell Science	NCCS
Baby hamster ovary	BHK
Poly-L-lysine PLL Poly-L-arginine	PLA
Dulbecco's modified eagle medium	DMEM
Fetal bovine serum	FBS
Direct current	DC
2-(4-amidinophenyl) indole-6-carboamidinedihydrochloride	DAPI
3-(4, 5-dimethylthiazol-2-yl)-2, 5- diphenyltetrazolium bromide	MTT
Tokyo chemical industry	TCI
Fluorescein isothiocyanate	FITC
Field Emission Scanning Electron Microscopic	FESEM
Transmission electron microscopy	TEM
Encapsulation efficiency	EE
Polydispersity index	PDI
Dynamic light microscopy	DLS
Electron-volt	eV
Dimethyl sulfoxide	DMSO
Capillary tubes	CT
Quantitative real-time polymerase chain reaction	qRT-PCR
Phosphate buffer saline	PBS
Multiplicity of infection	MOI
Sodium dodecyl sulfate	SDS
Polyacryl amide gel	PAGE
Photon correlation spectroscopy	PCS
Plaque forming unit	PFU
European Medicines Agency	EMA
Emission-excitation matrix	EEM
Bright-field	BF

Interferon- β	IFN β
Interferon- γ	IFN γ
Interferon regulatory factor 3	IRF3
Cyclin RGD	cRGD

NOMENCLATURE

Nanometer	nm
Wavelength	λ
Excitation wavelength	λ_{ex}
Emission wave	λ_{em}
Degree celsius	$^{\circ}\text{C}$
Millimolar	mM
Micromole	μM
Microliter	μL
Micrometer	μm
Kilovolt	kV
Nanometer	nm
Centimeter	cm
Ground state	S_0
First excitation state	S_1
Carbon dioxide	CO_2
Minute	min
Watt	W
Energy difference	ΔE
Incident radiation	I_0
Transmitted radiation	I
Absorbance	A
Transmittance	T
Molar extinction coefficient	ϵ
Molar concentration of the sample	c
Path length of the sample cell	l
Percentage	%

Chapter 1

Introduction

Early detection of disease and individualized treatment is key to reducing complications and improving patient's health.[1] In this direction, biomedical imaging plays a significant role in visualizing and real-time monitoring the physiological, structural, functional, and morphological conditions.[2] Also, this provides non-invasive structural information of tissues or organisms at the subcellular/cellular level.[3] Further, the *in vivo* imaging and visualization of various biological processes, including an understanding of receptor dynamics, signal transduction, evaluating the movement of molecules across membranes, etc., are possible using these imaging techniques.[4,5] In addition, biomedical imaging offers the precise measurement of ions and metabolites in biological systems in the context of biomarkers to diagnose and track disease progression and treatment effectiveness.[4]

1.1 Conventional clinical bioimaging modalities

Numerous imaging techniques are routinely used in the medical setting for disease diagnose such as:

1.1.1 Positron emission tomography (PET)/Single-photon emission computed tomography (SPECT)

PET/SPECT are imaging techniques, based on radioactive tracers' signal such as fluorodeoxyglucose (FDG)/fluorothymidine (FLT).[6,7] These techniques rely on the decay of radionuclides, which usually get coupled to a biologically active molecule such as glucose.[8] These analogs can be monitored in the body for minutes to hours after administration and provide data on biological processes. The PET scans are commonly used to identify areas of the body that have excessive sugar metabolism, as

an indicator of tumor growth.[6] Though PET and SPECT are most frequently used to diagnose cancer, these imaging techniques are also used to examine neural activity, myocardial functions, and drug distribution.[9]

1.1.2 Computer tomography (CT)

CT entails emitted and detected X-rays from multiple angles around an object to elucidate internal structures.[10] A CT scan uses ionizing radiation but is considered the gold standard for detecting abnormalities in the body, including tumors, hemorrhages, bone trauma, vascular disorders, and heart conditions.[9] It is often used to diagnose the head, chest, abdomen, pelvis, and upper gastrointestinal tract (GI) diseases.[11] Despite CT's transformative effect in medicine, concerns have been raised regarding the risk posed to the patient by ionizing radiation and unnecessary scans.

1.1.3 Magnetic resonance imaging (MRI)

MRI exceptionally provides detailed information of the soft tissue and can produce images in any plane. It is a non-invasive technique and does not utilize ionizing radiation to generate images; instead, it relies on a strong magnetic field and radio waves.[12] In addition to CT, MRI is also a vital imaging method both in clinical and preclinical studies. This technique enabled imaging of the central nervous system (CNS), musculature, joints, and soft tissue structures.[9] The resulting MRI images can display pathologic attributes of disease processes rather than just its presence or absence. It provides sufficient information, to begin with, the treatment without the necessity for a biopsy or other diagnosis mode. However, MRI is a time-consuming and expensive method compared to other imaging modalities. The image acquisition procedure is also vulnerable to image artifacts caused due to metallic implantations in patients.

1.1.4 Ultrasound (US)

Currently, the US is the most commonly used imaging technique due to its affordability, accessibility, transportability, radiological safety, and real-time functionality. In this technique, the acoustic waves generate vibrations with a frequency above the audible range of human and translate tissue effects onto these waves.[13] This effect forms the basis for diagnostic sonography. The technique is clinically used in prenatal medicine and to diagnose diseases in most major organs, with variations such as Doppler echocardiography and elastography to examine structural and functional characteristics.[14] The US technology has several shortcomings, including considerable noise and a limited ability to penetrate deep into tissues, where resolution decreases as depth increases.

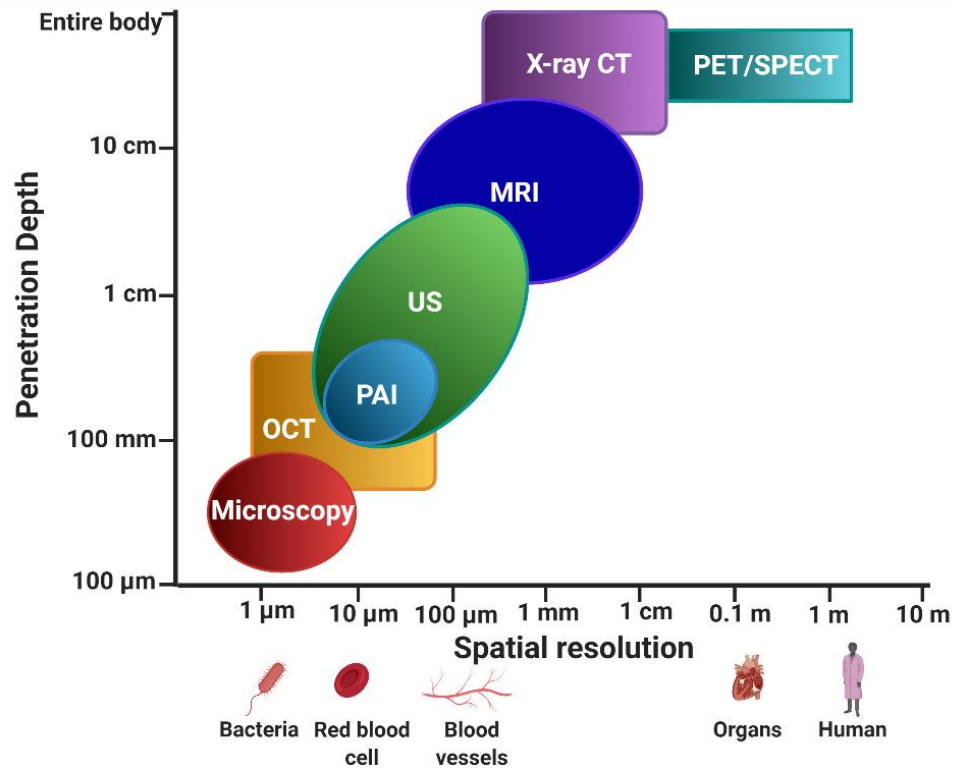


Figure 1.1 A comparison of the depth of penetration and resolution of current biomedical imaging techniques. PET, positron emission tomography; SPECT, Single-

photon emission computed tomography; CT, computed tomography; MRI, magnetic resonance imaging; US, ultrasound; PAI, photoacoustic imaging, OCT, optical coherence tomography.[15]

Despite their widespread use in the clinical setting, conventional imaging techniques have a limited spatial resolution, as illustrated in **Fig. 1.1**. [16] Under best conditions, the smallest details can be observed in the range of half a millimeter. In addition, imaging with optical methods can produce spatial resolutions of micrometers or better, but they do not penetrate deeply, so their use is inappropriate for visualizing deeply buried biological samples. [17] At the same time, MRI and X-ray CT use a high dosage of exogenous contrast agents (gadolinium- and iodine/barium-based contrast agents) that can seriously impact a patient's health. [18–20] Due to long scanning time, low sensitivity, radiation hazard, and low spatial resolution, these methods require higher optimization for obtaining more accurate data. [21]

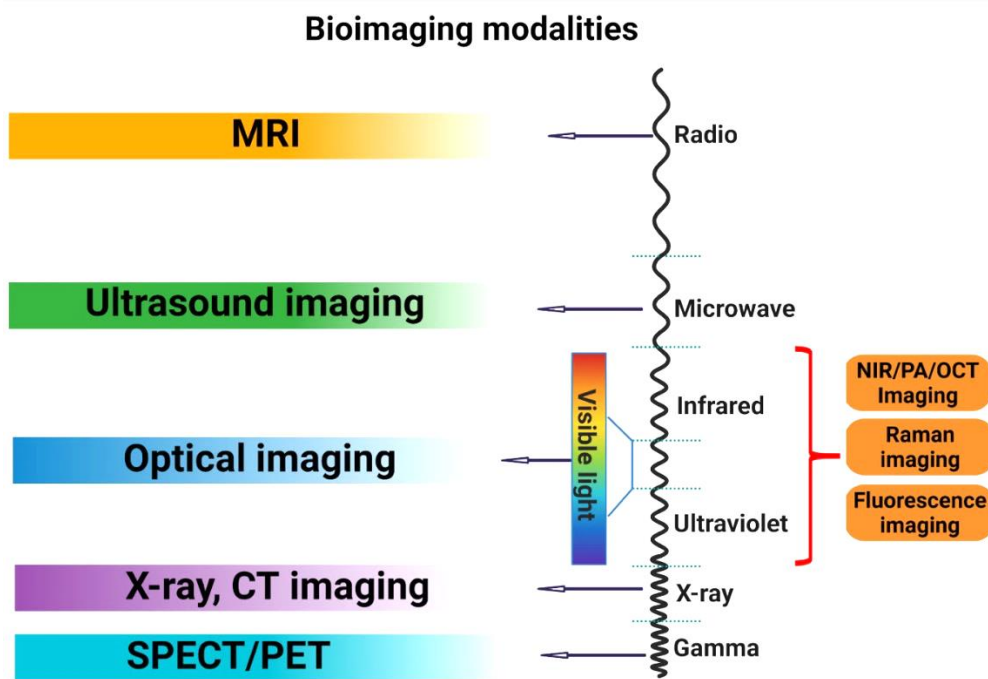


Figure 1.2 *Imaging modalities using distinct wavelength of electromagnetic spectrum. MRI, PET, SPECT, CT, NIR near-infrared, PA: photoacoustic, OCT.*[22]

1.1.5 Emerging preclinical modalities

Over the last few years, optical imaging has become the spotlight, primarily in preclinical research studies. It provides excellent visualization in real-time and high sensitivity/spatial resolution for early-stage disease diagnosis.[23,24] By utilizing the unique properties of light and photons, optical imaging can obtain detailed images of small molecules, cells, tissues, and organs.[25] As depicted in **Fig. 1.2**, optical imaging has the advantage of using non-ionizing radiation, which minimizes radiation exposure to patients.[26] Since optical imaging is safer than the techniques requiring ionizing radiation, such as X-rays, it is suited for repetitive testing to track the progress of disease or treatment. Additionally, the optical imaging technique is advantageous for assessing the unique properties of soft tissue.[27] Since light scatters and absorbs differently in soft tissues, optical imaging can detect changes in metabolic activity as early indicators of tissue and organ dysfunction.[27,28] Generally, most optical imaging modalities work in the short-wavelength region of the electromagnetic spectrum (ultraviolet (UV) and visible regions).[29] Though, the majority of the biological components (body fluids, skin and muscle) easily absorb and scatter light in this spectrum leading to autofluorescence, reduced signal-to-noise ratio (SNR) and low tissue penetration depth.[30–32] In addition, the incidence of light with higher energy can lead to photodamage of biological tissues.[33] Therefore, a comprehensive understanding of the optical properties of biological components is needed as the interaction between photons and tissue determines how deeply one can image and probe molecular processes faithfully with high SNR.

1.2 Importance of near-infrared (NIR) imaging

To address the aforementioned challenges, bioimaging in the near-infrared (NIR) region or "tissue optical window" (650–900 nm) has gained significant interest due to reduced photon absorption, scattering, and tissue autofluorescence.[34] Consequently, reduced background interference from the biological components (HbO₂, Hb and H₂O) in the NIR region improves penetration depth and SNR of the optical images compared to UV and the visible region as depicted in **Fig. 1.3**.[35,36]

As a result, a non-invasive and radiation-free method of obtaining high-resolution deep tissue images can be employed by NIR imaging. Further, the sensitivity and detection limits of NIR imaging can be enhanced using exogenous NIR active contrast agents.[37,38] There have been numerous reports describing NIR emitting organic and inorganic fluorophores so far.[39] Subsequently, several NIR emitting NPs, semiconductor quantum dots (QDs) and organic dyes have also been explored for *in vivo* NIR imaging.[40] However, for bioimaging applications, the contrast agent must be biocompatible and should not elicit an adverse immune response in the body. In this regard, out of various NIR active fluorophores, indocyanine green (ICG) is one of the contrast agents approved for clinical use.[41]

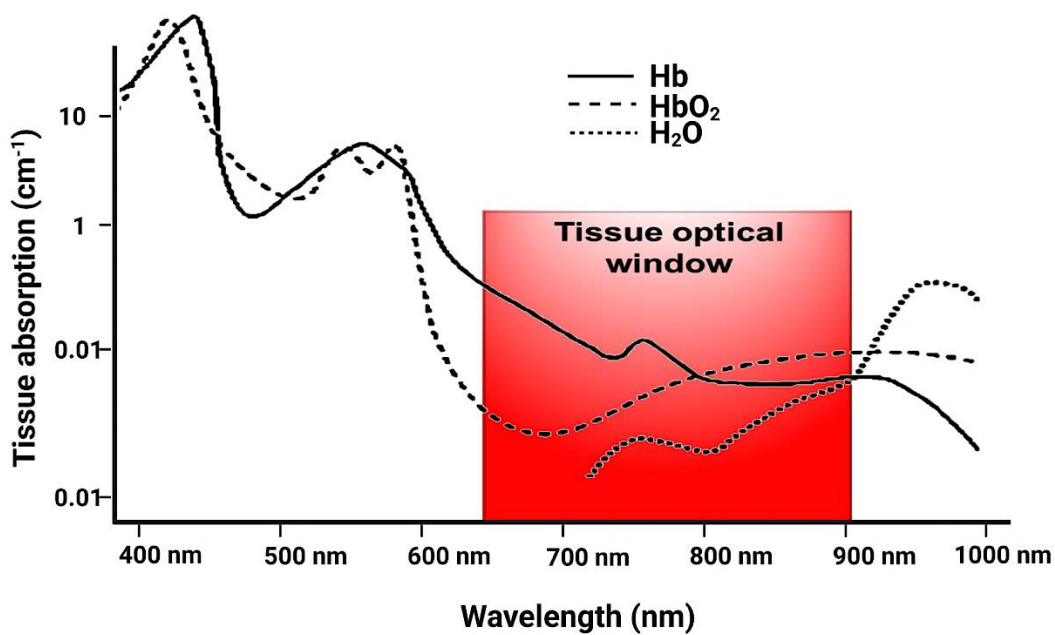


Figure 1.3 The absorption spectrum of light with wavelengths of around 650-900 nm depicts the tissue optical window for deeper penetration due to minimal absorption in this range by the biological components HbO₂, Hb, and H₂O.

1.3 Importance of ICG for NIR imaging

ICG is used in clinical applications since 1959. The applications started with studying cardiovascular measurements, ophthalmology imaging, and testing liver function in humans.[42] ICG has desirable features of minimal toxicity and enhanced absorbance over a wavelength range of 650 nm to 900 nm, which is a “tissue optical window”.[43] Therefore, ICG enabled imaging-guided early-stage cancer diagnosis and follow up surgical practices.[44–46] Over the years, clinical applications of ICG in the patients have proven to have no significant side effects (<0.15%), and are hence considered one of the safest dyes for bioimaging.[47,48]

1.3.1 Structure of ICG

ICG is a tricarboyanine dye with a chemical formula of $C_{43}H_{47}N_2NaO_6S_2$ and a molecular weight of ~775 Daltons.[49] ICG exhibits absorption and emission wavelengths in the NIR region.[49,50] The molecular structure of ICG constitutes two lipophilic polycyclic moieties, linked through a polyene bridge as presented in **Fig. 1.4**.[51] In addition, the sulfonate group on nitrogen of each polycyclic moiety provides ICG, a net negative charge and water solubility. Owing to the overall molecular structure, ICG exhibits amphiphilic properties, which improves its solubility in biological fluids and its bioavailability, which is crucial for clinical applications.[52,53]

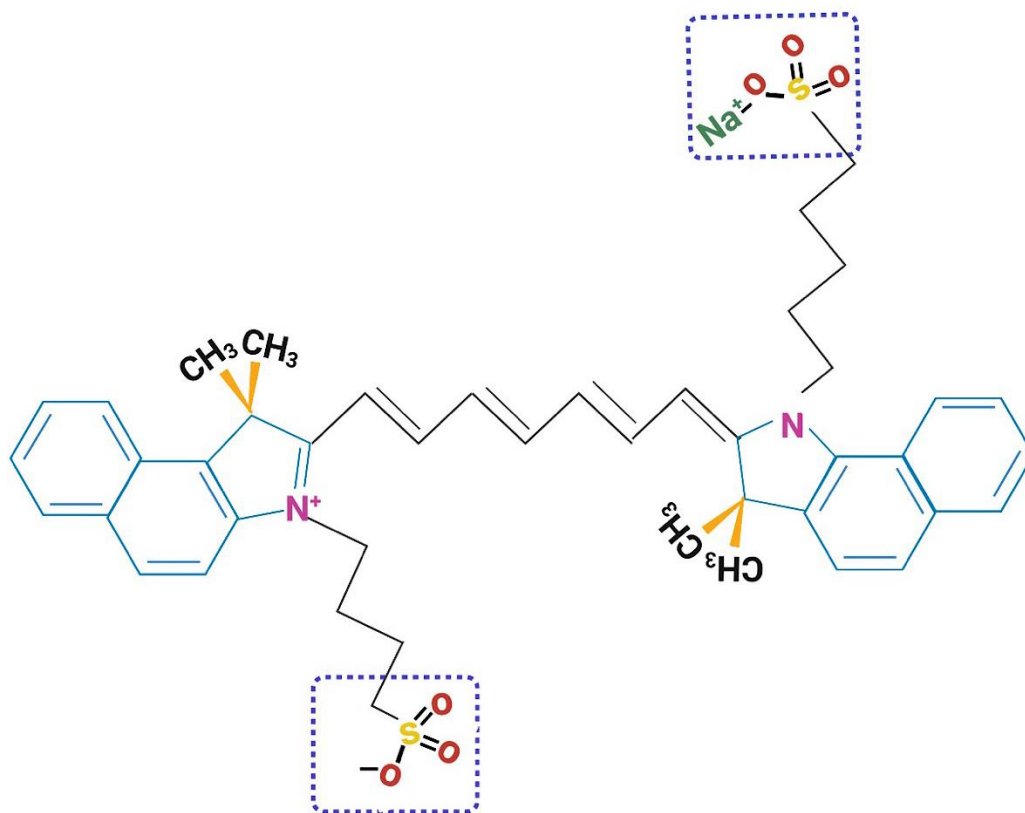


Figure 1.4 Chemical structure of ICG dye. The ICG comprises two hydrophobic polycyclic rings (benzindotricarbocyanin) linked by carbon chains, each containing a sulfate group (blue dotted box) linked by a carbon chain, making it hydrophilic.

1.3.2 Optical properties of ICG

The optical properties of ICG mainly depend on the concentration and the properties of the solution in which it is dissolved.[54] The ICG exhibits absorption and fluorescence emission in the NIR region. ICG absorbs mainly in the wavelength range of 600 nm and 900 nm and emits fluorescence between 750 nm and 950 nm. As seen in **Fig. 1.5**, the free ICG in an aqueous solution displays maximum absorption and emission at the wavelength of ~780 nm and ~810 nm. The spectral peaks of free ICG at 780 and 710 nm correspond to its monomeric and dimeric (H-like aggregates) forms.[43] In addition to the widely used absorption and emission of ICG in the NIR wavelength, it also shows higher energy absorption properties between the 350 nm to 500 nm wavelength range.[55] Consequently, the higher energy optical characteristic

of ICG is crucial for deep-tissue multiphoton bioimaging and therefore needs more exploration.[55]

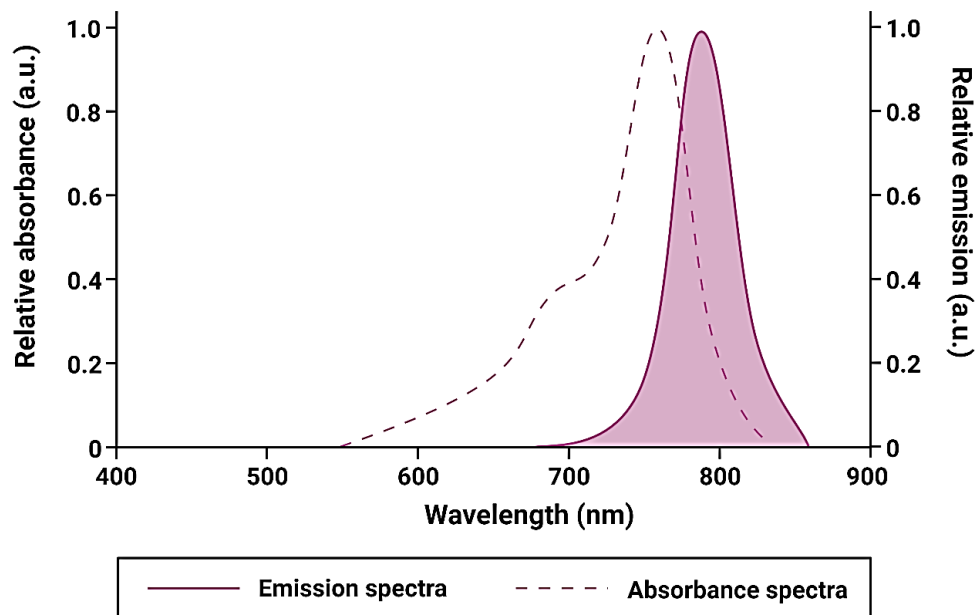


Figure 1.5 Absorption ($\lambda_{max(ab)} = 780 \text{ nm}$) and emission spectra ($\lambda_{max(em)} = 810 \text{ nm}$) of ICG dye in water.

1.3.3 Aggregation of ICG in aqueous solution

ICG have a tendency to form highly ordered aggregates like other carbocyanine dyes.[56] The aggregation of ICG depends on the concentration and the nature of the solvent.[57] The aqueous solution of ICG tends to form oligomers at high concentrations, primarily due to hydrophobic interactions and van der Waals forces.[58–60] Further, in an aqueous solution, ICG remains in equilibrium between monomers, dimers, and aggregates. The monomeric form of ICG predominates at lower concentrations (5 μM), while the oligomeric form is prominent at higher concentrations (100 μM). The organization of different states of ICG in an aqueous solution alter its optical properties. Based on the organization pattern of ICG monomers within the aggregate, hypsochromic shifts (caused by H-aggregates) or bathochromic shifts (caused by J-aggregates) are observed in the absorption spectra with

respect to its monomeric absorption band, as depicted in **Fig. 1.6**.^[61] ICG in aqueous solution displays both types of aggregate spectra based on the condition of its preparation. In H-aggregates, ICG and its transition dipole get arranged in a stacked (like sandwich) manner, whereas in J-aggregates they adopt linear “head-to-tail” arrangements.^[62,63] H-aggregate generally quenches the fluorescence emission of ICG, which adversely affects its applications relying on the fluorescence property.^[64] Therefore, to exploit ICG for biomedical applications, it is essential to inhibit the H-aggregation of dye. However, the J-aggregates are spectroscopically active and stable, allowing biomedical imaging with negligible autofluorescence, reduced scattering and higher penetration depth in the biological tissues.^[65–67]

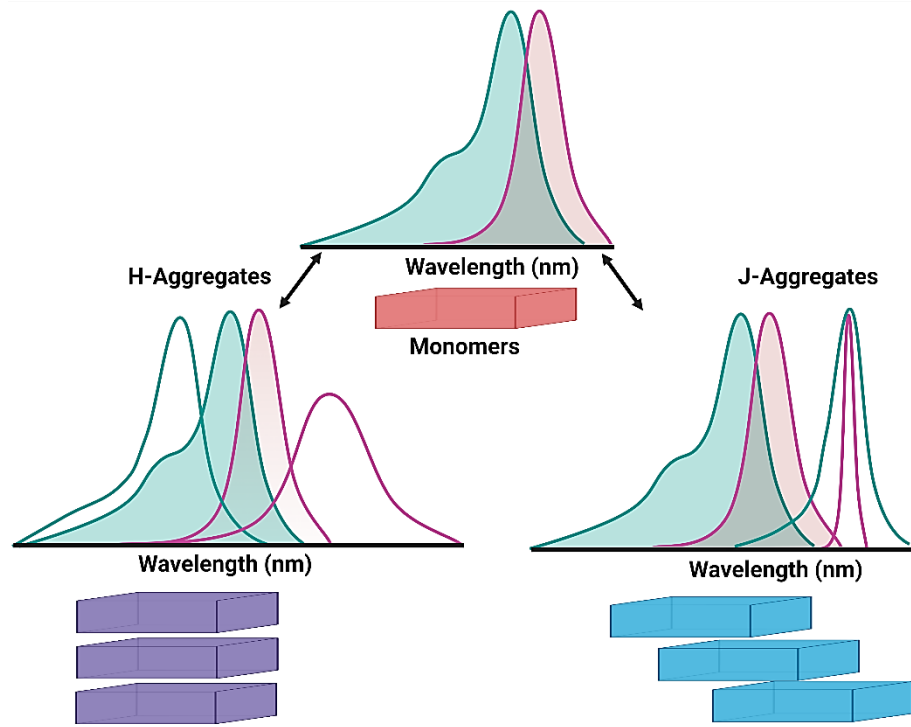


Figure 1.6 Illustration of the absorption (blue) and fluorescence (pink) spectra of H-aggregates arranged in “head-to-head” orientation and J-aggregates associated in “head-to-tail” orientation formed by ICG monomers.

1.4 Biomedical imaging applications of ICG

Kodak Research Laboratories brought ICG for NIR photography in 1955 and by the following year, it entered clinical use.[54,68]. Following FDA approval in 1959, ICG was initially administered to diagnose hepatic functions and then in cardiology.[69] Further, in 1964, renal blood flow and subretinal functions in the eye's choroid were examined. Afterwards, the ICG is being used as a standard, especially in ophthalmology for fluorescent angiography.[70] By virtue of its favorable NIR optical properties, ICG has also been widely used in numerous medical fields for diagnostic and therapeutic applications.

1.4.1 NIR photoacoustic (PA) imaging

PA imaging is a non-invasive optical technique that can visualize cellular and molecular details of different organs at clinically relevant depths. PA imaging does not rely on ionizing radiation like other popular imaging techniques such as X-ray, CT, and PET.[71,72] As illustrated in **Fig. 1.7**, PA imaging system integrates both optical and acoustic imaging by utilizing NIR laser pulses to excite thermoacoustic waves from the biological tissue stained with a suitable molecule or chromophore.[73,74] For the spatial resolution of the contrast agents, the photoacoustic waves are detected by a sensitive ultrasound transducer. Consequently, PA imaging has gained increasing attention in recent years as it improves penetration depth and spatial resolution over traditional optical and acoustic imaging methods.[75–77] In addition, like US imaging, PA imaging also facilitates 3D reconstruction and precise diagnosis and prognosis. Further, to obtain a strong PA signal, high thermal conversion efficiency and robust NIR extinction coefficient are required. During the past decade, there has been much interest in generating PA signals by using exogenous chromophore. The excellent NIR absorbance of ICG and FDA approval makes it one of the extensively studied contrast agents for PA imaging.[77,78] PA imaging using ICG improved contrast and SNR of the images, which is efficient in detecting early-stage cancer.[79,80] Subsequently, ICG in the conjugation with other metals and carbon nanotubes was employed for PA imaging, which displayed significant enhancement in the contrast of images in the *in vivo* model.[77,81,82] Additionally, the photoacoustic therapy of cancer cells was also performed with various nanoparticles (NPs) loaded with ICG.[83] A study of *in vivo* PA imaging of breast carcinoma was carried out using polylactic/co-glycolic acid (PLGA) lipid NPs conjugated with folate receptors.[84] Also, non-invasive PA imaging of tissue targeting ICG loaded nanoliposomes has been studied.[85] Therefore, both free and nanoencapsulated forms of ICG have been exploited in recent years for PA imaging and therapy.[86,87]

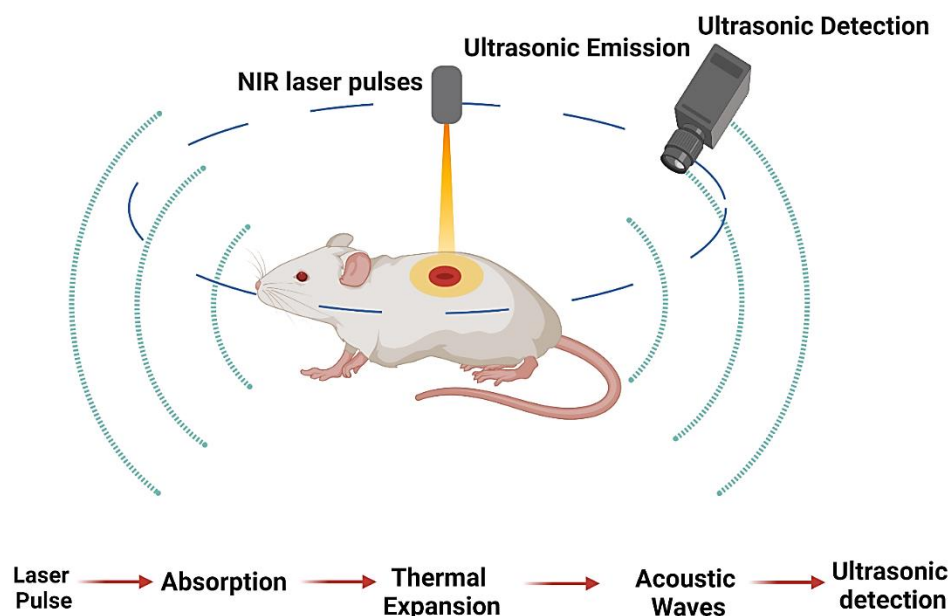


Figure 1.7 Schematic of NIR photoacoustic (PA) imaging. A pulse of laser is used to irradiate the chromophore-tagged biological tissue, causing it to produce ultrasonic waves originating from photo absorbers based on thermoelastic expansion. An ultrasound transducer detects the signal that is used to form images of tissue structures.

1.4.2 NIR fluorescence (NIRF) imaging

Among various imaging modalities, fluorescence imaging particularly NIRF imaging has been shown to be an effective non-invasive technique for diagnosing cancer in its early stages. NIRF imaging is mostly used to detect tumor margins and to localize metastatic lymph nodes for imaging guided surgery.[88,89] In this context, the ICG is widely used as a NIR-active contrast agent for cancer and metastatic lymph node imaging. NIRF imaging studies on humans typically use ICG for contrast imaging in the blood and vasculature for assessing vascular repair intraoperatively.[90] Usually, nanoencapsulated ICG is used for NIRF imaging applications. In recent studies, ICG-loaded magnetic carbon nanoparticles (MCNPs)

have been shown to be useful for *in vivo* NIRF imaging of breast cancer.[91] Consequently, NIRF imaging enables monitoring of the accumulation of ICG-loaded MCNPs in the mouse organs and tumors in real-time. Furthermore, the *in vivo* NIRF imaging using ICG encapsulated NPs demonstrated their selective and effective targeting within the breast and pancreatic cancer models.[92] Utilization of combined NIRF and radionuclide imaging using ICG and technetium-99m embedded in functionalized silica nanoparticles successfully identified deeply buried sentinel nodes and breast cancer cells with overexpressing HER 2 receptors.[93] NIRF imaging of liver cancer patients using mesoporous silica NPs (MSNs) with highly loaded ICG allowed accurate delineation of tumor borders and detection of residual tumor tissue, as a high payload of ICG generates a high contrast between tumor and normal tissue.[94] Likewise, various other nanoformulations of ICG have been used for NIRF imaging in biomedical imaging for disease diagnosis.

1.4.3 Multimodal imaging

The conventional imaging modalities such as MRI, CT, US, SPECT, PA, and optical imaging are among the most used medical imaging paradigms for diagnosing tumors and monitoring treatment outcomes.[95–97] However, each imaging modality has its own inherent benefits and drawbacks. The optical imaging technique can be used to monitor nanoparticles throughout the body in real-time with a high level of sensitivity.[98] However, due to low spatial resolution owing to optical scattering, the clinical application of optical imaging is limited. As MRI provides images of deeply seated tumors, it is one of the most widely used non-invasive imaging procedures in clinical settings.[99] Though, MRI's clinical utility is limited due to low sensitivity, requirement of extensive instrumentation, and time-consuming data collection process.[100] Therefore, the contrast agents that permit multimodal detection ability are beneficial for imaging different tissues (such as soft tissues via MRI, blood vessels via PA imaging, and specific cells by optical imaging), translating preclinical to clinical imaging, and integrating preoperative to intraoperative bioimaging.[95,101] Multimodal imaging involves the use of two or more imaging techniques to co-register complementary images in a single examination.[102] Combining NIR imaging with

MRI provides 3D information about the anatomical structure and molecular details of the tissue with high spatial resolution and high penetration depth.[103] In addition, the use of exogenous contrast agents in combination with molecular imaging provides improved SNR and high-resolution images for early-stage disease diagnosis.[104,105] It has recently been demonstrated that exogenous ICG is an excellent contrast agent for multimodal bioimaging for disease diagnosis, as displayed in **Fig. 1.8**. [106,107] MRI/NIR optical synchronized imaging using ICG loaded magnetic resonance nanomaterials have also been used.[108–110]. Additionally, dual-modality fluorescence imaging/MRI using superparamagnetic iron oxide (SPIO) NPs containing polyethylene glycol (PEG), a tumor-targeting peptide, and ICG have been reported recently.[111] There has been considerable interest in MRI/NIR diffusion optical tomography imaging after administration of an ICG to detect cancer in a precise manner.[112]

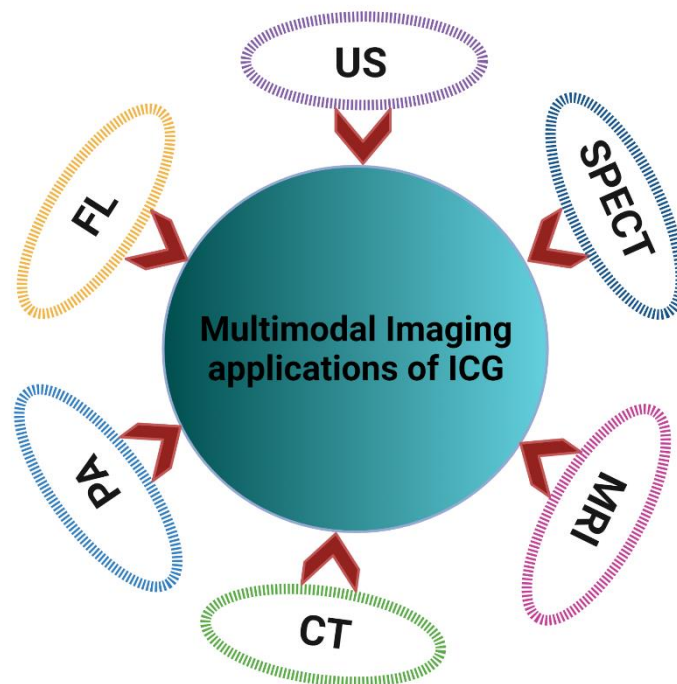


Figure 1.8 Overview of ICG as a potential agent for multimodal imaging applications. MRI: magnetic resonance imaging, CT: computed tomography, PA: photoacoustic,

SPECT: Single-photon emission computed tomography, FL: fluorescence US: ultrasound.

1.4.4 Multiphoton bioimaging

As a non-invasive method, single-photon excitation (SPE) fluorescence microscopy has been extensively used for bioimaging.[113] However, SPE microscopy techniques exhibit low penetration depth, thus limiting the scope of their applications. Moreover, two-photon excitation (TPE) fluorescence microscopy circumvents the limitations of conventional SPE microscopy for image acquisition in deep tissues.[114] The TPE is based on the nonlinear absorption property of photons by fluorophores and utilizes low-energy photons for imaging, which reduces the photobleaching and photodamage of biological samples compared to the SPE fluorescence technique.[115,116] Using the TPE method, the first singlet (S_1) state of the exogenous contrast agent can be excited in the visible range, which enables deeper imaging than a conventional fluorescence microscope.[117] Furthermore, TPE fluorescence imaging reduces the background associated with SPE and minimizes scattering caused by short wavelengths.[118] Consequently, conventional TPE fluorescence imaging excites fluorophores at NIR wavelengths and emits them at visible wavelengths.[117,119] In order to improve tissue penetration depth, excitation and emission wavelengths for bioimaging must fall within the “tissue optical window”. Though, it is not possible to achieve this goal with two-photon S_1 excitation. Two-photon microscopy based on the fluorescence emission from the second singlet state (S_2) of ICG could be utilized to visualize deep tissues.[55] Importantly, the TPE of ICG enables the absorption and emission wavelengths to fall within the “tissue optical window”. [120] As reported previously, TPE fluorescence images of beads stained with ICG showed strong emission intensities, indicating that ICG can be exploited as a two-photon contrast agent for improving fluorescence images.[120] Moreover, our group has shown that aqueous ICG can efficiently fluoresce from the S_2 state following TPE, with maximum excitation at wavelengths of 790 nm.[55] As shown in the **Fig. 1.9**, for the first time, the non-linear property of ICG for cellular imaging was demonstrated. Following its optical property, biocompatibility, and FDA approval,

ICG can be used in clinical and preclinical settings to investigate *in vivo* deep tissue TPE fluorescence bioimaging. Notably, more exploration is needed to use ICG in TPE fluorescence imaging to achieve deep tissue optical images with improved SNR.

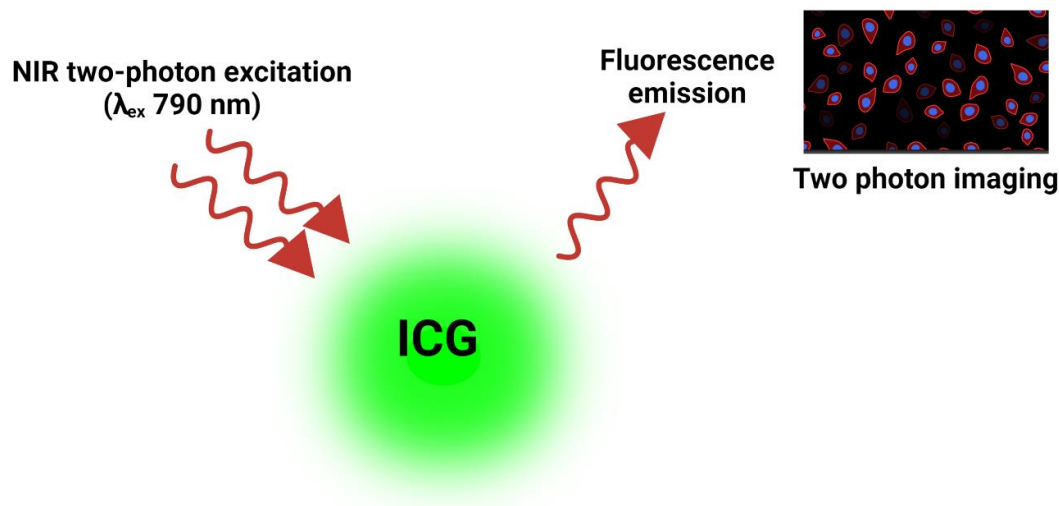


Figure 1.9 Mechanism of NIR two-photon excited (λ_{ex} 790 nm and λ_{em} 575-630 nm) ICG dye for multiphoton bioimaging.

1.5 Shortcomings of ICG

Although ICG is frequently used for clinical diagnosis, its utilization is restricted by concentration-dependent aggregation, aqueous instability, low emission intensity, nonspecific protein binding, chemical degradation, and photodegradation.[59,121] Due to these limitations, ICG has short circulation times (~2-4 minutes) in the body. To increase the efficacy of ICG and extend its plasma half-life, it should either be loaded or encapsulated within the NPs.[122]

1.6 Nanoencapsulation of ICG

The use of NPs for ICG delivery is a promising way to overcome its inherent inefficiency as well as to improve its functionality for biomedical applications.[123] These NPs are homing systems that shield and protect highly unstable molecules from

physiological changes, thereby preserving their pharmacological activity. Following this, various nanofabrication strategies have been developed for ICG after unremitting efforts.[83,122,124] ICG delivery has extensively been exploited by lipid-based, polymer-based, magnetic, and mesoporous silica and metallic NPs, as can be seen in **Fig. 1.10**. Many of the above-mentioned NPs have been functionalized with a targeting moiety to facilitate targeted delivery and imaging. Further, various preclinical studies have demonstrated the successful application of ICG NPs' for tumor imaging and therapy.[125,126]

Although several ICG encapsulation systems have been synthesized successfully, their applications in clinical settings remain limited by issues such as poor biocompatibility, slow biodegradation, and accumulation within tissues resulting in short- or long-term tissue damage.[127–129] Also, chemically synthesized materials can be immunotoxic, so smart approaches to their decoration are essential. Besides improving the ability to image and target, it is imperative to provide appropriate therapeutic regimens and address safety and efficacy concerns for clinical applications. Thus, instead of chemically synthesized nanocarriers, nowadays the significant interests have been shown to encapsulate the cargo within biomacromolecules such as amino acids, proteins, carbohydrates, lipids, and nucleic acids.[130–133] Therefore, the development of novel biocompatible and biodegradable nanocarriers is crucial for the success of ICG encapsulated NPs in clinical settings.

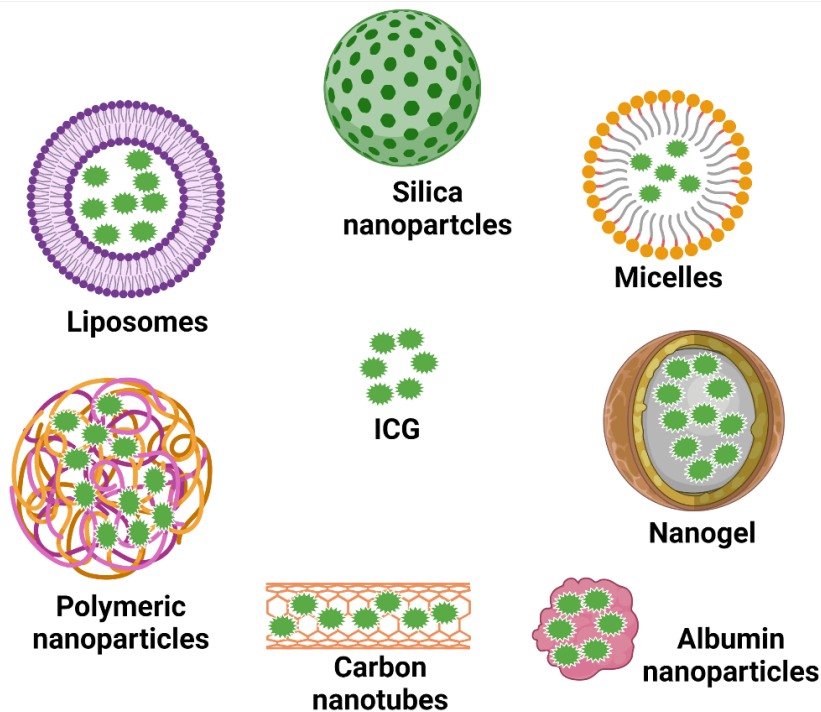


Figure 1.10 Different surface modifications and functionalization strategies used to load or conjugate ICG to a variety of nanostructures, such as silicon, micelles, liposomes, nanogel, carbon nanotubes, albumin-based, polymer-based, lipid-based nanoparticles.

1.7 Bioinspired nanoparticles

In this perspective, the bioinspired and biomimetic NPs are an essential alternative to overcome toxicity and accumulation concerns. These NPs are made using synthetic and natural materials whose structure, properties, and functions mimic biological systems. **Fig. 1.11** displays numerous bioinspired and biomimetic NPs exploited for drug delivery. These NPs bring together the functionality of biological and synthetic materials to accomplish effective drug delivery and interfacing in sophisticated biological processes. Various bioinspired nanoparticles, including lipid-based, silica-based, hydrogel-based, polymer network hydrogels, and calcium phosphate nanocarriers, have been recently investigated as a platform for drug delivery applications.[134] It is noteworthy that naturally occurring bioactive materials are desirable compared to synthetic NPs due to their excellent biocompatibility, cell

targeting ability, low immunogenicity, and degradability in biological tissues.[135] As such, the fabrication and utilization of bioinspired and biomimetic materials derived from bacteria, viruses, fungi, and cells are advantageous for their use in clinical settings as drug delivery systems (DDS).[134] These platforms have a great potential to be used as DDS owing to their less toxicity, high biocompatibility, and significant interaction with biological processes. Thus, bioinspired, and biomimetic NPs have a bright future ahead with tremendous potential to resolve the obstacles faced in drug delivery.

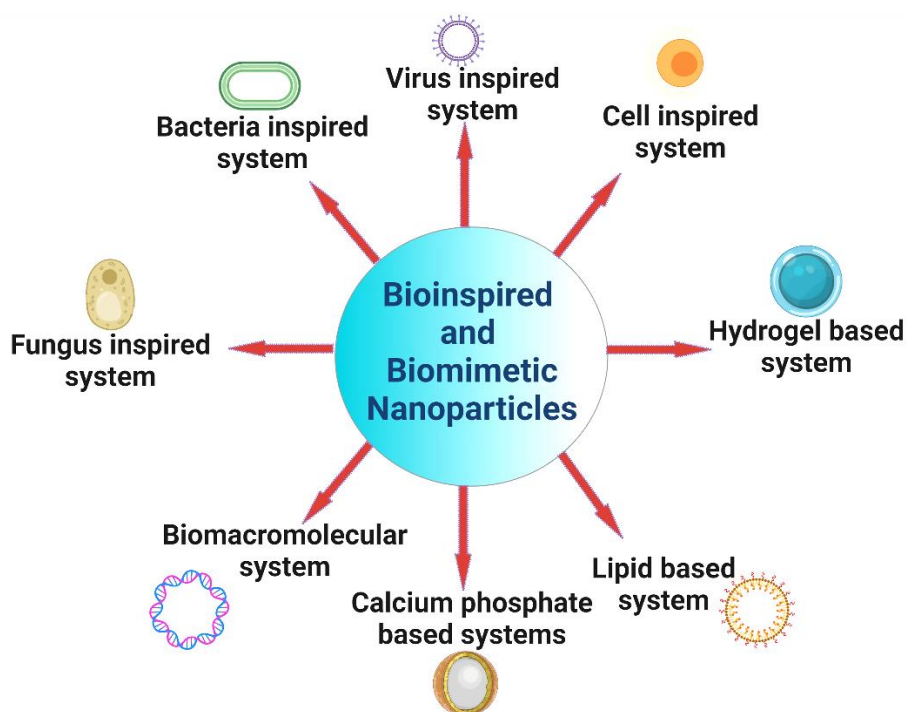


Figure 1.11 A schematic representation depicting different bioinspired and biomimetic drug delivery systems fabricated by synthetic (lipids, calcium phosphate, hydrogel) and biologically derived (cell, virus, bacteria, fungus, biomacromolecules) materials.

1.8 Aim of the thesis

In clinical settings, ICG is used as a NIR contrast agent. Despite this, ICG has not been used fully in clinics for bioimaging due to its low quantum yield,

concentration-dependent aggregation, aqueous instability and photodegradation. The present thesis is focused on fabricating bioinspired and biomimetic nanosystems for ICG encapsulation. In this quest, niosomes nanovesicles, and vesicular stomatitis virus glycoprotein (VSV-G) based VNPs were explored to encapsulate ICG and evaluated for improved NIR and multiphoton deep tissue imaging.

The thesis has the following three main objectives:

1. To employ a simple self-assembling method for fabricating novel bioinspired ICG encapsulated niosomes (ICGNios) synthesized from non-ionic surfactants and cholesterol. And evaluate ICGNios's *ex vivo* deep tissue NIR imaging potential.
2. Similarly, we aimed at utilizing structural protein (glycoprotein) of vesicular stomatitis virus (VSV) to fabricate NIR-active viral nano constructs (NAVNs) to encapsulate ICG and tested its NIR optical imaging potential.
3. The other main objective is to exploit two-photon excitation (TPE) property of ICG encapsulating NAVNs to obtain deep-tissue optical images by employing multiphoton bioimaging technique.

1.9 Thesis organization

The current thesis is organized into six chapters where the first chapter presents the research problems. The second chapter describes the materials and methods used to conduct this research work. Chapter 3 describes the fabrication of novel biocompatible NIR active ICGNios with enhanced optical stability, fluorescence quantum yield and emission compared to free ICG. Further, this chapter illustrates the potential of ICGNios NPs for efficient delivery of ICG in cells and deep tissue *ex vivo* NIR imaging in chicken breast tissue. Chapter 4 focuses on fabricating bioinspired and biomimetic VNPs encapsulating ICG for *in vitro* and *in vivo* NIR bioimaging. It also delves into the analysis of the biochemical properties, photostability, drug release behavior, cellular uptake, and biosafety of VSV-G based VNPs. Chapter 5 presents the use of fabricated VSV-G-based NAVNs for two-photon deep-tissue optical imaging. Here, the efficacy of NAVNs for two-photon fluorescence imaging is

demonstrated in *in vitro* models. The high penetrative capability of two-photon imaging with NAVNs is investigated in chicken breast tissue (350 μm tissue depth). A summary of the significant finding is presented in Chapter 6, followed by possible future applications in clinical settings.

Chapter 2

Materials, Methods, and Instrumentations

2.1 Introduction

This chapter describes the materials, methods, and principles of the instruments used to perform the experiments successfully. Additionally, the details about the fabrication of NPs and their experimental arrangements are described. The description of each of the characterization techniques used in this thesis is also presented in this chapter.

2.2 Materials

Span 80 (sorbitan monooleate) was purchased from Loba chemie, Mumbai, India. Tween 80 (polyoxyethylene sorbitan monooleate) was procured from Himedia, Mumbai, India. Cholesterol was bought from LobaChemie (Mumbai, India), and chloroform was obtained from MP Biomedical LLC (Mumbai, India). ICG was acquired from Sigma-Aldrich, India. The stock solution of ICG was made by dissolving it in de-ionized (DI) water (18.2 MΩ Millipore, Sartorius system) and stored at -20 °C till further use. The cell nuclear staining dye, DAPI (2-(4-amidinophenyl) indole-6-carboxamide-dihydrochloride) was obtained from the Himedia (India). The human embryonic kidney (HEK293T) cells, human cervical cancer (HeLa) cells, and baby hamster kidney (BHK-21) cells were procured from the National Centre for Cell Science (NCCS) Pune, India. The lipofectamine-2000 reagent was procured from Gibco. Dulbecco's modified Eagle's medium (DMEM), penicillin-streptomycin, fetal bovine serum (FBS) and 0.25 % trypsin-1 mM ethylenediaminetetraacetic acid (EDTA) were purchased from were bought from HiMedia (Mumbai, India). The anti-VSV-G polyclonal antibody was procured from Sigma. Western blot is detected by chemiluminescence reagent (SERVA, India.) and GELA Chemidoc LAS4000 system.

2.3 Methods

2.3.1 Niosome preparation

Non-ionic surfactant mixtures consisting of Tween 80, Span 80, and Cholesterol were used to prepare niosomes by a thin film hydration method at specified molar ratios of 0.4:0.4:0.2. In brief, the surfactants and cholesterol were dissolved in 500 μ l of chloroform in a 10 ml round-bottom flask. A rotary evaporator apparatus was used to evaporate the solvent at 37 °C under a high vacuum atmosphere. As a result, a thin-film formation was achieved, and the samples were kept in a desiccator to remove residual chloroform. The film was hydrated with DI water to make a final niosomes concentration of 5 mM. Similarly, for fabricating ICGNios, 50 μ M, 100 μ M and 200 μ M stock solution of ICG was used for thin-film hydration, which was done while stirring the mixture, followed by vigorous vortexing. The ICGNios was then pelleted down using centrifugation to get rid of un-encapsulated ICG. Pellet containing ICGNios was resuspended in DI water for further use.

2.3.2 Encapsulation efficiency estimation of ICG within Niosomes

To estimate ICG encapsulation efficiency (EE) of ICG within niosomes, the ICGNios were centrifuged, and the pellet of ICGNios was resuspended in dimethyl sulfoxide (DMSO) to disintegrate NPs to release ICG from niosomes. The absorption of released ICG was taken by UV/Vis spectrophotometry. And the concentration was calculated using the calibration curve of free ICG dissolved in DMSO. The EE was calculated by equation (i):

$$EE(\%) = \frac{\text{The concentration of ICG in ICGNios disintegrated in DMSO}}{\text{The total concentration of ICG used for ICGNios synthesis}} \times 100 \dots \dots (i)$$

2.3.3 Morphological characterization

The morphology of niosomes and ICGNios were assessed by field emission scanning electron microscope (FESEM). For SEM imaging, samples were drop cast on a glass slide and dried overnight in a desiccator. Following drying, the niosomes were drop casted on carbon tape, and sputter-coated using gold by direct current (DC) sputter coater. The operating voltage of the electron gun was kept between 2–5 kV. The accurate size of ICGNios was then determined by a transmission electron microscopy (TEM). The samples were dropcast on a 400-mesh carbon-coated copper grid for TEM imaging and stained using uranyl acetate (1%). Additionally, dynamic light scattering (DLS) was used to evaluate the hydrodynamic diameters (D_h) and polydispersity index (PDI) of niosomes, and ICGNios. The DLS spectroscope equipped with a diode laser of 660 nm at 25 °C was used for analysis. For the size measurements, the geometry of the scattering light collection was done at 175°.

2.3.4 Spectroscopic investigation

The biochemical characterization of ICG encapsulation within niosomes was studied by absorption and emission spectra analysis. The absorption spectra measurements of all samples were performed using a UV/vis/NIR spectrophotometer, and fluorescence emission of all the samples were recorded using a spectrofluorometer. The samples were excited with a 400 W Xenon lamp using 680 nm as an excitation wavelength (λ_{ex}). The fluorescence emission was evaluated with the excitation-emission slit width of 5 nm and 2 nm, respectively. The fluorescence spectrum was obtained and analyzed using Origin 2021b (OriginLab Corporation, Northampton, MA, United states) software.

The excitation-emission matrix (EEM) spectral map of free ICG, niosomes and ICGNios was generated by scanning fluorescence emission as a function of excitation wavelengths. The study used excitation wavelengths between 660 and 780 nm at 5 nm increments and fluorescence emission wavelengths between 785 and 950 nm.

2.3.5 Fluorescence quantum yield calculation (Φ_s)

For calculation of Φ_s , the test (ICGNios) and reference (free ICG) samples having similar absorbance at the excitation wavelength was used as they are supposed to absorb equal number of photons. The absorption of samples was recorded using a UV/vis/NIR spectrophotometer, and fluorescence emission of all the samples were recorded using a spectrofluorometer. For the relative Φ_s , the λ_{ex} and λ_{Abs} used were 680 nm. The Φ_s of the ICGNios were compared with free ICG based on the absorption and fluorescence spectra. The relative Φ_s was calculated using equation (ii):

$$\frac{\Phi_s}{\Phi_{Sref}} = \left(\frac{A_{Sref}}{A_s} \right) \times \left(\frac{F_s}{F_{Sref}} \right) \times \left(\frac{\eta_s}{\eta_{Sref}} \right)^2 \dots \dots \dots \text{(ii)}$$

Where the Φ_s and Φ_{Sref} is the quantum yield of the test (ICGNios in water) and reference (free ICG in water) samples, respectively; F_{Sref} and F_s represents the area under the fluorescence emission curve of reference and test samples, respectively; A_s and A_{Sref} represents absorption of test and reference samples at excitation wavelength, and η_{Sref} and η_s denotes a refractive index of the reference and test samples. The Φ of free ICG and ICGNios in ultrapure water is determined by comparison with a freshly prepared ICG as a standard ($\Phi_{Sref} = 0.016$).

2.3.6 Photostability study

The photostability study of free ICG and ICGNios was performed by incubating samples under the exposure of ambient light. The experiment was done by incubating samples under the ambient light (Philips fluorescent lamp) at a distance of 15 cm. Further, both ICG and ICGNios, the absorbance was measured at various time points (0, 2, 4, 12, 24, and 48 h) utilizing a UV/Vis/NIR spectrophotometer. The percentage of stable ICG was calculated using equation (iii):

$$\% \text{ of stable ICG} = \frac{\text{Absorbance of ICG at each time point}}{\text{Absorbance of ICG at initial time point}} \times 100 \dots \dots \dots \text{(iii)}$$

2.3.7 Storage stability study

For storage stability assessment, free ICG (5 μM) and ICGNios were incubated at 4° C temperature for 30 days. Both samples' absorbance was taken on 0 days and 30 days, and their stability in terms of percentage was calculated.

2.3.8 Cell culture

HeLa cells were utilized for *in vitro* NIR imaging. The cells were cultured in DMEM media constituting 100 units/mL penicillin-streptomycin and 10% FBS and were incubated at 37 °C in CO₂ incubator. Cells were then sub-cultured using 0.25% trypsin-EDTA, when cell density reached ~80% confluency.

2.3.9 MTT assay

For the experiment, 1×10⁴ cells/well of Hela cells were seeded in 96-well plates and incubated at 37 °C in a CO₂ incubator for 24 h. Different concentrations (0.5 μM – 100 μM) of empty niosomes and ICGNios were added in wells in triplicates for 24 h. Following incubation, MTT (0.5 mg/ml in PBS) was add up to each well and incubated in a 5% CO₂ incubator at 37 °C for 4 h. The supernatant was then discarded followed by addition of 100 μL DMSO. Formation of formazan was quantified by obtaining the absorbance at a 570 nm wavelength utilizing a microplate reader. Control samples were as follows: Positive control (PC)= cells+ solubilizing buffer (10% SDS and 0.1 N HCL) +MTT+ DMSO and control= cells + MTT. Further, viability of the cells was determined by using equation (iv).

$$\text{Cell viability (\%)} = \frac{(\text{absorbance of treated cells})}{(\text{absorbance of control cells})} \times 100 \dots \dots \dots \text{(iv)}$$

2.3.10 *In vitro* NIR bioimaging using free ICG and ICGNios

The cellular uptake of ICGNios by HeLa was evaluated by NIR bioimaging. The cells were seeded in six well plate placed with glass coverslips at a cell density of 1×10^5 cells per well and incubated at 37 °C for 16 h for adherence. The next day media was replenished with fresh media and treated with ICGNios and free ICG samples for 4 h. For control (untreated cells), the cells were incubated with plain media for 4 hours. Further, the media was discarded, and the cells were washed using $1 \times$ PBS. Further cells were fixed using 4% paraformaldehyde for about 20 minutes. Nucleus of the cells was stained utilizing DAPI for 5 minutes. The slides were prepared by placing coverslip onto mounting media and NIR imaging was done using Nikon Eclipse inverted microscope using mercury and xenon lamps.

2.3.11 *Ex vivo* NIR imaging for tissue depth penetration

Chicken breast tissue samples of ~1 cm thick were used to assess fluorescence detection of ICG and ICGNios through the tissue. The capillary tubes (CT) with 1 mm inner diameter were filled with ICG (10 μ M), and ICGNios (comprising equal amount of ICG) were placed above the tissue sample. Bright-field and NIR images were captured using Nikon Eclipse inverted fluorescence microscope using $5 \times$ objective lens.

2.3.12 Construction of plasmid and bacterial strain

The VSV-G gene was PCR amplified utilizing pVSVFL (+) vector as a template and primers mentioned in the **Table 2.1** using the Q5 High-fidelity polymerase. The amplified gene product was then cloned at the EcoRI and XhoI restriction sites of pCAGGS vector and amplified by transformation in *E. coli* (DH5 α) bacteria.

S.No.	Primer name	Sequence (5'-3')
1	Forward primer	ATAATATGAATTCACCGCCATGAAGTGCCT TTTGTACTT
2	Reverse primer	ATATATCTCGAGTTACTTTCCAAGTCG

Table 2.1 *The primers utilized for PCR amplification of VSV-G gene.*

2.3.13 Cell culture and VNPs purification

The HEK293T cells were grown in DMEM media constituting 10% FBS and 100 U/mL penicillin-streptomycin and incubated in 5 % CO₂ incubator at 37 °C. For experiment, cells were seeded in a 100 mm dish at a cell density of 2.2×10^6 . Following the day, HEK293T cells were transfected with pCAG-VSVG vector using lipofectamine reagent. After transfection, the supernatant was collected and fresh DMEM was added. The supernatant was collected every 24 h and stored at -80 °C. For VNPs purification, the supernatant was thawed and centrifuged at low speed to pellet down cell debris. The supernatant obtained was layered onto 20% sucrose cushion and ultracentrifuged at 25,000 rpm for 2 h. The pellet constituting VSV-G VNPs was then resuspended in 1× PBS (pH 7.4) and put in storage at -80 °C.

2.3.14 Western blot analysis

The expression of VSV-G protein in the transfected cell lysate and purified conditioned media was analyzed by Western blot technique by utilizing anti-VSV-G antibody (1:1000) followed by the horseradish peroxidase (HRP)-tagged secondary antibody. The VSV-G protein bands was detected in the Chemidoc LAS4000 system (GE LA) using chemiluminescence method.

2.3.15 Fabrication of NAVNs

For fabrication of NAVNs, the purified VNPs (10 µg/mL) were incubated with free ICG (12.5 µM) in DI water for 1 h. The unencapsulated ICG was separated by pelleting the NAVNs by ultracentrifugation at 1,00,000 g for 2 h. The pellet comprising NAVNs was resuspended in 1× PBS, and the supernatant constituting untrapped ICG was utilized for estimation of the EE.

2.3.16 Quantification of EE

For determining EE, the absorbance of untrapped ICG was quantified after pelleting down NAVNs. The concentration of the ICG was determined by obtaining the absorbance of the supernatant using the calibration curve of ICG. The EE was further calculated by equation (v).

$$EE \% = \left(\frac{\text{Initial amount of ICG used for NAVNs fabrication} - \text{amount of untrapped ICG in supernatant after centrifugation}}{\text{Initial amount of ICG used for NAVNs fabrication}} \right) \times 100$$

..... (v)

2.3.17 Morphological characterization

The morphology of NAVNs and VNPs was evaluated by TEM operating at a voltage of 200 kV. For the experiment, samples were put onto copper grid and dried for 5 min. Then the grids were rinsed with DI water, wicked dried, and stained with uranyl acetate (2%) for 5 min. The zeta potential and Dh of NPs were studied using a DLS system.

2.3.18 Spectroscopic analysis

The absorption spectra of free ICG (9 µM), VNPs (10 µg/mL) and NAVNs (equal to free ICG), were performed using a UV/vis/NIR spectrophotometer. The fluorescence spectra of all samples were obtained using spectrofluorometer by exciting with a 400 W Xenon lamp. Further, the fluorescence data were collected by FluorEssence software and analyzed using Origin software.

2.3.19 Photostability study of NAVNs

The photostability study of free ICG and NAVNs was performed by incubating samples in ambient light for 72 h. The fluorescence emission of the samples at distinct time points was measured by a spectrofluorometer with the λ_{ex} 680.

2.3.20 In vitro release study of NAVNs

The ICG release profiles from NAVNs were studied by the dialysis method. For this, the NAVNs were suspended in 1 mL of 1× PBS and sealed in a dialysis membrane (12 kDa cutoff). Subsequently, the dialysis bag was submerged in 5 mL of 1× PBS with continuous stirring at 100 rpm. At different time intervals, 1 ml of the solution outside of the dialysis bag was obtained for absorption measurement with the replacement of the same volume of fresh 1× PBS. The percentage (%) of ICG released from NAVNs was quantified by measuring the absorption at 778 nm using a microplate reader.

2.3.21 VSV-G VNPs cellular uptake assay

For the experiment, HeLa cells were seeded in 24-well plates having glass coverslips. The next day, cells were incubated with VSV-G VNPs diluted in Opti-MEM at a concentration of 10 $\mu\text{g}/\text{mL}$ for 4 h. After incubation, cells were rinsed with 1× PBS and fixed with 4 % paraformaldehyde for 20 minutes. Fixed cells were then incubated with anti-VSV-G primary antibodies of 1:200 dilutions. Cells were then washed and incubated with the FITC-conjugated secondary antibody of 1:1000 dilution for 1 h. For nucleus staining, the cells were incubated with Hoechst 33342 dye for 5 min. The coverslips were then placed over a glass slide having mounting media and imaged using fluorescence microscopy at the magnification of 10 \times .

2.3.22 MTT assay

For cell viability assay, the HeLa cells were seeded in 96 well plate at a density of 5000 cells/well. The cells then treated with different concentrations of NPs in

triplicates for 24 h. Following day, the fresh media comprising MTT of 0.5 mg/mL is added into each well and incubated for 4 h. Further, the media is removed, and DMSO was added to suspend the formazan. For quantification, the absorbance at 570 nm wavelength was measured by a UV/vis microplate reader. The cell viability was then calculated using equation (iv).

2.3.23 NIRF bioimaging

HeLa cells were seeded in 12-well plates at a cell density of $\sim 0.1 \times 10^6$ cells/well onto coverslips. The next day, the cells were treated with free ICG (3 μ M) and NAVNs (encapsulated with an equal concentration of ICG) for 4 h. Following incubation, the cells were washed with 1 \times PBS and incubated with Hoechst 33342 dye for nuclei staining. The fixation of cells was done with 4% paraformaldehyde followed by washing with 1 \times PBS. The slides were prepared using mounting media. The NIR imaging was performed using a Nikon Eclipse Ti-U inverted microscope with 40 \times magnification. For bioimaging, the cells were excited using the mercury lamp for Hoechst dye and the xenon lamp for ICG.

2.3.24 VSV isolation

One day prior to the virus infection, BHK-21 cells were seeded in a 10 cm cell culture dish. The following day, the cells were infected with VSV for 16 h with a multiplicity of infection (MOI) of 1. The supernatant from the infected cells constituting the virus was purified and pelleted by ultracentrifugation at 1,00,000 g for 2 h. The purified VSV was then resuspended in 1 \times PBS and stored at -80°C .

2.3.25 Plaque assay

Virus titer was estimated using the plaque assay method. One day before virus infection, the Vero cells were seeded in six-well plate with 80% confluency. The next day, the cells were infected with 10-fold serial dilutions of viral stocks for 45 min. After discarding the virus constituting media, the infected cells were overlaid with 1%

agarose. After 24 h the plaques were fixed and stained using glutaraldehyde containing 1% crystal violet. Subsequently the plaques were counted manually.

2.3.26 Determination of immune response gene expression by quantitative real-time PCR (qRT-PCR)

The mouse embryo fibroblasts (NIH/3T3) cells were plated on to a 6-well plate and incubated for 16 h. The cells were then given treatment with NAVNs (20 µg) for 24 h. For positive control, the cells were infected with VSV at a MOI of 0.01. After 24 h of infection, the cellular mRNA was extracted using the Trizol reagent. Then, 1 µg of mRNA was reverse transcribed by the iScript cDNA synthesis kit. Consequently, the RNA inactivation was done by incubating at 70 °C for 5 min. qRT-PCR was performed using 1:10 dilution of the cDNA and primers mentioned in **Table 2.2** using iTaq SYBR green supermix. Normalization of all the samples for relative quantification was done by the $2^{-\Delta\Delta CT}$ method using the housekeeping β -actin gene.

S. No.	Primer Name	Sequence (5'-3')
1.	IFN β Forward primer	CATCAACTATAAGCAGCTCCA
2.	IFN β Reverse primer	TTCAAGTGGAGAGCAGTTGAG
3.	IRF-3 Forward primer	CACAAGGACAAGGACGGAG
4.	IRF-3 Reverse primer	ATGCAGAACCACAGAGTGTAG
5.	IFN γ Forward primer	TCA AGT GGC ATA GAT GTG GAA
6.	IFN γ Reverse primer	TGG CTC TGC AGG ATT TTC ATG
7.	β -actin Forward primer	GCCTTCCTTCTTGGGTATGG
8.	β -actin Reverse primer	GCACTGTGTTGGCATAGAGG

Table 2.2 The sequence of IFN β , IRF3, IFN γ and β -actin gene primers used for qRT-PCR.

2.3.27 Animal experiment and histopathological Evaluation

Nine female BALB/c mice were split into three different groups, i.e., control and treated (1 day and 7 days post-injection; n = 3/group). The test group was injected intraperitoneally with VNPs at a concentration of 1 mg/kg body weight dose, and control animals were injected with PBS. During the study time interval, bodyweight of all the animals was assessed daily. The test group animals were sacrificed on the first- and seventh-day post-treatment, while the control groups were sacrificed on seventh-day post-injection. After sacrifice, the visceral organs, such as liver, spleen, kidneys, and lungs, were harvested and processed for histopathological assessment. The tissue section was fixed using neutral buffered formalin solution (10 %) and embedded in paraffin blocks. Then the paraffin blocks were sliced with 5- μ m-thickness using a Leica RM2125RT microtome and placed over a microscope slide. The tissue sections were stained with hematoxylin and eosin (H&E) dye and analyzed for any histological changes using a Leica DM500 microscope at the magnification of 40 \times . Three slides per block were evaluated for histological alterations of the sectioned tissues.

2.3.28 *In vivo* NIR imaging and biodistribution study

NAVNs and free ICG solution is administered intravenously in BALB/c mice through tail vein injection under the anesthetized condition. The concentration of free ICG and NAVNs administered is 3mg/kg bodyweight of the animal. The injection volume of the sample is 150 μ L. After injection, fluorescence images will be acquired at 24 h and 48 h. The imaging parameters were: $\lambda_{\text{ex}} = 745$ nm and $\lambda_{\text{em}} = 840$ nm with the exposure time of 2 to 6 s. For the biodistribution study, mice will be sacrificed at 48 h post-injection.

2.3.29 Spectroscopic analysis

A UV-Vis-NIR spectrophotometer was used to examine the encapsulation of ICG by absorption measurement of NAVNs (loaded with an equivalent concentration

of free ICG) and free ICG (35 μM) and. Further than, the fluorescence emission of NAVNs and ICG (35 μM) were measured using a spectrofluorometer equipped with a 400-Watt xenon lamp for excitation (λ_{ex} 680 nm and λ_{ex} 420 nm). The spectral data were recorded utilizing FluorEssence software, and all the data were analyzed using Origin 2021b software.

2.3.30 Two-photon excitation (TPE) fluorescence imaging of free ICG and NAVNs treated HeLa cells

The HeLa cells were cultured as a monolayer in DMEM medium in a 5% CO₂: 95% humidified incubator adjusted at 37°C. Further, the cells were plated onto coverslips containing six-well plate ($\sim 1.5 \times 10^5$ cells/well) and incubated for 16 h. Next day, the cells were treated with NAVNs and free ICG (3 μM). The control cells were incubated with DMEM media. After treatments, the cells were incubated in humidified incubator at 37 °C for 4 h for cellular uptake of ICG and NAVNs. Further, cells were fixed using 4% paraformaldehyde and slides were made using mounting media. The multi-photon imaging was done with multiphoton confocal microscopy. The multi-photon imaging system is equipped with the femtosecond negative chirped infrared (IR) laser. A mode-locked Ti(Titanium):Sapphire laser (Mai Tai, Deep-See, Spectra-Physics) was employed as an excitation source which gives ~ 70 femtoseconds (fs) pulse with a repetition rate of 80 MHz with the wavelength range of 690 to 1064 nm . *In vitro* TPE fluorescence images of NAVNs and free ICG incubated cells were recorded using non-descanned detectors, with a bandpass filter to collect emission in the range of 590-670 nm related to the collection window ($S_2 \rightarrow S_0$ state transition of ICG).

2.3.31 TPE fluorescence imaging of chicken breast tissue

Ex vivo TPEF imaging was done in chicken breast tissue to mimic the biological environment. 3 different tissue samples of the same dimension (~ 350 μm thickness) were cut using a surgical scalpel and transferred into Nunc chambered cover glass for the experiment. NAVNs (with an equivalent concentration to free ICG of 20 μM), free

ICG (20 μM), and 1 \times PBS were applied on the tissue surface. The tissue samples were kept unperturbed for 30 minutes and then washed with 1 \times PBS for removal of unbound samples. Subsequently, the TPEF images of tissue samples were captured using multiphoton confocal laser scanning microscopy. The imaging parameters for the TPE fluorescence imaging is λ_{ex} 790 nm with an emission collection wavelength range of 575 nm to 630 nm. The Z-scanning parameters are as follows: Z-dimension is 4423.53-4038 μm , 0.5 $\mu\text{m}/\text{slice}$. TPE images were processed by the Olympus Fluoview version 4.2. software and analyzed using ImageJ software.

2.4 Instrumentation and techniques

2.4.1 Western blotting

Western blotting is routinely used to detect an expression of a protein of interest. As seen in **Fig. 2.1**, the Western blot technique constitutes three main steps: protein separation using SDS-PAGE, transferring proteins to solid supports such as Polyvinylidene fluoride (PVDF) or nitrocellulose membranes, and detecting the proteins using primary and secondary antibodies. The treatment with primary antibodies followed by secondary antibodies detects and visualizes only a specific protein band with a chemiluminescent substrate. Protein concentration in a sample is directly proportional to the thickness of the bands. For confirmation of the protein expression, positive and negative controls are often run with the protein samples. Purified target proteins can be used as positive controls to demonstrate the sensitivity of the antibody and the specificity of the target protein. Constitutively expressing proteins, such as GAPDH or β -actin, can be used as negative controls to determine the non-specificity of the protein bands. A change in protein expression is often compared with that of negative control since the expression of the target protein may change with treatment while that of the control protein will remain unchanged. It, therefore, provides a relative comparison between the protein levels and is not an exact method of measuring protein concentrations.

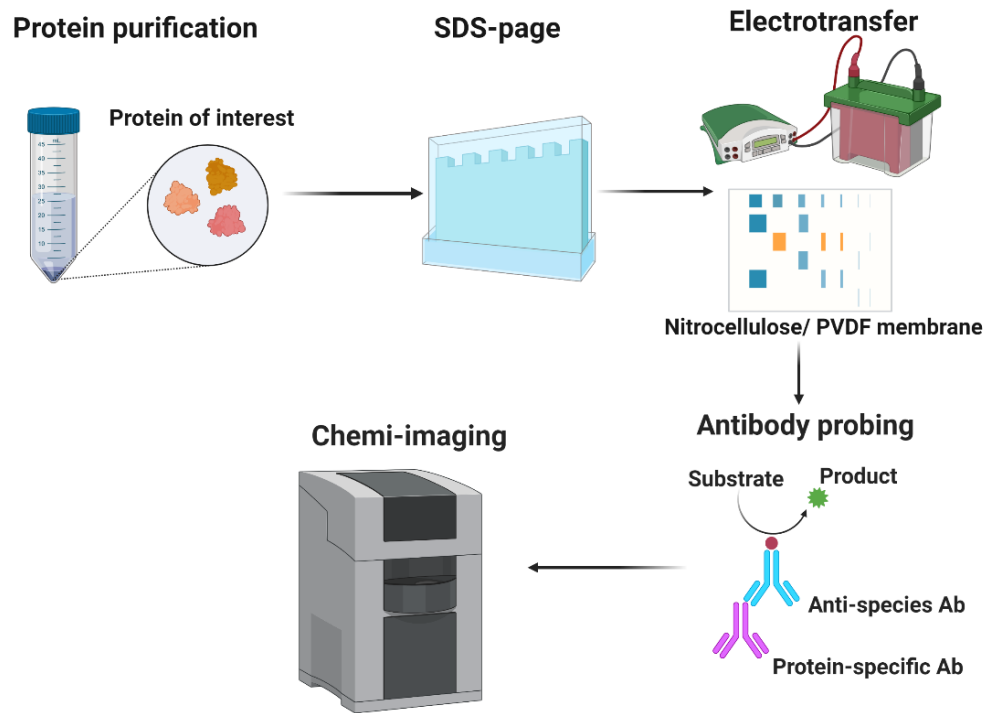


Figure 2.1 Schematic illustration of western blotting technique. For the western blotting technique, the desired purified protein is separated by gel electrophoresis according to its molecular mass. The proteins are transferred from the SDS gel onto a membrane. Afterward, the membrane with proteins is incubated with the gene specific primary antibody followed by HRP tagged secondary antibody. The secondary antibody catalyzes an enzymatic reaction with the substrate, which is detectable through a digital imager.

2.4.2 Quantitative real-time polymerase chain reaction (qRT-PCR)

qRT-PCR method serves as an advanced version of PCR. During each PCR cycle, the amplified products can be detected and quantified in real-time. Using cellular RNA as a template material, complementary DNA (cDNA) is first synthesized with the aid of reverse transcriptase and then used as a qPCR template for DNA synthesis. As illustrated in **Fig. 2.2**, the basic PCR procedure comprises three stages: denaturation, annealing, and extension. Prior to qRT-PCR, cellular RNA is converted into cDNA, and fluorescence tags are utilized to enable real-time data analysis. RT-PCR mainly uses probe-based and dye-based qPCR methods. An oligonucleotide

probe is used for the TaqMan method since it comprises a 5' fluorescent reporter and 3' quencher dye. By virtue of fluorescence resonance energy transfer (FRET), the reporter dye emits comparatively diminished fluorescence due to its proximity to the quencher dye. Following annealing of the probe to the template sequence downstream of the primer site, the Taq DNA polymerase extends the primer. This is followed by cleavage of the probe by the Taq polymerase's 5' nuclease activity. Due to the reporter's and quencher dyes' separation, a high level of fluorescence is emitted, and its intensity is directly proportional to the amplicon's amplification. In SYBR green method, the dye specifically binds to double-stranded DNA (ds DNA). The fluorescent intensity increases as the copy number of ds DNA multiplies during PCR reaction, as the dye binds to these amplified products and emit fluorescence. Hence, the fluorescence emitted by the dye directly correlates with the number of amplified products. The SYBR green-based RT-PCR is one of the most common methods for quantifying RNA since it is cost-effective and does not require sequence-specific primers like TaqMan.

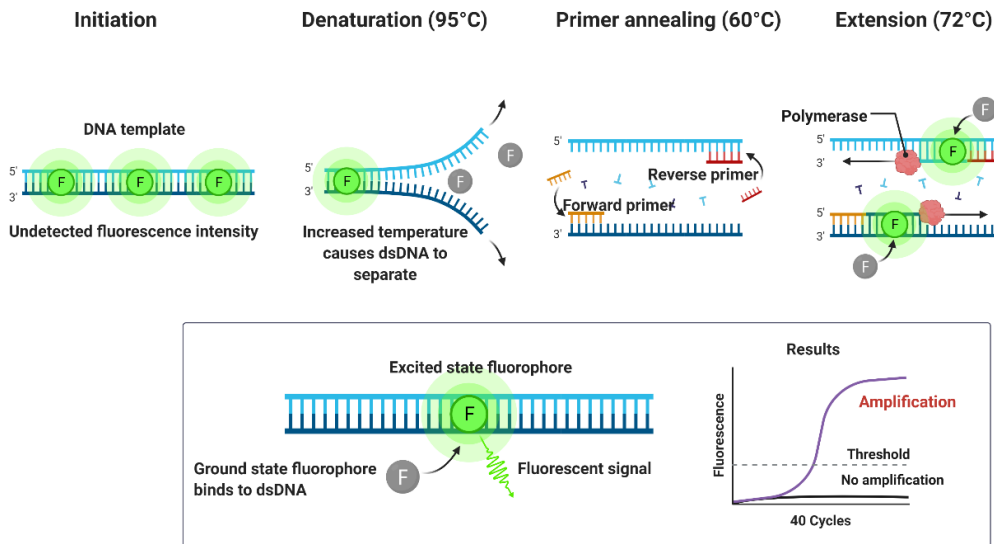


Figure 2.2 A schematic depicting the qRT-PCR principle. The template RNA is converted to cDNA by reverse transcriptase and amplified using PCR by denaturation of cDNA at 95 °C, annealing the primers and probe to the denatured cDNA at 60 °C followed by the final extension at 72 °C. The RNA is quantified by the intensity of fluorescent signals produced during amplification of cDNA.

2.4.3 UV-Vis-NIR absorption spectroscopy

When radiation encounters the material, it can be scattered, emitted, or absorbed. The absorbed radiation gives rise to the branch of spectroscopy called absorption spectroscopy. It is an analytical chemistry technique that can determine the concentration of the absorbing chromophores in solutions.[136] This is a non-destructive method used by biologists, biochemists, and systems biologists to evaluate molecular, biological, and functional properties. This approach assesses radiation absorption as a function of frequency or wavelength due to its interaction with material across the electromagnetic spectrum. The most typical configuration, as displayed in **Fig. 2.3** produces a beam of radiation upon a sample and measure the intensity of the radiation that passes through it. A fraction of electromagnetic radiation pass by a transparent material, and some portion of it is absorbed by the samples. Because of the energy absorption, molecules, or atoms transit from their lower energy level (S_0) to a higher energy state (S_1). The radiation absorbed by the samples has energy equivalent to the energy difference between its excited state and ground state.

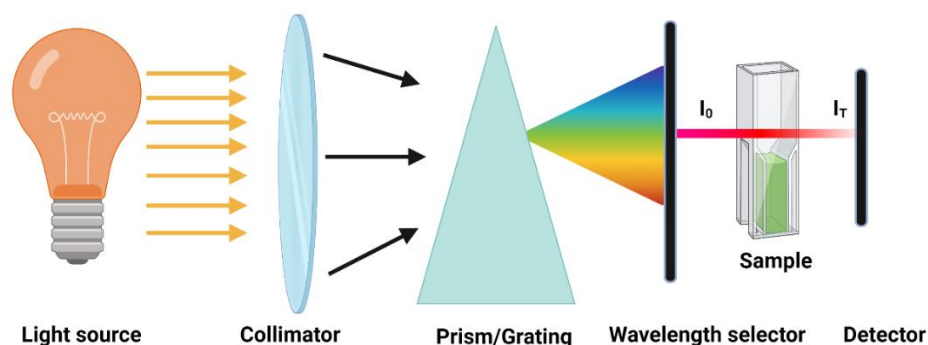


Figure 2.3 Ray diagram depicting the working of the absorption spectroscopy. The absorption spectrophotometer uses a light source and an excitation monochromator to select a specific wavelength of light that hits the sample. The sample reflects or transmits light. A detector is used to detect the intensity of light transmitted or reflected.

This thesis employed UV-Vis-NIR absorption spectroscopy to analyze biomolecules quantitatively and qualitatively by spectrophotometer. UV-Vis-NIR absorption spectroscopy works on the movement of electrons from one chemical orbital to another produced by electromagnetic radiation absorption in the UV-Vis-NIR (200 to 1000 nm) range. UV-Vis-NIR spectrophotometers function on the Beer-Lambert law concept. According to Lambert's law, when a monochromatic light flows through a transparent medium, the intensity of the light drops exponentially as the thickness of the absorbing substance grows.[137] In contrast, Beer's law, says that the absorbance of a radiation by sample in a homogeneous isotropous medium is proportional to the path length and concentration of the samples.[138] As a result, the Beer-Lambert equation is applied to determine the amount of light absorbed by the sample, as shown in equation (vii).

$$A = -\log \frac{I_T}{I_0} = \epsilon cl$$

..... (vii)

Where A is the absorbance (optical density), I₀ and I_T are the incident and transmitted light intensities for a particular wavelength. The proportionality constant ε is referred to as the molar extinction coefficient (M⁻¹ cm⁻¹), l is the sample cell's route length (in cm) and c is the sample's molar concentration (M, or mol/L).

A UV-Vis-NIR spectrometer generally consists of a light source to create the broad wavelength light and a lens to concentrate that light on the grating, which splits the white light into distinct wavelengths. In addition, the wavelength selector (slit) chooses the specific wavelength of light that is emitted on the sample. A photomultiplier tube detector (PMT) recorded the sample's absorbed wavelengths, which transforms the light into an electrical wave.

2.4.4 Fluorescence spectroscopy

Fluorescence spectroscopy, also known as fluorimeter or spectrofluorometric spectroscopy, is an electromagnetic spectroscopy technique used to examine the

fluorescence of a substance. As shown in **Fig. 2.4**, xenon lamp is mainly used in the spectrometer. Variable excitation wavelengths from 200 to 700 nm can be achieved by an excitation monochromator. All-reflective optics inside the fluorimeter compartment guarantees that the fluorescence signals collected will not be affected by the light illumination level. The emission monochromators with wavelength range from 300 to 1000 nm is used for collecting emitted photons. Fluorescence spectroscopy measures the fluorescence emitted by a fluorophore based on its optical properties. When atoms or molecules reach a high energy level, they can decay by releasing radiation at a lower energy level.[139] In addition, when the electron absorbs a photon, it is activated and returns from the S_1 to S_0 state, resulting in the fluorescence emission. Non-radiative processes such as transitional and vibrational states always cause some energy wasted in the excited state. As a result, the energy of emitted light is always less compared to the energy of absorbed light; hence fluorescence occurs at a longer wavelength than absorption. In general, electrons stimulated to higher energy levels following light absorption are unstable and return to the S_0 state via the radiative or non-radiative process. Fluorescence is a radiation-emitting process in which the molecule transits from a higher singlet electronic (S_n) state to a lower singlet electronic (S_0) state. Because of energy loss, fluorescence emission always has a redshift concerning the absorption wavelength, and this wavelength shift is known as the Stokes shift. According to Kasha's rule, fluorescence emission always happens when electron from the excited S_1 state relaxes to the S_0 state.[140]

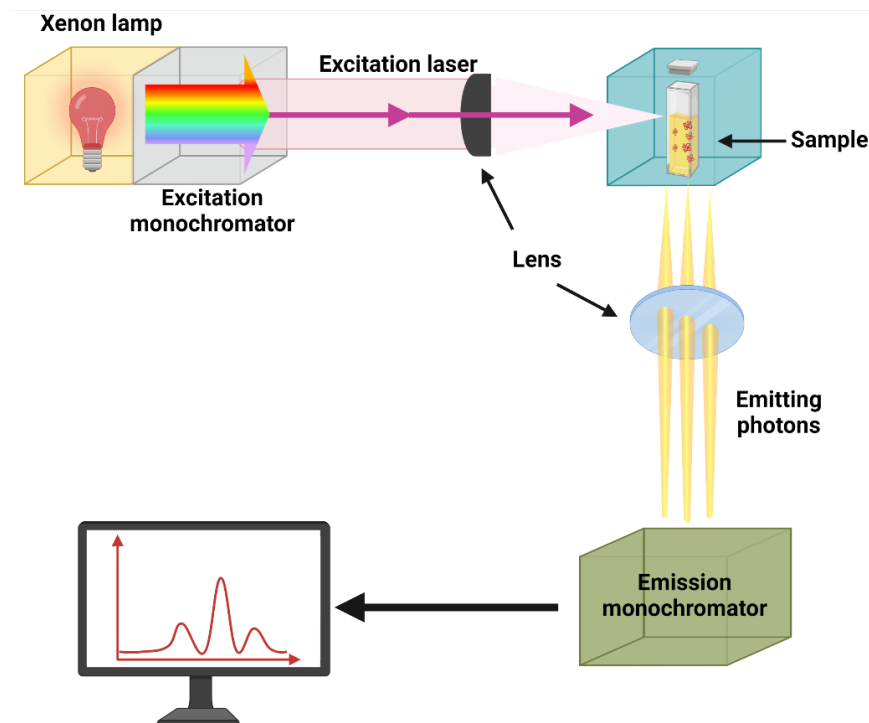


Figure 2.4 Schematic depiction of the fluorescence spectroscopy setup. The spectrofluorometers consist of light sources, monochromators, optical filters, and detectors to record fluorophore's excitation and emission spectra.

2.4.5 Dynamic light scattering (DLS) spectroscopy

DLS also termed as photon correlation spectroscopy (PCS) is a light scattering method for analyzing the size distribution of tiny particles in suspension or polymeric solution. As depicted in **Fig. 2.5**, this technique determines the hydrodynamic size by scattering light through a colloidal solution and analyzing variations in scattered intensity over time.[141]. Floating particles are subject to Brownian motion in the presence of random collisions among molecules in the solvent. Brownian motion of particles is proportional to their hydrodynamic diameter. Smaller particles diffuse faster, and the DLS device produces a correlation function based on particle size and time-dependent light scattering capacity. The laser beam is dispersed in all directions when it hits the sample in the cuvette. The scattering angle and detection apertures define this volume. The perceived intensity of scattered light at any given time depends, however, on the relative locations of the particles that interfere with the

scattered light. If the particles are moving in solution, their close locations will vary over time, causing variations in the scattered light intensity to be detected. Because the particles are in Brownian motion and travel randomly, the fluctuations in scattered light intensity are also unpredictable. The changes will occur quickly for smaller, faster-moving particles and slowly for bigger, slower-moving particles. The light intensity data is collected over time and is regulated by a digital correlator. The raw data is utilized to compute the autocorrelation function, and then used to calculate the mean diameter or particle size distribution.

DLS is also used to determine the zeta potential (surface charge) of the material. Particles are thought to be in a liquid and move with the ions in the Stern layer near the particle surface and with a portion of the diffuse layer. The electromagnetic field that causes this movement is known as the slipping plane. The zeta potential is described as the potential in close proximity to the sliding plane, whereas the potential distance from the particle surface is specified as zero. When the potential is high, the particles are monodispersed and do not combine due to strong electrostatic repulsion between them. On the other hand, a low value (close to zero) increases the likelihood of particles interacting and creating particle aggregates. As a result, DLS is also utilized to measure the particles' dispersion stability.

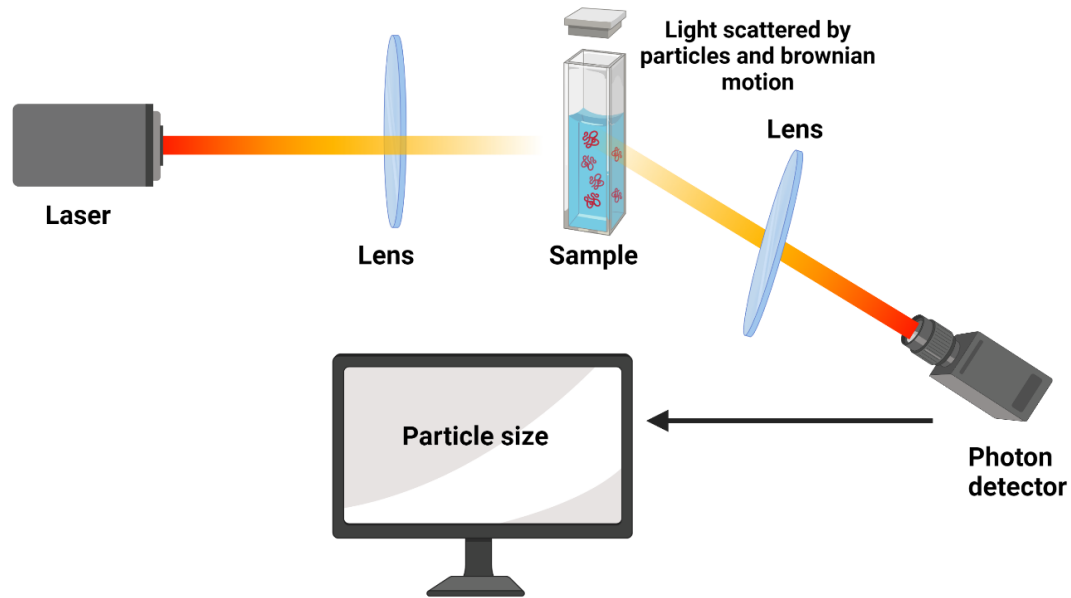


Figure 2.5 Schematic of the working principle of DLS for particle size information. The sample contained in a cuvette is illuminated with a laser. Interaction with the sample scatters incident light in every direction. At a certain angle, the scattered light is detected at a certain angle which is used to calculate the particle size and diffusion coefficient.

2.4.6 Field-emission scanning electron microscopy (FESEM)

The FESEM characterization method provides information about surface morphologies, such as the shapes and sizes of materials. As illustrated in **Fig. 2.6**, this technique produces images by deflecting an electron from the object's outer surface. The scanning electron microscope generates signals based on electron interaction using kinetic energy.[142] To examine crystalline elements and photons, backscattered electrons, secondary electrons and diffracted backscattered electrons are utilized. The image of particles was created by backscattered and secondary electrons. The secondary electrons released from the specimen are responsible for detecting the shape and topography, while backscattered electrons generate contrast in the sample components.[143]

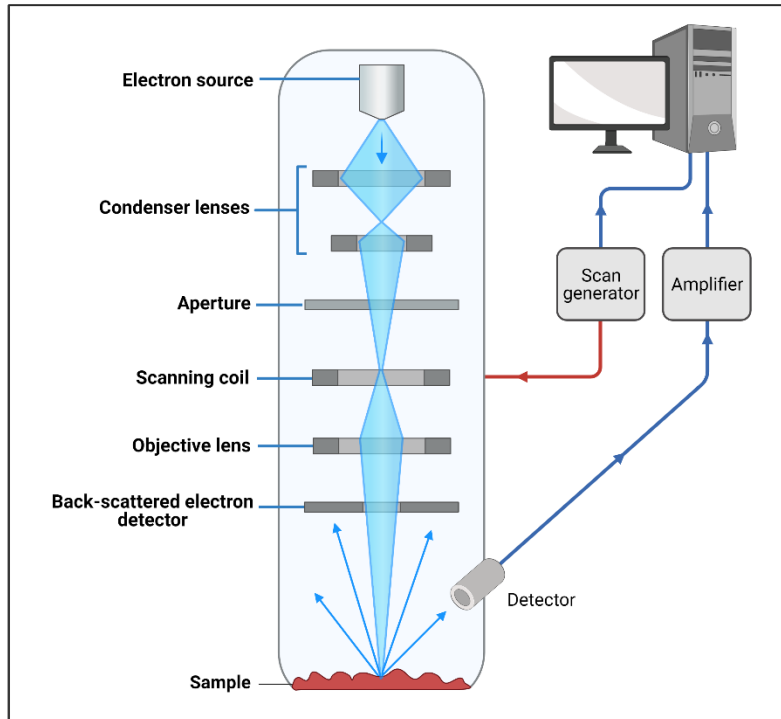


Figure 2.6 Ray diagram of working principle of the FESEM. FESEM produces images of specimens using a focused beam of electrons. A primary electron beam generates secondary electrons and backscattered electrons as it strikes the sample. Detectors capture these electrons and produce signals to create images of the sample.

2.4.7 Transmission electron microscopy (TEM)

The TEM is an excellent technique for examining the interior structure of many biological materials, including cells. As shown in **Fig. 2.7**, the TEM utilizes an electron particle beam to generate an enlarged image of particles. Electron gun releases electrons from the top of TEM that pass across the vacuum tube of the microscope. TEM uses electromagnetic lens instead of the glass lenses for concentrating the electron into a narrow beam. This electron beam then travels via thin sample due to which the electrons scatter or strike a fluorescent screen situated at the bottom side of the microscope.[144] The working principle of TEM is similar to the light microscopy, however it uses electrons instead of the light source. Since the electrons have a shorter wavelength than light, the optimum resolution of TEM pictures is higher than that of

a light microscope. A TEM can magnify an image up to 2 million times. Thus, TEMs may disclose the minutest features of the interior structure, even down to individual atoms in some circumstances.

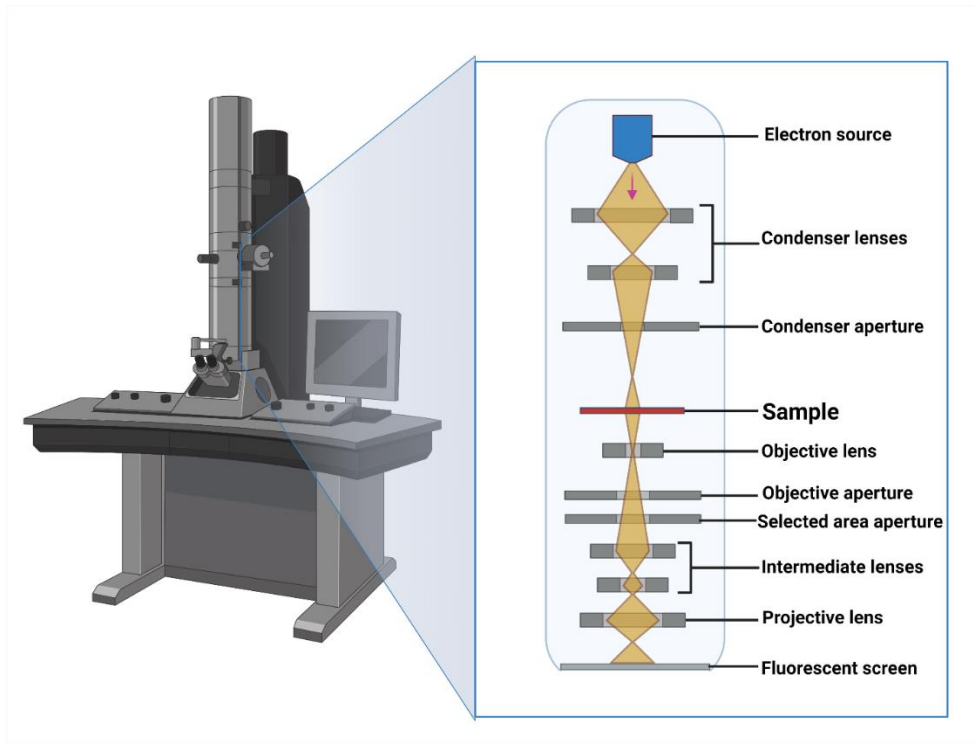


Figure 2.7 Schematic of working principle of typical TEM system. In TEM, electrons are transferred from a gun to the sample, providing a broad or focused beam of light. The ray diagram illustrates the illumination system located above the sample. The stage and objective lens are central components, along with the intermediate and projector lenses.

2.4.8 Fluorescence microscopy

Fluorescent microscopes combine the magnifying power of light microscopy with the ability to visualize fluorescence. Fluorescence is a spectroscopy phenomenon in which substances absorb light at one wavelength while emitting light at another wavelength. Following excitation to a high-energy state (S_n), an electron relaxes to its ground state (S_0) and emits a photon of light. **Fig. 2.8** illustrates the working principle of fluorescence microscopy. In this microscopy technique, the shorter wavelength of

light (UV, blue, or NIR) produced by the lamps (Mercury/Xenon) passes through the excitation filter, which removes non-specific waves of light. The filtered light passes through the dichroic filter and strikes fluorophores. The fluorophore absorbs light energy in its "ground state (S_0)," due to which the molecule's electronic, vibrational, and rotational states may occur. On average, the absorbed energy can shift an electron into a new orbital which is farther from the nucleus. This electron shift to an "excited" state (S_n) occurs in femtoseconds. The excited fluorochromes emit waves of longer wavelengths that pass via the emission filter. The residual excitation light is blocked by the emission filter and the desired emission wavelength is passed to the detector. Further, the fluorescence yield can be quantified by measuring the fluorescence Stokes-shift emitted at the peak wavelength of the fluorescence spectra.[145] Subsequently, the broad spectral ranges of fluorescence microscopy allow the visualization of multiple molecular, cellular, and subcellular structures simultaneously. This thesis employed an inverted microscope (Nikon, model Eclipse Ti-U) for a fluorescence microscopy study. In this microscope, mercury, xenon, and halogen lamps were used as light sources, with filter cubes used to select excitation and emission wavelengths. During this study, fluorescent dyes ICG, DAPI, and FITC were used. The excitation wavelength range for DAPI filters is 349 - 380 nm, while the band-pass filters used in the collection have wavelengths between 435 - 485 nm. Similarly, the FITC has an excitation wavelength range of 465 - 495 nm and a 515 - 555 nm emission collection window. The essential difference is that the NIR excitation filter permits 775 ± 25 nm, whereas the collecting window allows 845 ± 27.5 nm.

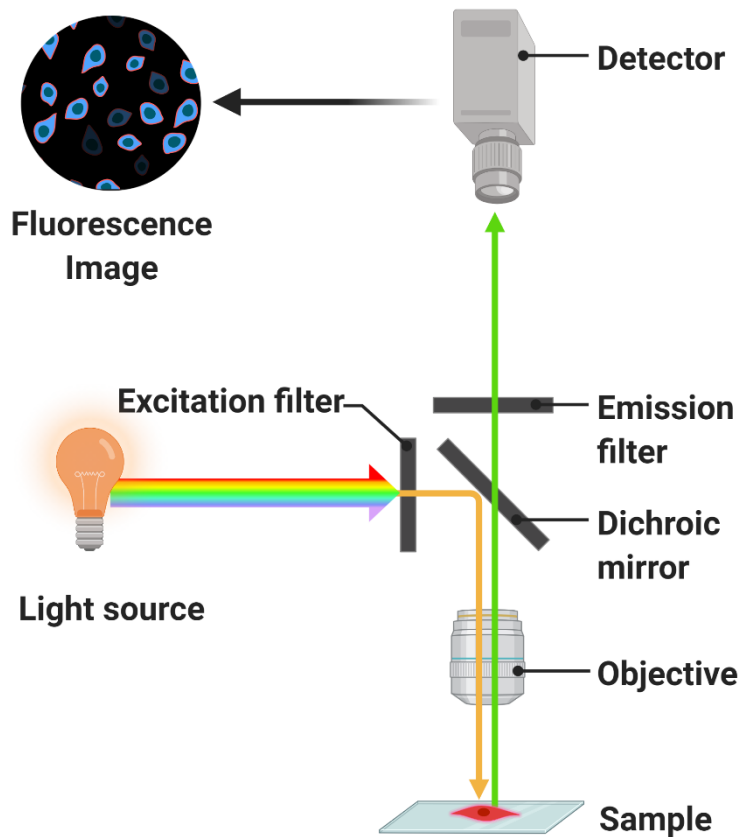


Figure 2.8 Schematic of working principle of fluorescence microscope. An inverted setup using mercury and xenon lamps is shown. In a typical experimental design, the excitation light is centered on the backside of the aperture of the lens to produce uniform light distribution within the sample. The fluorescence emission is collected using an objective lens, uncoupled from excitation light with a dichroic mirror, and imaged using detector (CCD camera).

2.4.9 Multiphoton fluorescence microscopy

A multiphoton microscopy is an important bioimaging technique because it offers lower photon toxicity and superior spatial and temporal resolution compared to other *in vivo* bioimaging modalities. This technique uses sophisticated optical system of a laser scanning microscope and longer nonlinear fluorescence excitation wavelength for obtaining high-resolution and 3D images of fluorescently tagged specimens. This powerful tool can visualize hundreds of micrometers into biological tissues to investigate cellular and subcellular biological processes.[146] It has

numerous benefits over traditional optical microscopy, including the capacity to collect serial optical slices from thick specimens and remove out-of-focus glare.[147] In multiphoton microscopy, excitation occurs only at the focal point of a diffraction-limited microscope, which provides the ability to obtain a 3D resolution from thick biological specimens. Fluorophores are less photobleached due to their highly localized excitation energy. Because multiphoton imaging minimizes photodamage, the subsequent duration of experiments for investigating the properties of live tissues can be extended. Furthermore, NIR wavelength excitations help penetrate deeper into biological tissues and reduce light scattering observed at shorter wavelengths.

Usually, this technique uses two or more photons to create high-resolution, 3D images of microscopic samples. In two photon-excited fluorescence imaging, the two photons are absorbed simultaneously by a sample followed by single-photon emission. Further, the signals absorbed and emitted by biological tissues give information about their structure and processes. As depicted in **Fig. 2.9**, the multi-photon studies in this thesis were carried out using a laser scanning multiphoton confocal microscopy (Olympus, model no. FV1200MPE, IX83, Japan). The multi-photon imaging system constitute femtosecond damaging chirped IR laser. A mode-locked Ti-Sapphire laser was employed as an excitation source, that delivers a pulse width of ~ 70 fs at the repetition rate of 80 MHz with the 690 nm to 1064 nm wavelength range. An acousto-optic modulator was used to make the wavelength selection.

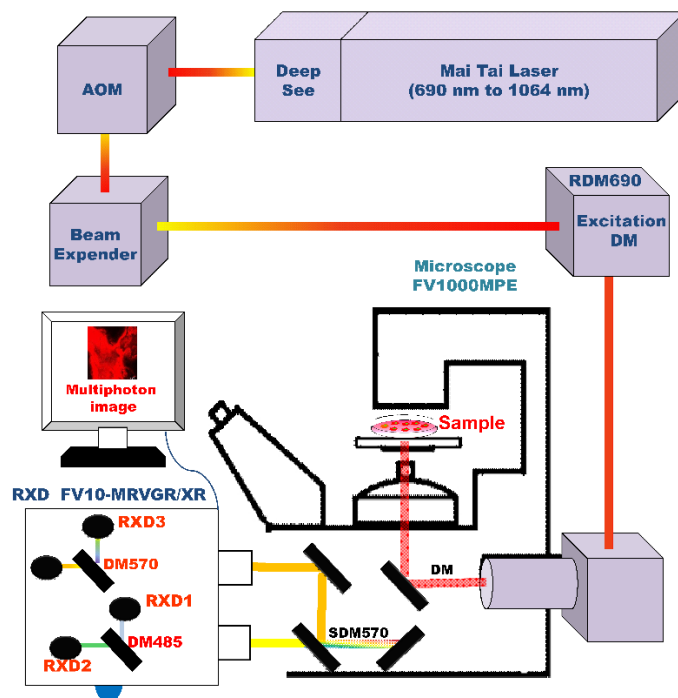


Figure 2.9 Schematic of an Olympus confocal laser scanning microscope equipped with a MaiTai laser for multiphoton bioimaging. The acronym is AOM: Acoustic optical modulator, DM: Dichroic mirror, RXD1: BA420-460nm, RXD2: BA 495-540, RXD3: BA380-560nm, and RXD4 BA575-630nm.

2.4.10 Cell culture

Cell culture is growing cells from plants or animals in a controlled environment generally outside their natural habitat. Cell type and culture medium, which contains nutrients and growth agents, influence cell culture conditions [148]. The physiochemical environment and gases such as CO₂ and O₂ play an essential role in cell growth regulation in an artificial environment. Most cells need a surface or a synthetic substrate to develop monolayer culture, although others can grow freely in culture media. Most cells have a genetically determined lifespan; nevertheless, specific cultivated cells have been "transformed" into immortal cells that will reproduce indefinitely if particular conditions are fulfilled.

2.4.11 Plaque assay

Plaque assays are widely used to determine the amount/titer of infectious viruses in a particular sample. Previously, the plaque assay was used frequently for quantifying infectious bacteriophage virus particles. Later in 1952, the Renato Dulbecco used this assay for use in animal virology. Since then, this assay is used to determine the titers of numerous types of viruses.[149] To determine the virus titer in a particular sample, **Fig. 2.10** depicts the plaque assay approach. In plaque assays, cell monolayers are infected with a lytic virus. The virus is serially diluted to a countable range, typically in between 5 and 100 viral particles. Then the infected host cell monolayers are overlaid with an immobilizing medium for inhibiting viral infection and spreading from one cell to another. After infection and immobilization, individual plaques, or cell death zones, are formed as the surrounding monolayer restricts viral replication and infection. The replication-lysis cycle continues in infected cells, further propagating the infection, increasing clearly defined plaques. The formation of a visible plaque varies based on viral growth kinetics and host cell type. Following the fixation and staining of the monolayer, plaques are counted to obtain a viable viral stock titer (plaque forming unit, pfu) per milliliter by equation **(viii)**

$$\text{Viral titer (PFU/mL)} = \frac{\text{No. of Plaques}}{D \times V} \dots \dots \dots \text{(viii)}$$

Where D is Dilution factor and V is Volume of diluted virus/well

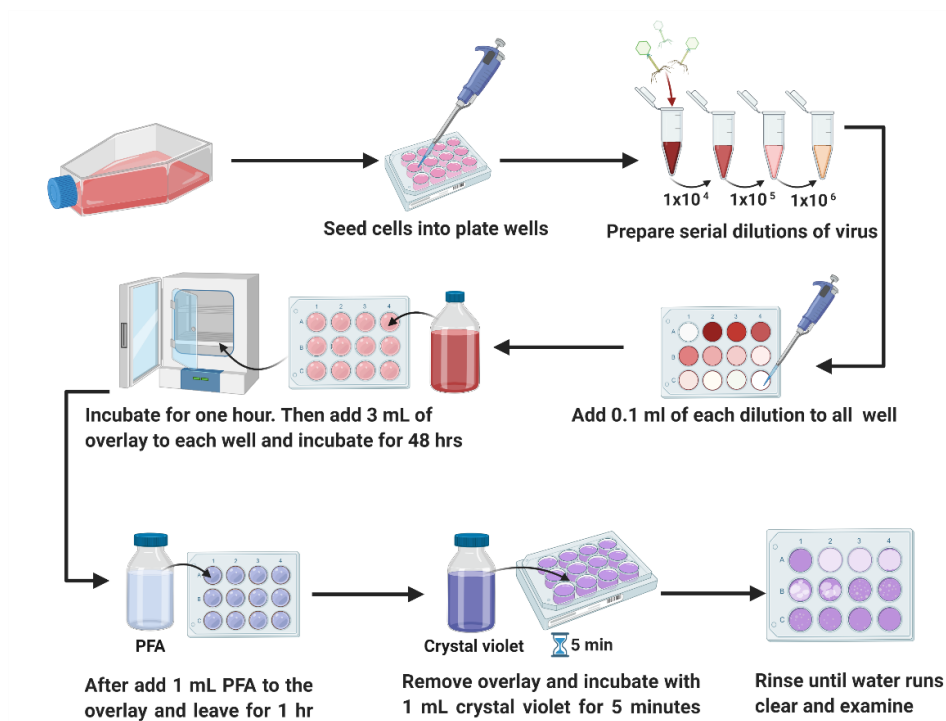


Figure 2.10 Illustration of a plaque assay method for virus quantification. This assay involves infecting host cells with varying dilutions of a virus particles, and covering it using semisolid media, like agar, for preventing indiscriminate spreading of virus.

2.4.12 MTT assay

The MTT test is a quantitative colorimetric assay used to determine the survival and proliferation of mammalian cells. As the mitochondrial activity of cell is directly proportional to the number of viable cells, this test is broadly used to evaluate *in vitro* cytotoxicity of the anticipated drug. The schematic illustration of the principle of MTT assay is shown in **Fig. 2.11**. When mitochondrial succinate dehydrogenase is incubated with metabolically active, living cells, it converts MTT from a bright yellow tetrazolium salt to a dark purple formazan product.[150] MTT is the measurement of a cell's mitochondrial activity, which is constant in virtually all viable cells. The conversion of MTT salt into formazan crystals can be solubilized for homogeneous measurement and is comparable to the mitochondrial activity of cells. MTT penetrates the cells and travels to the mitochondria, where it is converted to a dark purple formazan product that is insoluble. Because these formazans were solubilized in an

organic solvent (such as isopropanol or DMSO), any increase or decrease in viable cell population is quantified by a microplate reader. The cell viability was then assessed using equation (iv).

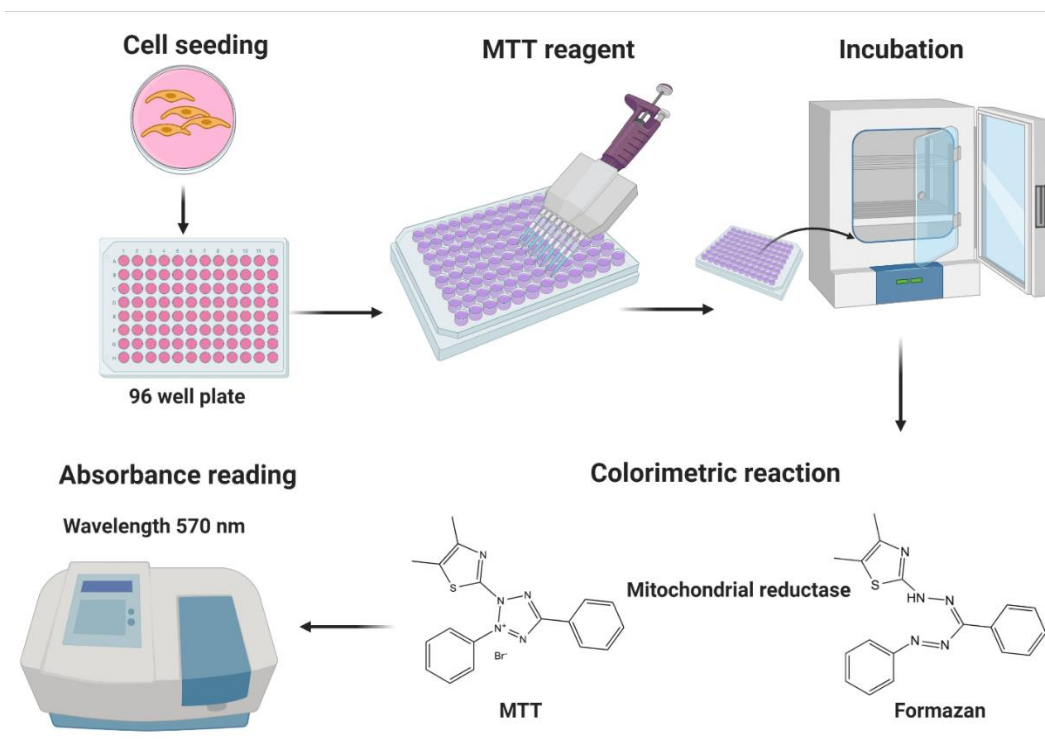


Figure 2.11 Graphic illustration of the principle of MTT assay. MTT involves the reduction of tetrazolium salts to formazan crystals by viable cells, where the number of cells directly correlates with the optical density.

Chapter 3

*Optical Property Enhancing Novel Near-infrared Active Niosomes Nanoformulation for Deep Tissue Bioimaging**

3.1 Introduction

NIR fluorescence imaging has attracted tremendous attention in biomedical science as it greatly improves imaging performance due to negligible tissue autofluorescence, reduced light scattering and absorption.[151,152] Among various NIR-active fluorophores, ICG is one of the US FDA and European Medicines Agency (EMA) approved chromophores widely used for clinical applications.[153] However, ICG has not achieved its fullest diagnostic and imaging potential due to certain limiting factors such as aqueous instability, rapid optical and thermal degradation, and concentration-dependent aggregation leading to quenching of its fluorescence emission.[154] Further, non-specific binding of ICG to blood plasma proteins leads to a relatively short circulation half-life.[155] To overcome these limitations, one of the promising approaches is to encapsulate ICG within a nanocarrier. With the advancement of nanotechnology, various types of nanoparticles (NPs) such as metals, liposomes, polymers, and proteins are developed to encapsulate ICG for biomedical applications.[156–161]

Among various types of NPs, vesicular systems have become an important platform for pharmaceutical applications.[162] These vesicular bilayers are made of

* This chapter is largely taken from the paper: **S. Bishnoi et al.**, "Optical Property Enhancing Novel Near-infrared Active Niosomes Nanoformulation for Deep Tissue Bioimaging", *ACS Omega* 2021, 6, 35, 22616–22624

amphiphilic molecules, which are capable of trapping hydrophilic and hydrophobic theranostic agents.[163,164] Vesicular systems such as liposomes have short stability and have a high cost of production.[165] Therefore, finding an alternative vesicular system with similar properties as liposomes is highly desirable.[166] Niosomes, synthesized from non-ionic surfactants, are affordable vesicular system with amphiphilic characteristics, neutral charge, and self-assembly properties.[167]

Niosomes are colloidal nanocarriers made from non-ionic surfactants and cholesterol. The non-ionic surfactants have a hydrophilic head group connected to a hydrophobic tail and possess a neutral charge.[168,169] Further, niosomes have an aqueous cavity similar to liposomes, but the neutral charge on non-ionic surfactants makes them less toxic than liposomes.[170] Additionally, cholesterol acts as a helper lipid that hinders the interaction of niosomes with proteins of the immune system and enhances their stability within the body fluids.[171] Moreover, the physical characteristics and preparation method of unilamellar or multilamellar structures of niosomes are similar to the liposomes.[172,173] However, compared to liposomes, niosomes have unique properties such as longer storage stability, use of relatively inexpensive raw materials, and spontaneous loading ability with both hydrophilic and hydrophobic molecules. Interestingly, the cosmetic industries were first to utilize niosomes as an alternative to phospholipid-based vesicles due to their low-cost production, enhanced stability, and easy storage.[174,175] Later on, the niosomes were also being assessed to deliver the theranostic agents like genes, siRNA, and vaccines.[176–180]

In this study, we developed an NIR active theranostic nanocarrier ICGNiosomes (ICGNios) by encapsulating ICG within niosomes composed of non-ionic surfactants (Tween 80 and Span 80) and cholesterol. These ICGNios were synthesized by an efficient and scalable preparation procedure using a thin-film hydration technique with an ICG encapsulation efficiency of ~62.5%. Spectral measurements of ICGNios showed a peak shift towards longer wavelengths with enhancement in fluorescence emission. The ICGNios also showed enhanced optical stability as compared to free ICG. Further these are biocompatible and thus could be used as a nanocarrier for biomedical applications. The *in vitro* NIR imaging depicted enhanced uptake of

ICGNios with improved fluorescence intensity compared to free ICG. Further, the *ex-vivo* imaging in ~1 cm thick chicken breast tissue resulted clear visualization of microcellular structure compared to free ICG. Therefore, the fabricated novel ICGNios present a biocompatible, biodegradable, versatile, and cost-effective contrast agent for deep tissue NIR imaging and has immediate translational biomedical applications.

3.2 Results and discussions

Fig. 3.1 shows the schematic representation of niosomes and ICGNios fabrication process. Niosomes were prepared using the thin-film hydration technique. For this, Tween 80, Span 80, and cholesterol were mixed at a molar ratio of 0.4:0.4:0.2 and dissolved in chloroform. To obtain the thin film, the chloroform was dried using a rotary evaporator at 37 °C under an ultra-high vacuum. This was followed by hydration of the thin film by 5 ml of DI water for fabrication of empty niosomes, and for ICGNios, ICG was dissolved in DI water. After hydration, spherical shape niosomes and ICGNios were obtained, which were used for further studies.

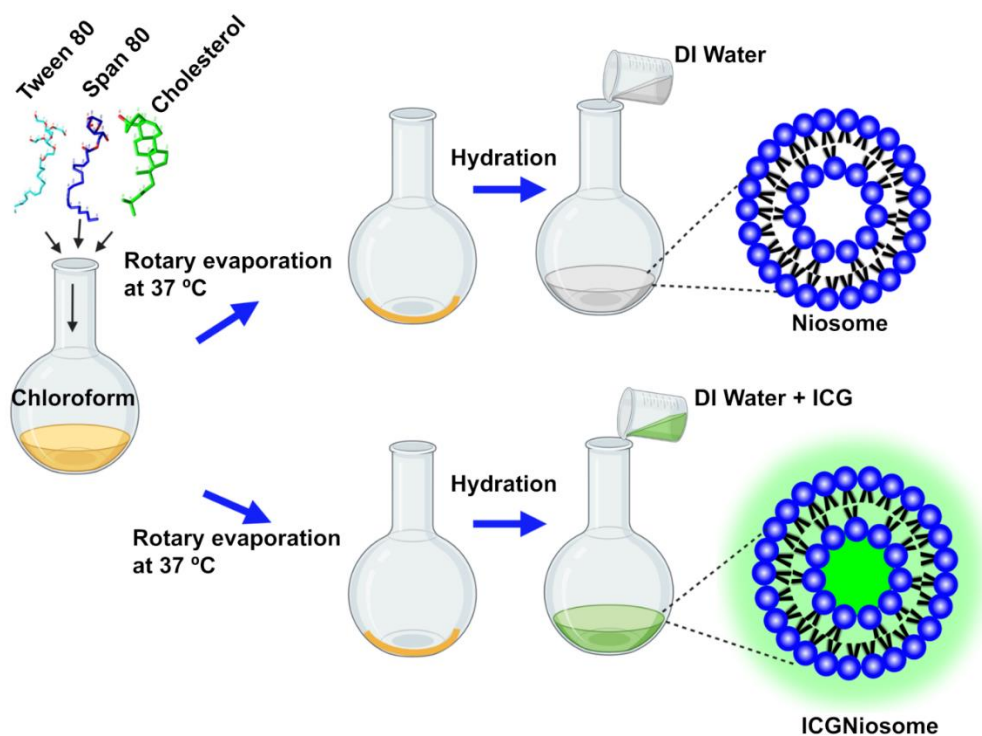


Figure 3.1 Schematic representation of the preparation of niosomes and ICGNios by thin-film hydration method. Tween 80, Span 80, and cholesterol are dissolved in chloroform followed by the formation of thin-film by evaporating chloroform using rotary evaporation at 37 °C. Niosomes and ICGNios are fabricated by hydration of the thin-film of non-ionic surfactants using DI water and ICG dissolved in DI water.

3.2.1 Morphological characterization of Niosomes and ICGNios

The morphology and size of empty niosomes and ICGNios were characterized by FESEM and TEM. SEM image (**Figure 3.2a**) shows that the niosomes appear spherical and ~250 nm in size. However, both the SEM and TEM images (**Figure 3.2b and 3.2c**) show that ICG encapsulation within the niosomes NPs, make them more compact, and result in marginal reduction in size of ~200 nm, whereas the shape remained spherical. This could be attributed by the strong binding of the lipophilic moieties of ICG with the lipophilic part of the niosomes, which might result in a reduction in the size of the ICGNios after encapsulating ICG.[176] The hydrodynamic diameter (Dh) distribution of niosomes and ICGNios was studied by the DLS measurements. The estimated average diameter of niosomes was ~262 nm with the

polydispersity index (PDI) of 0.29. However, after loading with ICG, the average diameter of ICGNios gets reduced to 210 nm with a PDI of 0.27 (**Fig. 3.2d and 3.2e**). These results suggest that electrostatic interaction between niosomes and ICG plays a significant role in reducing the size and PDI of ICGNios compared to niosomes, which is crucial for their use in biomedical applications.

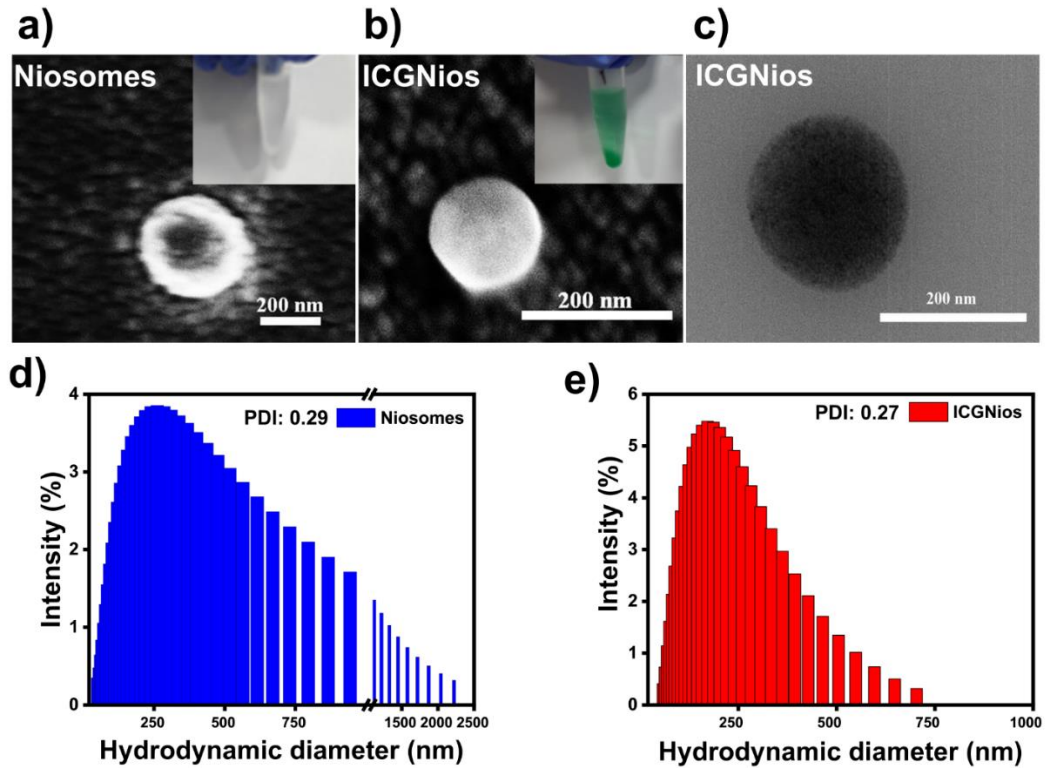


Figure 3.2 Morphological characterizations of niosomes and ICG Niosomes (ICGNios). (a) Scanning electron microscopy (SEM) image of niosomes, (b) SEM image of ICGNios (c) Transmission electron microscopy (TEM) image of ICGNios. Scale bar 200 nm. (d-e) Dynamic light scattering (DLS) measurement of niosomes and ICGNios depicting hydrodynamic diameter (D_h) and polydispersity index (PDI) of niosomes and ICGNios.

3.2.2 Encapsulation efficiency (EE) of ICGNios

The EE of the niosomes signifies the efficacy of vesicles to load therapeutic agents. Therefore, the EE of ICG within ICGNios was estimated using equation (i).

For optimizing the EE of ICG, the ICGNios were prepared with different ICG concentrations; 50, 100, and 200 μM . For quantification of loaded ICG, the ICGNios NPs were solubilized and disintegrated using DMSO, and the light absorption at 794 nm was measured. The EE of ICGNios formulation using different concentrations of ICG is shown in **Table 3.1**. The loading efficiency of the niosomes seems to increase with the increasing concentration of ICG. Also, the highest EE ($\sim 62.5\%$) was obtained when niosomes were fabricated using 200 μM of ICG and are used for further studies.

S. No.	Concentration of ICG used for ICGNios formulation	ICG EE%
1.	50 μM	47.5
2.	100 μM	50
3.	200 μM	62.5

Table 3.1 ICG encapsulation efficiency (EE) using the different concentrations of ICG for ICGNios fabrication.

3.2.3 Biochemical characterization of free ICG and ICGNios

The absorption and fluorescence emission properties of free ICG, niosomes and ICGNios were studied to validate ICG encapsulation within the NPs. The absorption spectra revealed that the absorbance of ICGNios got enhanced and showed a ~ 20 nm bathochromic shift from 778 nm to 798 nm compared to free ICG (**Figure 3.3a**). This remarkable redshift (~ 20 nm) in the absorption spectrum of ICGNios suggests active interaction of ICG with the niosomes. Essentially, the absorption peak shift of ICGNios to the longer wavelength (~ 798 nm) allows optical imaging in the NIR window. On the other hand, empty niosomes did not show any absorption peak in this wavelength range. Further, to validate peak shifting, Gaussian peak fitting was performed in the major absorption spectra of free ICG and ICGNios. The peak position of the monomeric form of ICG was found at 782 nm and 801 nm for free ICG and ICGNios, respectively. However, the peak width of ICGNios (~ 42.3 nm) did not show

significant change compared to the free ICG (~39 nm). The fitted absorption spectra revealed that redshift occurs in the ICGNios sample for both the monomeric and dimeric shoulder peak of nanoencapsulated ICG compared to the free form of ICG (**Figure 3.3b and 3.3c**). The redshift in the absorbance of ICGNios compared to free ICG might be due to the formation of ICG J aggregates (IJA) by the interaction of amphiphilic ICG with the niosomal membrane as reported previously with different ICG loaded nanoparticles.[59,66,181] Thus, the absorption peaks of ICGNios indicate that most of the ICG is encapsulated within niosomes in the form of IJA, which is an optically stable form.[182] Once encapsulated, IJA remains stable in a J-aggregated state in different solvents and shows excellent optical properties, which is crucial for NIR imaging for diagnosis and treatment.[183] Following the absorption assessments, the fluorescence emission measurements of free ICG, niosomes, and ICGNios were carried out. The free ICG shows maximum fluorescence emission (λ_{max}) at 810 nm, while the λ_{max} of ICGNios is shifted to 830 nm (**Fig. 3.3d**). In addition to the fluorescence peak shift, the ~1.5-fold fluorescence enhancement is also observed in the case of ICGNios, as shown in **Fig. 3.3d**. Here, all fluorescence spectra were smoothed using a Savitzky–Golay filter. This fluorescence enhancement might be due to the interaction between ICG molecules and surfactants, which reduces the random vibration and/or rotation of ICG molecules.[184,185]

In accordance with the enhancement of fluorescence emission of ICGNios as compared to free ICG, the quantum yield Φ_s of ICGNios was determined using equation (ii). The Φ_s of ICGNios was estimated relative to free ICG ($\Phi_{\text{sref}} = 0.016$) in water.[186] The measured Φ_s of ICGNios is 0.0202, which suggests that with the enhancement in the fluorescence intensity, the ICGNios also improved the quantum yield of ICG. Also, the enhanced quantum yield suggests the higher-order arrangement of ICG molecules within the ICGNios, forming a stable structure by preventing the free molecular vibrations and motions.[187] Thus, an overall analysis of the optical characteristics (absorption and emission) of samples confirms the encapsulation of ICG within ICGNios. The higher quantum yield and redshift at longer wavelength of ICGNios is advantageous and could be used to improve the imaging capabilities for deep tissue NIR bioimaging for disease diagnosis.

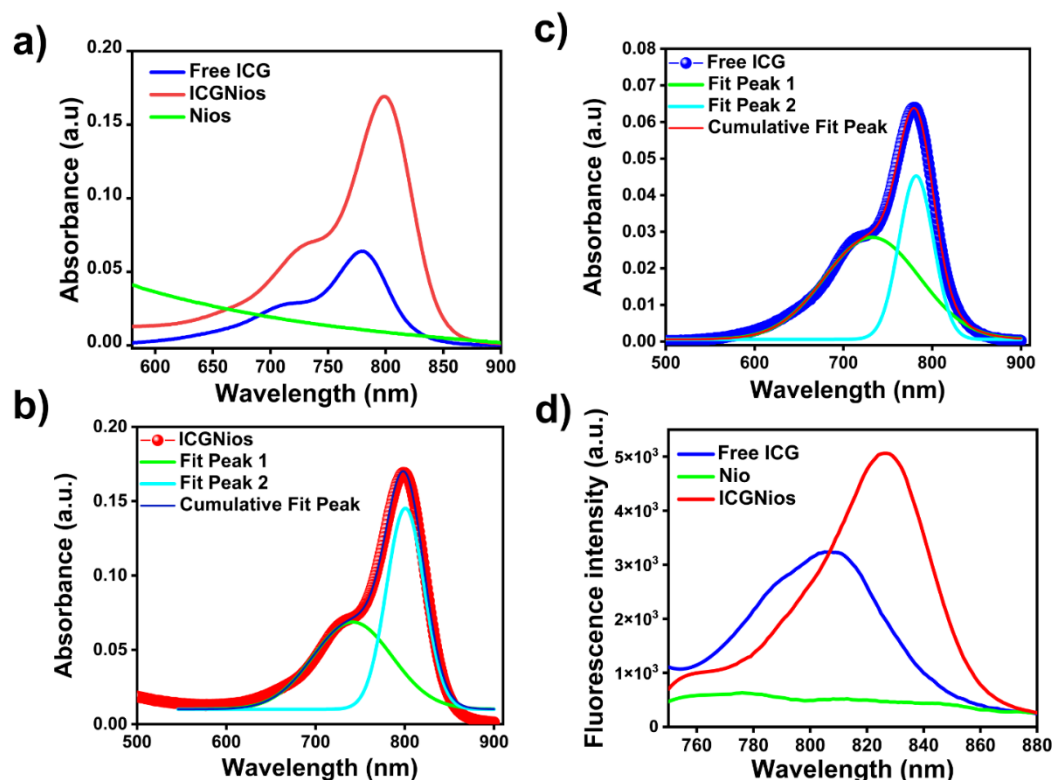


Figure 3.3 Biochemical characterizations of free ICG, niosomes, and ICGNiosomes (ICGNios). (a) Absorption spectra of free ICG, niosomes, and ICGNios. (b) The fitted absorption spectrum of ICGNios with $R^2=99.86\%$. (c) The fitted absorption spectrum of free ICG with $R^2=99.43\%$. (d) Fluorescence emission spectra of free ICG, niosomes, and ICGNios. All fluorescence spectra were smoothed.

3.2.4 Excitation Emission Matrix (EEM) of ICGNios

Further to visualize the fluorescence emission properties of free ICG, ICGNios and niosomes more clearly, the excitation-emission matrix (EEM) was recorded. The EEM results show that ICGNios exhibit a redshift in the λ_{maxem} at 825 nm compared to free ICG, for which the λ_{maxem} is 810 nm (**Fig. 3.4a and 3.4b**). This redshift at a longer wavelength is crucial for deep tissue penetration, background reduction, and increase in SNR of NIR imaging to visualize a detailed image of inaccessible structures. Meanwhile, for niosomes, the EEM did not show any fluorescence signal, providing further evidence that the interaction between ICG and niosomes plays a vital role in the bathochromic peak shift of ICGNios (**Fig. 3.4c**). Importantly, a ~ 2 -fold

enhancement of fluorescence emission was also seen in ICGNios compared to the free ICG. This result demonstrated the importance of using ICGNios formulations with longer emission wavelengths for deep tissue NIR imaging.

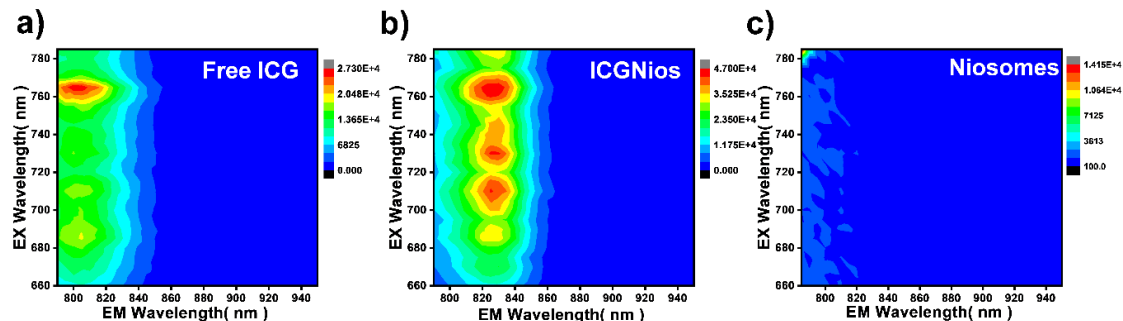


Figure 3.4 Excitation-emission matrix (EEM) of (a) Free ICG ($3 \mu\text{M}$), (b) ICGNios constituting $3 \mu\text{M}$ ICG and (c) Niosomes.

3.2.5 Interaction of ICG with the individual components of niosomes

To determine which constituent of niosomes is responsible for enhancing the optical property (absorbance and fluorescence emission) of ICG, the individual components of niosomes are mixed with an equivalent concentration of ICG ($12 \mu\text{M}$), illustrated in **Fig. 3.5a**. Then the interaction between ICG and different components of niosomes is studied by analyzing their absorption and fluorescence emissions spectra. The spectroscopic result suggests that the absorbance and fluorescence emission of ICG get enhanced in combination with tween 80; however, there is minimal change in the optical property of ICG in the presence of span 80 (**Fig. 3.5b and 3.5c**). Additionally, the tween 80 and span 80 also induce a bathochromic shift in the peaks of the absorbance (798 nm) and fluorescence emission (830 nm) of ICG towards a longer wavelength compared with free ICG. Results indicate that tween 80 contributes significantly to improve the optical properties of ICG.

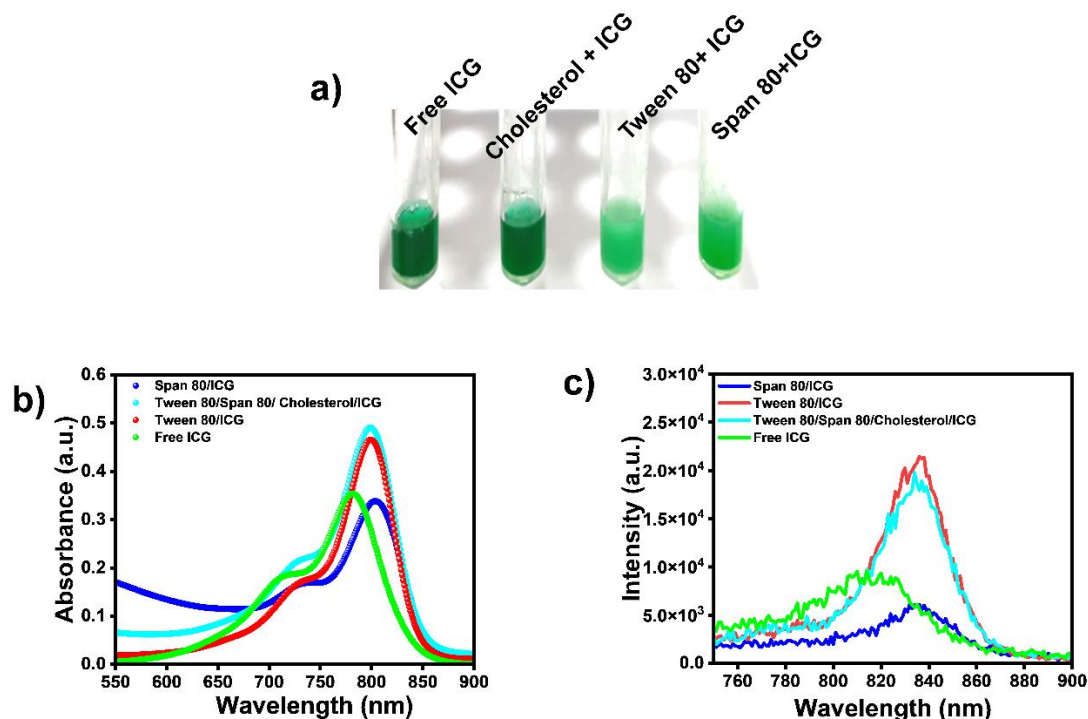


Figure 3.5 Spectroscopic characterization of individual components of niosomes (Span 80, tween 80 and cholesterol) with ICG. (a) Digital photographs of free ICG, cholesterol/ICG, tween 80/ICG and span 80/ICG blends. (b) Absorption spectra of free ICG, tween 80/ICG and span 80/ICG. (c) Fluorescence emission spectra of free ICG, tween 80/ICG and span 80/ICG.

3.2.6 Spectral characteristics of ICGNios encapsulating high concentration of ICG

ICG tends to aggregate in water at higher concentrations, leading to quenching of its fluorescence emission. In addition, at higher concentrations, the absorption and emission spectra of ICG overlap, resulting in a photosensitizing effect that limits its use in clinical settings. Therefore, the optical characteristics of ICGNios loaded with a high concentration of ICG were investigated by studying their absorbance and fluorescence emission properties compared to free ICG. Results of ICGNios encapsulated with 80 μ M, and 100 μ M showed that the absorption efficiency of ICGNios increased with increasing ICG concentration (**Fig. 3.6a**). However, the free form of ICG tends to form H aggregation at higher concentrations, which reduces its absorption. Hence, the encapsulation of ICG within these niosomes can minimize this

effect. Likewise, in comparison to free ICG, the ICGNios also showed anti-quenching of fluorescence emission of ICG at higher concentrations (Figure 6b). The result suggests that ICGNios encapsulated with higher ICG concentrations could be used for NIR imaging in clinical practices.

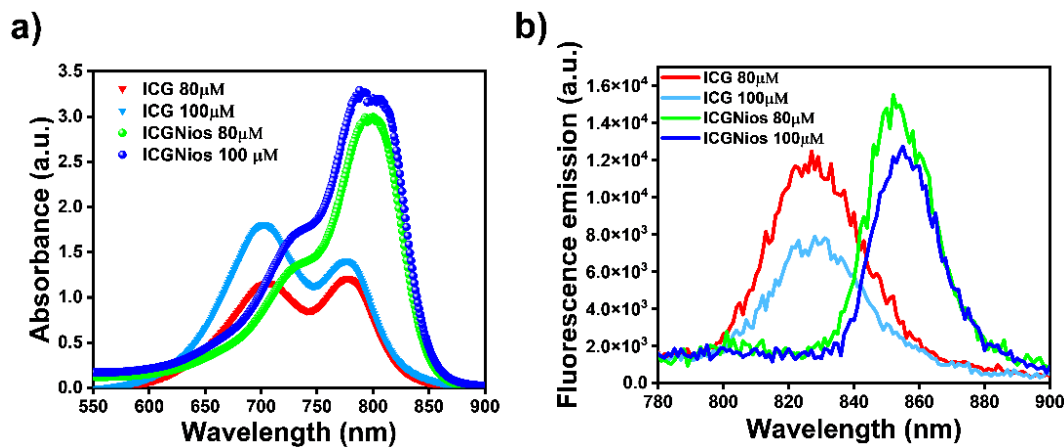


Figure 3.6 Antiquenching spectral characteristics of ICGNios compared to free ICG. (a) Absorption spectra and (b) fluorescence emission of free ICG and ICGNios constituting equivalent concentrations (80 μM and 100 μM) of ICG.

3.2.7 Optical and storage stabilities of ICGNios

Free ICG is an optically unstable NIR chromophore as it gets degraded when exposed to light. Hence, for better bioimaging applications, ICG's photostability should be preserved by encapsulating the ICG within the nanocarriers. Here we encapsulated ICG within niosomes, and the photostability of the free ICG was compared with ICGNios by placing both the samples in ambient light at room temperature for 48 h. The absorbance of the samples was recorded at different time intervals to check the photostability. The result indicates that free ICG degraded about ~90 % while ICGNios degraded only 25% over the 48 h time, as shown in **Fig. 3.7a**. This suggests that ICG encapsulated within niosomes is more optically stable compared to free ICG. In addition to this, free ICG also gets degraded over a period, even at low temperatures such as 4 °C. However, the rate of degradation would proportionately increase with the rise in the temperature.[66,188] The storage stability

of ICG could also be increased by encapsulating it within nanocarriers. The storage stability of free ICG and ICGNios were studied after four weeks of storage at 4 °C in dark. Interestingly, we found that ICGNios showed ~40 % degradation after 30 days of storage at 4 °C in the dark condition, while free ICG showed ~80 % degradation in the same conditions (**Fig. 3.7b**). Thus, this long-term stability of ICGNios could be advantageous for wider use in biomedical applications.

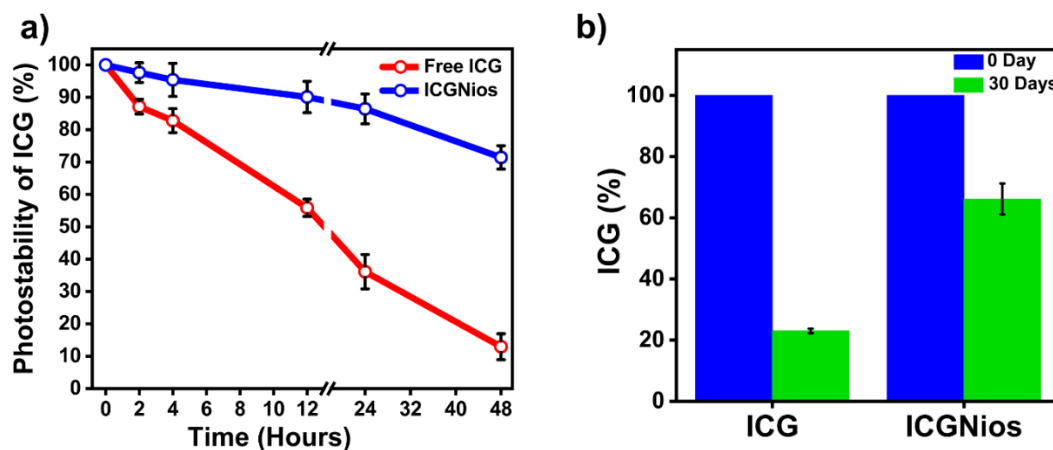


Figure 3.7 Photostability and storage stability of the ICGNios vs. free ICG. *a)* Photostability (%) of ICGNios and free ICG under exposure of ambient light at room temperature. *b)* Storage stability (%) of ICGNios and free ICG incubated at 4 °C in the dark condition.

3.2.8 Biosafety of ICGNios

The NPs used for different biomedical applications should be non-toxic and biodegradable. Therefore, the biosafety of ICGNios and niosomes was evaluated using MTT assay. For this, different concentrations of niosomes and ICGNios (0.5 μ M, 2 μ M, 10 μ M, 20 μ M, 25 μ M, 50 μ M, and 100 μ M) were used. **Fig. 3.8a** shows that more than 80 % of cells were viable even when the cells were treated with the maximum concentration (100 μ M) of ICGNios and niosomes. The HeLa cells without any treatment were used as a control, while the cells incubated with solubilizing buffer were used as a positive control which showed less than 5 % cell viability. This result

suggests that niosomes and ICGNios are safer nanocarrier for NIR bioimaging and other biomedical applications.

3.2.9 *In vitro* NIR bioimaging using ICGNios

A comparative NIR optical imaging study was performed between ICGNios and free ICG. For this, the HeLa cells were incubated with freshly prepared ICGNios and free ICG for 4 h. Cells incubated with media were used as a control. After four hours, the fluorescence images of control, ICG, and ICGNios treated HeLa cells were recorded. The nuclei of cells were counter-stained with DAPI to understand the intracellular distribution of ICG (**Figure 3.8b**). The NIR fluorescence imaging showed that ICGNios are readily internalized within the cells to release ICG in the cytoplasm and emit higher fluorescence as compared to the free ICG treated cells. Control cells did not show any NIR emission. Thus, the ICGNios proved to be a better nanocarrier for delivery of contrast agents suited for NIR imaging. Further, for quantification of fluorescence intensity, the mean fluorescence intensity (MFI) of fluorescence emitting cells was quantified. The MFI measurement supports the cellular uptake results (**Fig. 3.8b**), where control cells showed negligible fluorescence intensity and ICGNios treated cells showed ~1.5-fold higher NIR fluorescence emission than free ICG treated cells (**Fig. 3.8c**). These results suggest that the enhanced cellular uptake of ICG is due to the efficient binding of ICGNios to the cells, followed by the internalization and release of ICG in the cytoplasm. These findings indicate that ICGNios could be used as an exogenous contrast agent for NIR fluorescence bioimaging.

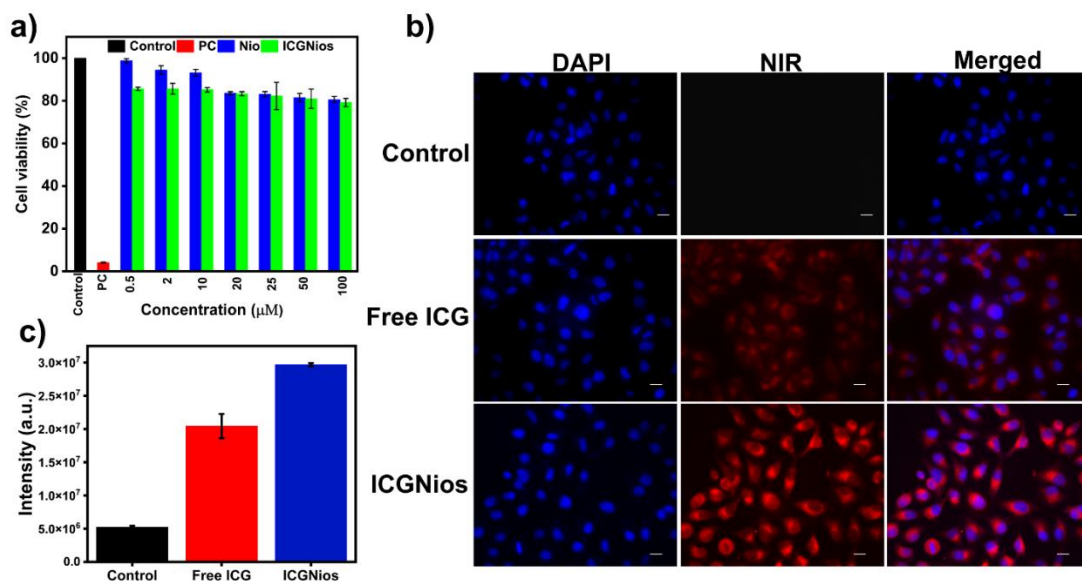


Figure 3.8 *Biocompatibility and NIR imaging of niosomes, ICGNios, and free ICG in HeLa cells (a) MTT assay of niosomes and ICGNios; where PC is positive control (b) Fluorescence imaging of HeLa cells; The DAPI staining nuclei are shown in blue colour, and ICG fluorescence emission is displayed in red colour. Scale bar: 20 μm and (c) Mean fluorescence emission intensity plot of control, free ICG and ICGNios.*

3.2.10 *Ex vivo* deep tissue NIR imaging

The fluorescence emission spectra of ICGNios showed an enhancement and a redshift compared to free ICG (**Fig. 3.3d**). This property could be helpful in deep tissue NIR bioimaging. For this purpose, the *ex vivo* NIR bioimaging was done with chicken breast tissue of ~1 cm thickness. The capillary tubes (CTs) of 75 mm in length and 1 mm inner diameter were filled with free ICG (10 μM), ICGNios, and water, respectively. These CTs were then placed above the tissue sample for deep tissue NIR imaging (**Fig. 3.9a**). *Ex vivo* fluorescence images were recorded in reflectance geometry. **Fig. 3.9** shows the bright field (BF) and NIR fluorescence images of CTs (filled with water, ICG, and ICGNios) and chicken breast tissue samples (placed with different CTs). The ICGNios tissue showed comparatively higher fluorescence emission over ICG filled CT (**Fig. 3.9b**). Similarly, CT filled with ICGNios showed significantly higher fluorescence intensity as compared to free ICG (**Fig. 3.9b**). As expected, the water-filled CT did not show any NIR fluorescence emission (**Fig. 3.9b**).

Further, the MFI of the tissue section with ICGNios filled CT showed ~ 7 -fold higher fluorescence intensity as compared to the tissue section filled with with free ICG (**Fig. 3.9c**). These results suggest that ICGNios have higher tissue penetration and can be detected across a ~ 1 cm thick chicken breast tissue sample. Thus, this novel nanoformulation could offer a promising platform for deep tissue NIR imaging to visualize inaccessible cellular microstructures for biomedical applications.

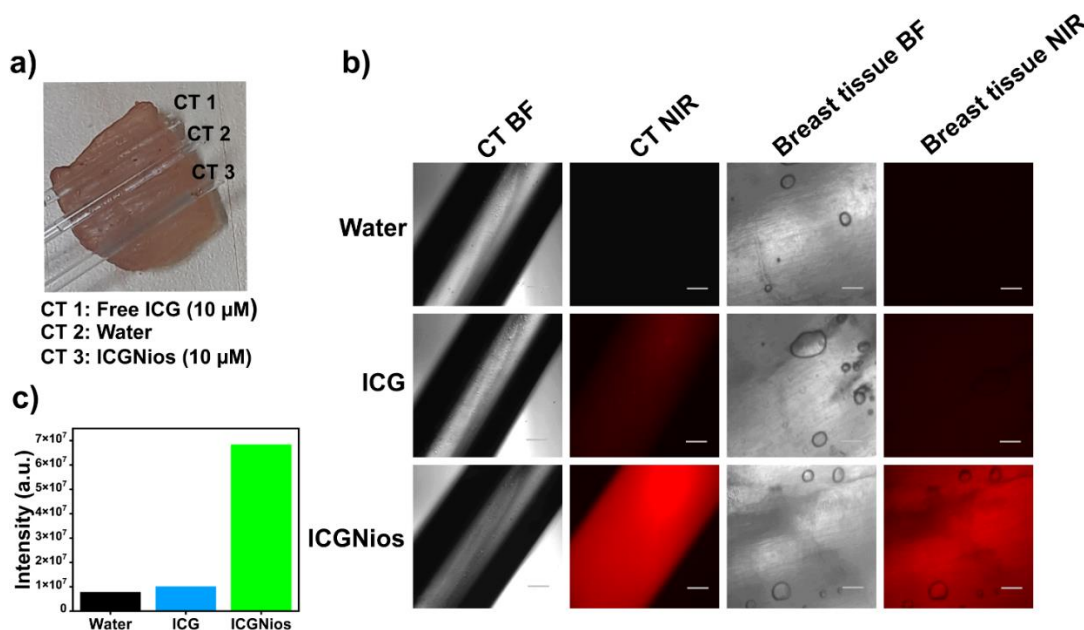


Figure 3.9 *Ex vivo* deep tissue enhanced NIR imaging of chicken breast tissue of ICGNios vs. free ICG. (a) Picture of capillary tubes filled with water, free ICG, and ICGNios placed over chicken tissue sample with the thickness of ~ 1 cm (b) Bright field and NIR bio bioimaging of CT filled with water, free ICG and ICGNios (column 1 and 2) and chicken breast tissue with CT filled with water, free ICG and ICGNios (column 3 and 4). Scale bar 100 μ m. (c) Mean fluorescence intensity plot of chicken breast tissue placed beneath the CT filled with water, free ICG and ICGNios.

3.3 Summary

In this study, novel NIR active niosomes (ICGNios) were fabricated using non-ionic surfactants (Tween 80, Span 80) and cholesterol for NIR bioimaging. The ICGNios exhibited enhanced absorbance and fluorescence emission compared to free

ICG. Additionally, the ICGNios displayed excellent photostability upon 48 h of light exposure. Moreover, the ICGNios showed only ~40% degradation after 30 days of storage at 4 °C compared to the free ICG, which showed ~80% degradation. Thus, ICGNios provides a simple approach to enhance the fluorescence quantum yield and optical stability of ICG by protecting it from photodegradation and improving the long-term storage stability. Most importantly, the ICGNios are biocompatible and are safe for biomedical applications. Additionally, the NIR fluorescence of ICGNios could be detected through ~1 cm thick chicken breast tissue, which was not possible using a free form of ICG. Thus, the novel ICGNios with improved optical and storage stability of ICG is a promising cost-effective platform for deep tissue NIR fluorescence bioimaging.

Chapter 4

*Fusogenic Viral Protein-Based Near-Infrared Active Nanocarriers for Biomedical Imaging**

4.1 Introduction

Fluorescence-based molecular imaging is an active area of interest for non-invasive clinical diagnosis and therapy.[189] A broad range of synthetic NPs such as metallic, polymers, micelles, and liposomes are being used to deliver various contrast agents to the host cells.[190–194] However, the majority of the NPs poses long- and short-term toxicity concerns; hence, are not suitable for *in vivo* biomedical applications.[195–197] Therefore, nowadays, researchers are moving towards naturally-derived biodegradable nanoconstructs for drug delivery.[198,199] Moreover, there is an increasing interest in the use of viruses as drug delivery systems (DDS) due to their intrinsic property of attachment to the host cells and swift delivery of their genetic materials.[200–203] Additionally, viruses can escape the endolysosomal compartment, where most of the NPs get trapped and degraded by an acidic environment.[204,205] Inspired by the viruses, scientists have developed virus-like nanoparticles (VNPs) that lack genetic material and are made up of solely viral structural protein for encapsulating theranostic agent. Thereby, these VNPs are non-infectious and act only as nanocarriers as they are replication-incompetent.[206] VNPs have been studied previously to encapsulate inorganic nanomaterials like

* This chapter is largely taken from the paper: **S. Bishnoi et al.**, "Fusogenic Viral Protein-Based Near-Infrared Active Nanocarriers for Biomedical Imaging", *ACS Biomaterials Science & Engineering*, 2021, 7, 7, 3351–3360

quantum dots (QDs), gold, and magnetic NPs for bioimaging.[207,208] In addition, VNPs with fusogenic envelope protein is of great interest as they enter target cells by receptor-mediated endocytosis and fuse with the endosomal membrane by low pH-induced conformation change to release cargo within their cytoplasm.[209,210] In this context, the fusogenic envelope protein-based VNPs has been reported earlier to deliver iron oxide NPs and radionuclides for *in vivo* high-resolution PET and MRI imaging. [211–213]

Here we have exploited the fusogenic properties of vesicular stomatitis virus (VSV) envelope glycoprotein (VSV-G) to bioengineer VNPs to deliver contrast agents for bioimaging. The VSV is a negative-strand RNA virus with a single fusogenic envelope protein which is also a cell attachment protein.[214,215] This fusogenic protein has broad tissue tropism which facilitates easy entry into the cell for the delivery of the cargo.[216] Additionally, the VSV-G shows pH-dependent conformation change that allows the fusion of viral envelope protein with the endosomal membrane of host cells to release the genetic material.[217,218] Moreover, when expressed in human cells, VSV-G gets self-assembled and released from the cells at a very high titre in the form of lipid-bound fusogenic nano-vesicles.[219] Therefore, VSV-G protein-based carriers have been extensively used to deliver other viral genes.[220] These nano-vesicles have also been used for packaging and delivering mammalian genes, mRNA, proteins, and organelle to a wide range of mammalian cells and tissues.[216,219,221–223] Additionally, the simplicity of the production, purification, and customization makes the VSV-G-based nanocarrier an attractive tool for biomedical applications.[224] Despite being successfully employed as a nanocarrier, the VSV-G-based VNPs have never been explored to deliver contrast agents for optical imaging. Here, for the first time, we present the VSV-G -based VNPs to encapsulate NIR ICG dye for optical bioimaging.

NIR fluorescence has the potential for non-invasive deep tissue imaging, particularly for early-stage cancer diagnosis.[55,225,226] NIR imaging is capable of higher tissue penetration and better visualization of cellular microstructure due to reduced photon scattering and negligible tissue auto-fluorescence in the optical window (650 to 950 nm).[227–229] Additionally, the use of NIR-active exogenous

contrast agents could further improve the SNR of fluorescence imaging.[230,231] ICG is one of the NIR active cyanine dye used for the past six decades for bioimaging.[185,232,233] However, due to various limitations of the ICG, the broader application of ICG as a potential contrast agent for bioimaging is not achieved yet.[83] These limitations of ICG could be addressed by encapsulating it within various types of nanoformulation that can be used for biomedical applications. [234–237]

The present study aims to exploit the unique property of fusogenic VSV-G VNPs as an efficient contrast agent delivery system. Here, we report successful fabrication of VSV-G-based NIR-active viral nano constructs (NAVNs) encapsulating ICG suitable for NIR bioimaging. The morphological characterization of bioengineered VNPs showed nanosized, spherical particles suited for easy uptake by cells. Further, VSV-G-based VNPs are safe to use as a drug delivery vehicle for *in vitro* and *in vivo* applications as they do not show any cytotoxicity.

4.2 Results and discussions

Fig. 4.1 shows the schematic presentation of the production of VNPs and fabrication of NAVNs. First, the VSV-G gene was PCR amplified from the pVSVFL (+) vector,[238] having a full-length genome of the VSV virus by using VSV-G gene-specific primers as mentioned in **Table 2.1**. Further, the amplified VSV-G gene was cloned into pCAGGS mammalian expression vector using recombinant DNA technology (**Fig. 4.1a**). The plasmid DNA was then amplified in the *Escherichia coli* (*E. coli*-DH5 α) bacteria host (**Fig. 4.1b**). Subsequently, the plasmid was transiently transfected in HEK293T cells used as a biofactory for the expression and production of VNPs (**Fig. 4.1c**). The VNPs harvested from conditioned media of VSV-G transfected cells were pelleted down and purified further by 20% sucrose cushion ultracentrifugation (**Fig. 4.1d**). The result shows an overwhelmingly higher amount of purified VSV-G protein (67 kDa) with a trace amount of membrane proteins as VNPs acquire envelope from the mammalian host cells. Further, Western blot analysis with anti-VSV-G antibody confirmed the expression of the 67 kDa VSV-G protein in both pCAG-VSVG transfected cell lysate (lanes 2 and 3) and conditioned media purified from VSV-G transfected cells (lane 4) (**Fig. 4.1e**). This suggests that the conditioned

media have sedimentable VSV-G-based VNPs, which could be further used to fabricate NAVNs. For the fabrication of NAVNs, ICG is encapsulated within purified VNPs by the incubation method (**Fig. 4.1f**). ICG is a negatively charged tricyanin dye with a molecular weight of 775 Da and possesses an amphiphilic property due to the presence of both hydrophilic (sulfonate group) and lipophilic (polycyclic ring) moieties linked with a polyene bridge (inset; **Fig. 4.1f**).[239] The amphiphilic property of ICG allows it to bind with the proteins and phospholipids, the major components of the cellular membrane. Moreover, the lipophilic part of ICG enables it to get encapsulated within the internal core of lipid vesicles primarily by diffusion across the phospholipid membrane.[185,240] Likewise, the interaction of the lipophilic ICG with the lipid-bound envelope of VNPs facilitates the diffusion and encapsulation of ICG within the envelope and internal core of these viral particles. A similar mechanism of encapsulating ICG within the lipid-membrane-bound extracellular vesicles has been reported earlier.[241–243]

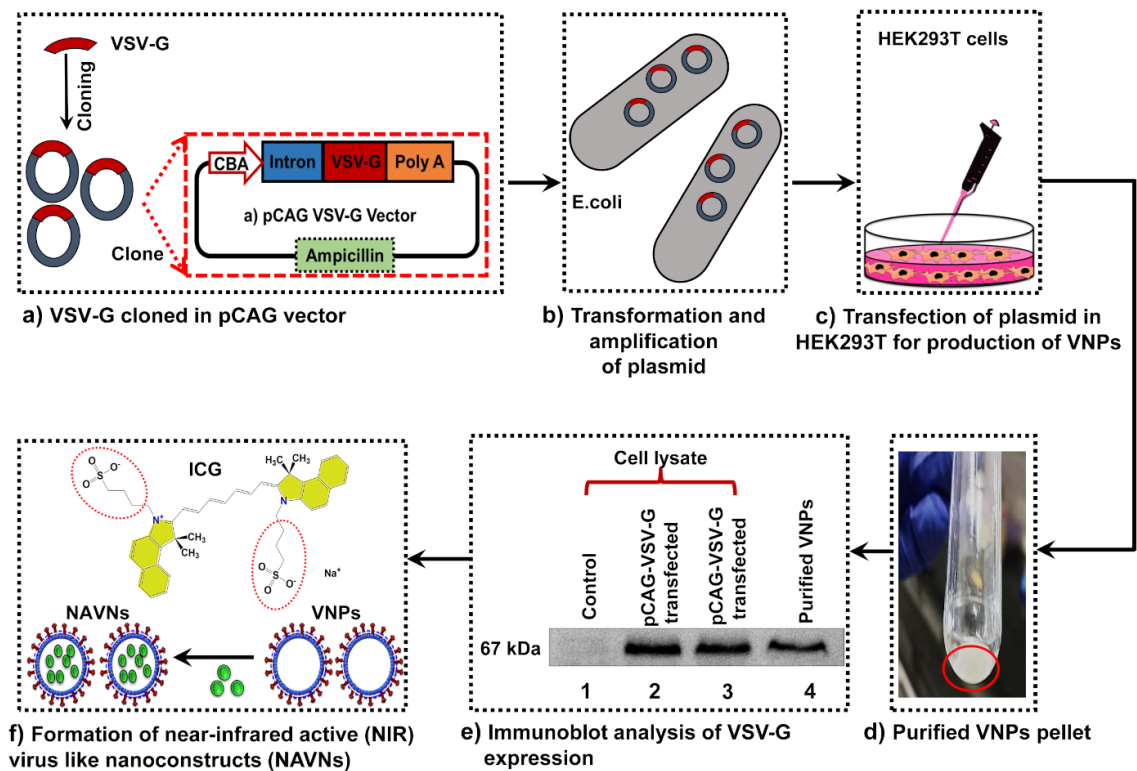


Figure 4.1 Schematic of bioengineering of VNPs and fabrication of NAVNs. (a) VSV-G gene cloned in pCAG mammalian expression vector. (b) Transformation and amplification of plasmid in *DH5a*. (c) Transfection of pCAG-VSVG in HEK293T cells. (d) VNP pellet after final purification by ultracentrifugation. (e) Western blot analysis for detection of VSV-G protein using an anti-VSVG polyclonal antibody. (f) Fabrication of NAVNs by incubation of VNPs with ICG; inset: chemical structure of ICG where the sulfonate group is circled in dotted red color and the polycyclic ring is highlighted by yellow color.

4.2.1 Morphological characterization of VNPs and NAVNs

The morphology of VNPs and ICG-loaded NAVNs was characterized by TEM that shows that VNPs are spherical in shape with an average particle size of ~200 nm (**Fig. 4.2a**). The TEM image of NAVNs also indicates that these are of nearly similar size and morphology to VNPs (**Fig. 4.2d**). However, an enhancement in contrast of the NAVN membrane is observed, which suggests that ICG is successfully loaded

within the VNPs. The DLS measurement further confirmed that the Dh of VNPs and NAVNs is similar in an aqueous environment (**Fig. 4.2b and 4.2e**). The DLS measurement showed that the average sizes of VNPs and NAVNs are ~175 and ~180 nm with polydispersity indices (PDIs) of 0.258 and 0.236, respectively. These results suggest that the doping of ICG did not change their size significantly. The zeta potential of VNPs was found to be -26.6 mV (**Fig. 4.2c**). Interestingly, the loading of ICG within VNPs reduces the surface charge of NAVNs with a zeta potential value of -59.9 mV (**Fig. 4.2f**). This implies that the binding of negatively charged ICG with the envelope protein (VSV-G) and lipid membrane of VNPs would modify the surface charge density of VNPs. As a result, the NAVNs will have a low negative value of the zeta potential. This could be inferred as a substantial amount of ICG is incorporated within the envelope of VNPs and gets stabilized by electrostatic interaction. Hence, the reduction in zeta potential confirms the encapsulation of ICG within VSV-G-based VNPs and the successful fabrication of NAVNs. Additionally, due to the high zeta potential, NAVNs will not aggregate. These results confirm that VSV-G expression in human cells produced nanosized particles, which could be used to encapsulate the contrast agents like ICG for biomedical applications.

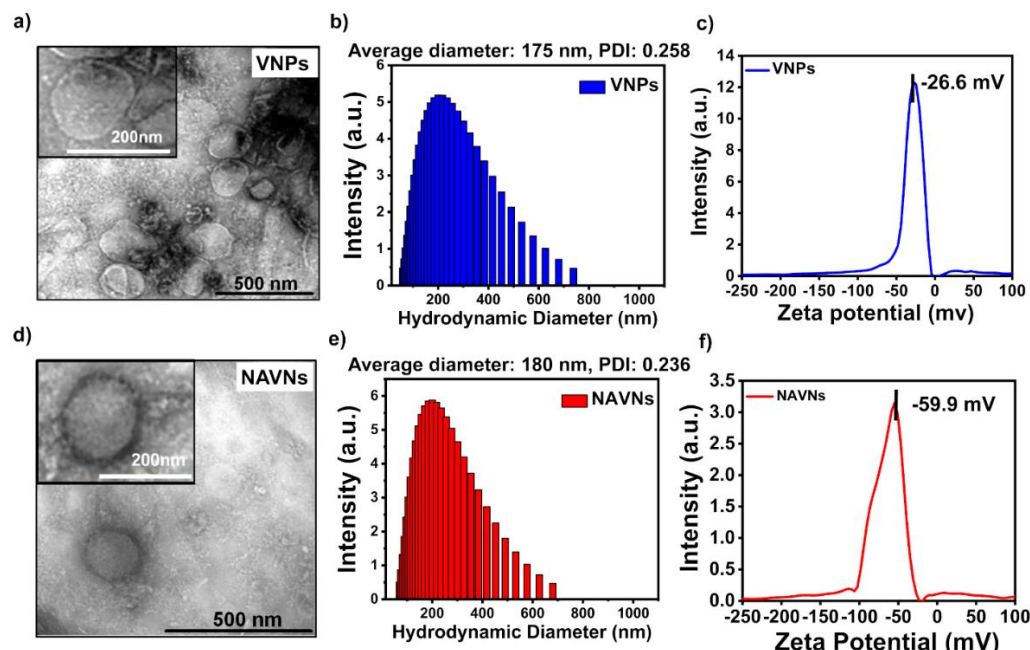


Figure 4.2 Morphological characterization of VNPs and NAVNs. (a and d) TEM image of VNPs and NAVNs. (b and e) Dynamic light scattering (DLS) of VNPs and NAVNs with an average diameter of 175 and 180 nm with a polydispersity of 0.258 and 0.236. (c and f) Zeta potential of VNPs and NAVNs.

4.2.2 Encapsulation efficiency

The EE of ICG within NAVNs was estimated using equation (v) which provides a molar concentration of ICG encapsulated within NAVNs. During fabrication, the NAVNs were pelleted down, and the ICG remaining in the supernatant was quantified by measuring the absorbance using a UV–vis microplate reader at 778 nm. Further, the concentration of untrapped ICG was calculated by comparing the calibration curve of free ICG dissolved in water. The EE of ICG within NAVNs was found to be ~75%.

4.2.3 Biochemical characterization

The optical properties of free ICG and NAVNs were characterized by absorption and fluorescence spectroscopic measurements. The absorption spectrum of free ICG (9 μM) diluted in water displays two characteristic peaks at ~780 and ~710 nm

representing its monomeric and dimeric forms, respectively (**Fig. 4.3a**). However, the absorption spectrum of NAVNs shows a broadened peak with decreased intensity at ~ 780 nm. The differences in peak intensity and spectral broadening in NAVNs might be due to the electrostatic interaction of ICG with the lipid-bound envelope and protein of VNPs, leading to the aggregation of ICG with various conformational states. The VNPs and water, as expected, showed negligible absorbance in that wavelength range (black and red curves in **Fig. 4.3a**). Moreover, the fluorescence spectrum of NAVNs upon excitation with 680 nm also showed a reduction in fluorescence emission compared to free ICG (9 μM) (**Fig. 4.3b**). The decrease in fluorescence intensity of NAVNs could be due to the aggregation-caused quenching (ACQ) of encapsulated ICG.[244] However, water and VNPs showed negligible fluorescence emission. Hence, a remarkable difference in the optical property of NAVNs is indicative of the different conformational states of ICG within the nanoscale VNPs. Consequently, the results confirm the successful fabrication of optically active NAVNs, which can be used as an exogenous contrast agent for bioimaging.

4.2.4 Photostability comparison between free ICG and NAVNs

Free ICG is an optically unstable chromophore, which gets degraded over time when exposed to light. ICG forms reactive singlet oxygen ($^1\text{O}_2$) responsible for oxidative c-c cleavage of its backbone leading to photodegradation.[245] In addition, ICG molecules randomly vibrate along the backbone. Stabilization of these vibrations are suggested to improve the optical properties of ICG, which is eventually achieved by encapsulating it within NPs. Therefore, to enhance the photostability of ICG, it was encapsulated within VNPs. Further, the kinetic study for fluorescence and photostability of NAVNs and free ICG was done after ambient light exposure of both samples over 72 hours (at the time points of 0, 2, 4, 12, 24, 48, and 72 h). The emission spectra were normalized by the initial fluorescence intensity of the samples. The result demonstrates that NAVNs-encapsulated ICG has higher optical stability as the fluorescence intensity of NAVNs degraded only $\sim 40\%$ after 72 hours of light exposure. While the free ICG showed more than 80% degradation during the same

time period (**Fig. 4.3c**). Thus, NAVNs are efficient nanoformulation as it showed better photostability than free ICG and can further be exploited for imaging based biomedical applications.

4.2.5 In vitro release study of ICG

The sustained and controlled release of the theranostic agent at the target site is crucial for achieving its therapeutic effect. Therefore, an *in vitro* release study of ICG from NAVNs was investigated by the dialysis method in 1× PBS (pH 7.4) as dissolution media under dark conditions. The absorbance of released ICG was measured at 780 nm for 24 h (at the time points of 0, 2, 4, 12, 16, and 24 h) to estimate the release of ICG from NAVNs. The absorbance values corresponding to the concentration of released ICG were calculated from the standard curve of ICG. Notably, NAVNs show a slower release of ICG ($\sim 20 \pm 3\%$) in the first 4 h and reached a maximum release of $70 \pm 4\%$ in 24 h (**Fig. 4.3d**). This result confirms the suitability of NAVNs for the controlled release of the encapsulated molecule for future therapeutic assessment.

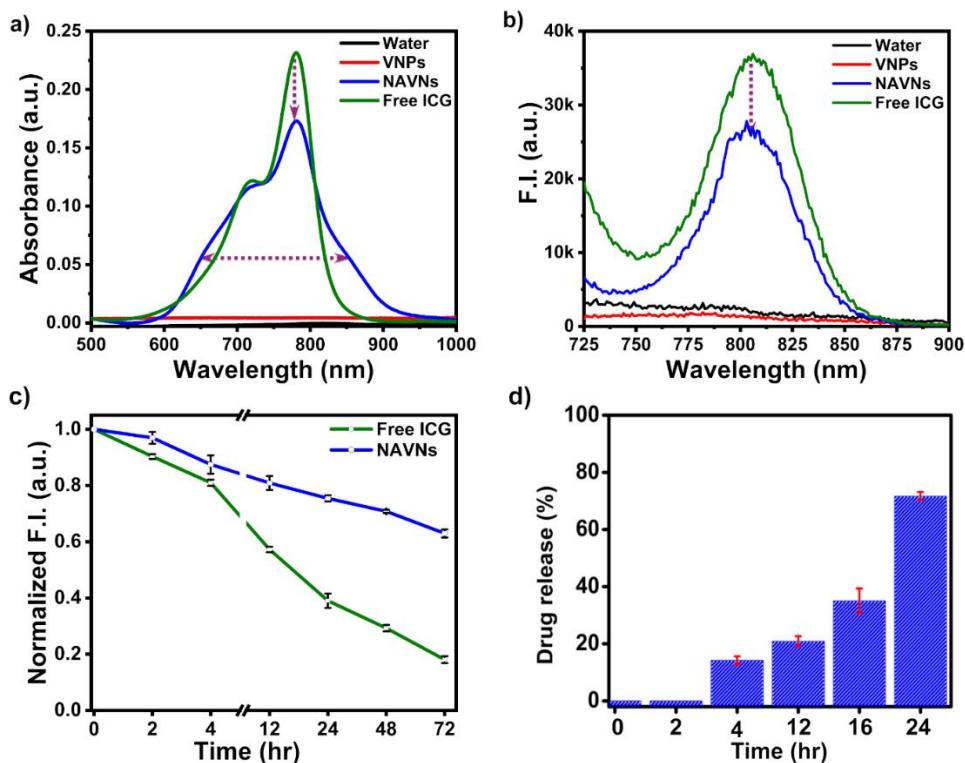


Figure 4.3 Biochemical characterization, photostability, and drug release study of free ICG and VSV-G-based nanoconstructs. (a) Absorption spectra of water, free ICG (9 μ M), VNPs (10 μ g/mL), and NAVNs displaying a reduction in absorption peak in NAVNs. (b) Emission spectra of water, free ICG (9 μ M), VNPs (10 μ g/mL), and NAVNs with a reduction in fluorescence emission of NAVNs. (c) Photostability study of free ICG and NAVNs for 72 h shows \sim 60% optically active ICG encapsulated within VNPs in comparison with less than 20% of free ICG. (d) Drug release behavior of NAVNs for 24 h depicting the controlled release pattern of ICG.

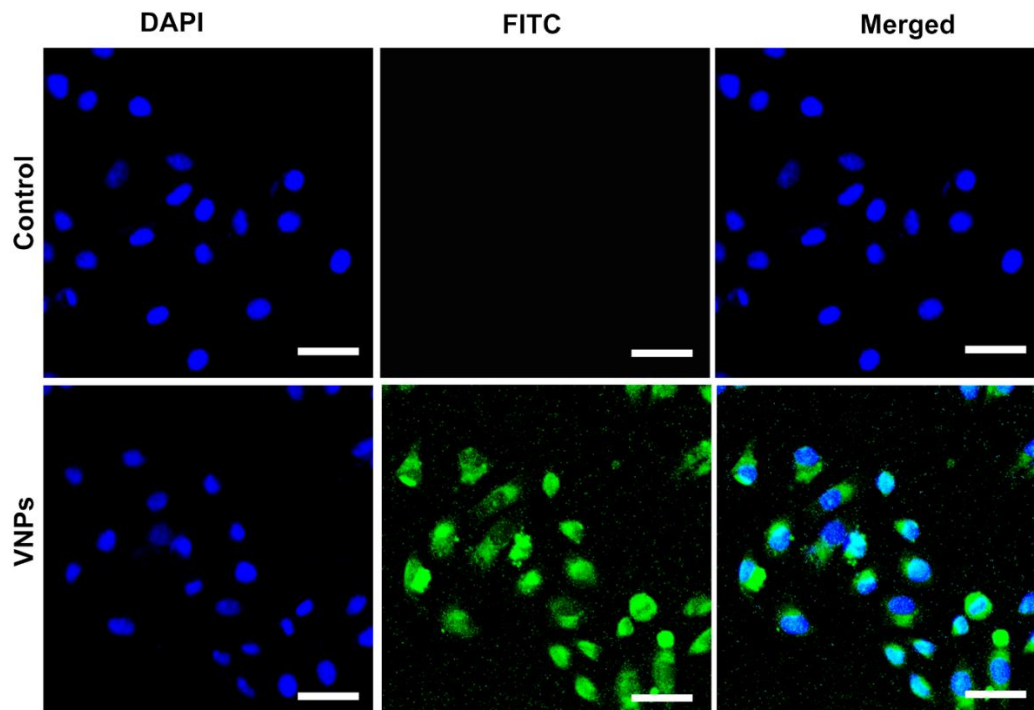


Figure 4.4 Cellular uptake of VSV-G VNPs by HeLa cells detected by immunofluorescence assay using the VSV-G polyclonal primary antibody and FITC-tagged secondary antibody. The Hoechst staining nuclei are displayed in blue color, and FITC emission is displayed in green color. Scale bar: 5 μm and magnification 10 \times .

4.2.6 Cellular uptake of VNPs

Further, the biofunctionality of VSV-G VNPs in terms of binding and entry to the host cells was determined. NAVNs were incubated with HeLa cells, and their cellular internalization was studied by immunofluorescence staining. The results reveal that VSV-G is detected within the cytoplasm of HeLa cells after 4 h treatment with VNPs (**Fig. 4.4**). At the same time, the untreated HeLa cells did not show any fluorescence emission. This result suggests that bioengineered VNPs are functionally active, while VSV-G enhanced the binding and cellular uptake of VNPs.[246] Therefore, the property of VSV-G-based VNPs to get internalized within the cells could be used to package and deliver the theranostic agent within the cells.

4.2.7 *In vitro* cellular toxicity and uptake study

The biocompatibility and imaging performance of bioengineered VNPs were assessed for biomedical applications. **Fig. 4.5a** shows the cellular cytotoxicity of VNPs and NAVNs treated cells. The cytotoxicity at different concentrations (1.6, 8, and 16 $\mu\text{g/mL}$) of VNPs and NAVNs in HeLa cells was evaluated by an MTT colorimetric assay. The result shows that more than 85% of cells remained healthy after treatment with a high concentration (16 $\mu\text{g/mL}$) of nanoconstructs (**Fig. 4.5a**). Thus, the VSV-G-based NPs have excellent biocompatibility that would be suitable for *in vivo* biomedical applications.

The NIR optical imaging was performed by incubating HeLa cells with freshly prepared NAVNs and free ICG equivalent to the concentration loaded within NAVNs for 4 h. Fluorescence images of control, ICG-treated, and NAVN-treated HeLa cells are shown in **Fig. 4.5b**. To understand the intracellular distribution of ICG, cells were counterstained with Hoechst nuclei stain. The overlay of the visible and NIR fluorescence images of HeLa cells shows that NAVNs are internalized within the cells and released ICG inside the cytoplasm. Moreover, the NAVN-treated cells emitted a higher fluorescence than the free-ICG-treated cells. Further, the integral fluorescence intensities from the overlay image of NAVNs- and free-ICG-treated cells were calculated using Image J software. The NAVNs treated cells showed significantly higher fluorescence intensity than those treated with the free ICG (**Fig. 4.5c**). Moreover, NAVNs delivered ~ 1.5 -fold higher ICG compared to the free form of ICG. Thus, the enhanced cellular uptake of NAVNs could be attributed to the fusogenic property of VSV-G protein for efficient binding and internalization within the cells. The findings reveal that NAVNs improved the SNR of *in vitro* NIR imaging, and they could be used for *in vivo* delivery of the contrast agent for disease diagnosis.

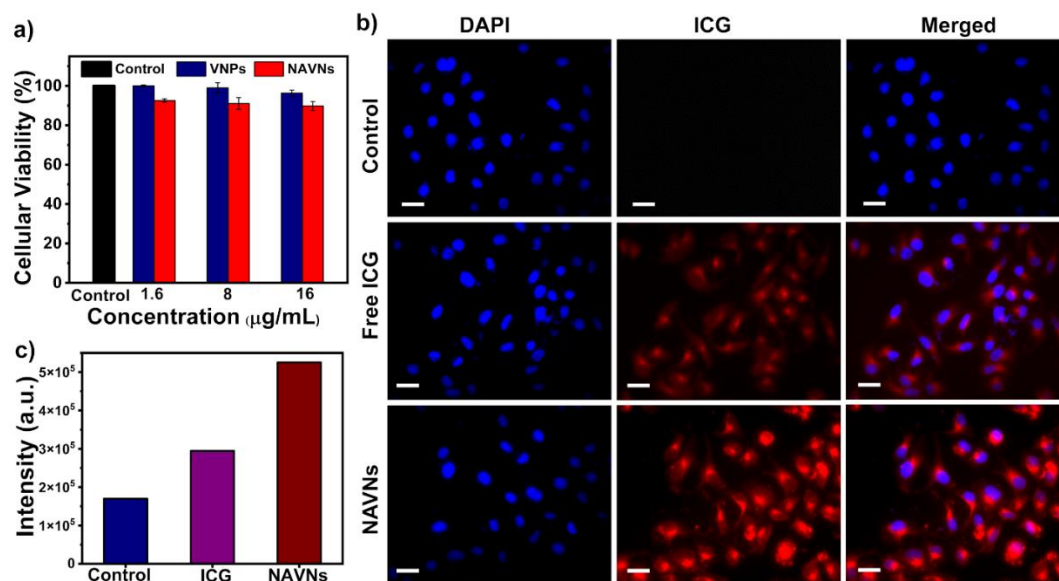


Figure 4.5 (a) *In vitro* cytotoxicity study showing the biocompatibility of VSV-G-based nanoconstructs in HeLa cells incubated with different concentrations of VNPs and NAVNs for 24 h. (b) NIR images of HeLa cells incubated with free ICG (3 μM) and NAVNs (equivalent to free ICG) for 4 h displaying the high cellular uptake of NAVNs. The Hoechst staining nuclei are displayed in blue color, and ICG emission is displayed in red color. Scale bar: 20 μm and magnification 40 \times . (c) Fluorescence emission intensity plot of NIR images of HeLa cells treated with ICG and NAVNs (equivalent to free ICG) depicting ~ 1.5 -fold enhancement in fluorescence intensity in NAVN-treated cells than free-ICG-treated cells.

4.2.8 Innate immune response study of NAVNs

An ideal theranostic nanoprobe should be compatible with the host and should not elicit an immunogenic response. To determine the intrinsic immune response induction due to the NAVNs, differential gene expression was studied in NIH/3T3 by quantitative PCR (qPCR) method after the treatment with NAVNs (10 μg) for 24 h. As a positive control, cells were infected with the wild-type VSV. Differential gene expression for interferon- β (IFN β), interferon- γ (IFN γ), and interferon regulatory factor 3 (IRF3) was investigated by qPCR using their respective primers as shown in **Table 2.2**. As anticipated, wild-type VSV displayed an increase in relative gene

expression for all tested immune responsive genes; IFN β $\sim 10^6$ -fold change (blue bar), IFN γ $\sim 2 \times 10^3$ -fold change (red bar), and IRF3 ~ 3 -fold change (green bar), respectively (**Fig. 4.6**). However, NAVNs-treated NIH/3T3 cells induced a negligible IFN β and IRF3 expression. Interestingly, NAVNs-treated cells induced ~ 15 -fold expression for IFN γ compared to nontreated cells. Although, IFN γ is a multifunctional cytokine that plays a vital role in synchronizing an innate and adaptive immune system to recognize and kill tumor cells.[247] IFN γ acts directly on cancer cells by enhancing their immunogenicity and activates macrophages or natural killer (NK) cells to kill tumors.[247] Moreover, co-loading of IFN γ with NPs has been studied to boost the tumoricidal activity using combinational immunochemotherapy for targeting tumors.[248,249] Thus, the intrinsic property of NAVNs to induce IFN γ might be beneficial for targeted therapy against tumor cells.

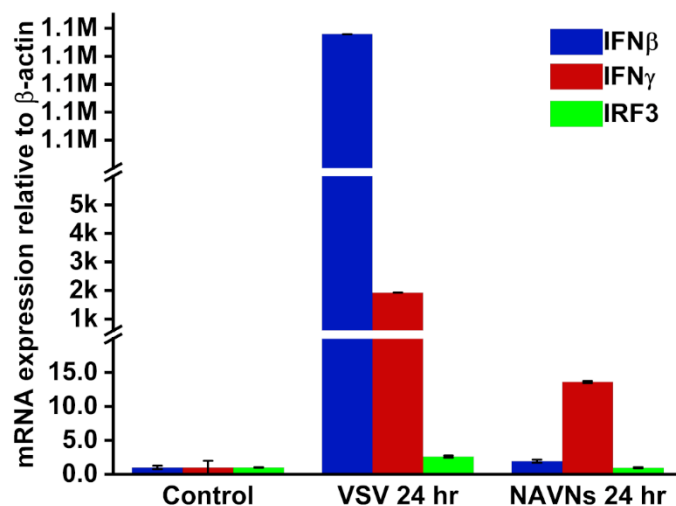


Figure 4.6 Relative immune gene expression of IFN β , IFN γ , and IRF3 in NIH/3T3 cells treated with wild-type VSV and NAVNs for 24 h depicting a negligible immune response by bioengineered VSV-G VNPs. Normalization of all samples was done by the housekeeping gene β -actin.

4.2.9 *In vivo* cytotoxicity study of VSV-G VNPs

To examine the *in vivo* cytotoxicity, the mice were administered with VNPs in three groups (control, 1 day, and 7 days post-injection; $n = 3/\text{group}$). The test groups were injected intraperitoneally (I.P.) with VNPs at a dose of 1 mg/kg of body weight, and the control animals were injected with only PBS. After 1 day and 7 days post-injection, the animals were sacrificed, and the visceral organs, i.e., liver, kidneys, spleen, and lungs, were harvested and analyzed for histological alterations. Excitingly, the microscopic evaluation of H&E-stained sections showed a normal tissue architecture for both the control and VSV-G VNPs-treated animals (**Fig. 4.7a**). This suggests that VSV-G VNPs are biocompatible as they do not show any cytotoxicity on liver, kidney, spleen, and lung tissues within 24 h and 1 week time periods. Further, during 7 days of the study period, no significant weight difference was observed between the control and VNPs-treated mice (**Fig. 4.7b**). Overall cytotoxicity study indicates that VSV-G based nanoconstructs are safe for the delivery of theranostic agents for *in vivo* biomedical applications.

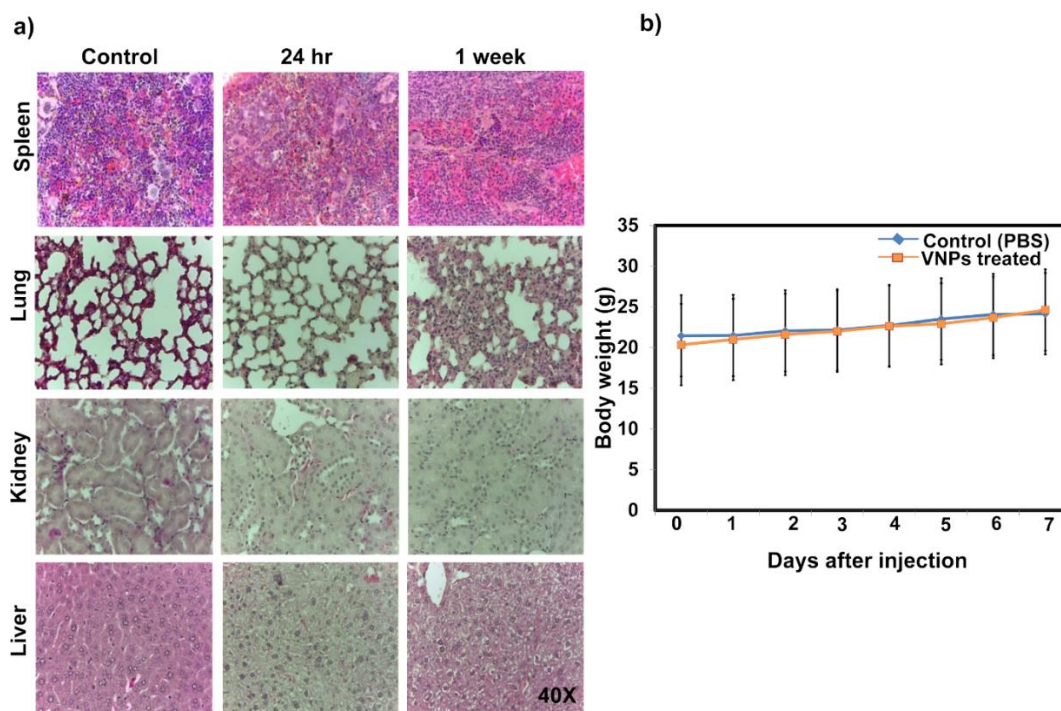


Figure 4.7 (a) Histopathology study of mice injected with control (PBS) and VNPs (1 mg/kg) at different time points showing the normal architecture of H&E-stained visceral organs in all treated groups, demonstrating the safety of VNPs. Magnification 40 \times . (b) Time-dependent body weight measurements of control and VNP-treated mice showing no significant difference in all treated groups.

4.2.10 *In vivo* biodistribution of NAVNs

Fig. 8 illustrates the whole-body distribution of free ICG and NAVNs within 48 h after a single intravenous injection. After injection, NAVNs accumulate in the liver, while the free ICG does not display any fluorescence signal (**Fig. 4.8a**). Based on this, it may be concluded that most of the free ICG was eliminated within 24 h from the body of the mouse. By 48 h, the fluorescence intensity in the liver area of mice treated with NAVNs decreased and shifted to the gastrointestinal region (**Fig. 4.8b**). When mice were dissected after 48 h of NPs injection, NAVNs were found mostly in the intestines, thus increasing the retention time of ICG (**Fig. 4.8c**). As free ICG is quickly eliminated from the body, this result suggests ICG is not released entirely from NAVNs for up to 48 hours and is retained in the body. In this way, NAVNs overcome the limitation of free ICG by enhancing their circulation half-life.

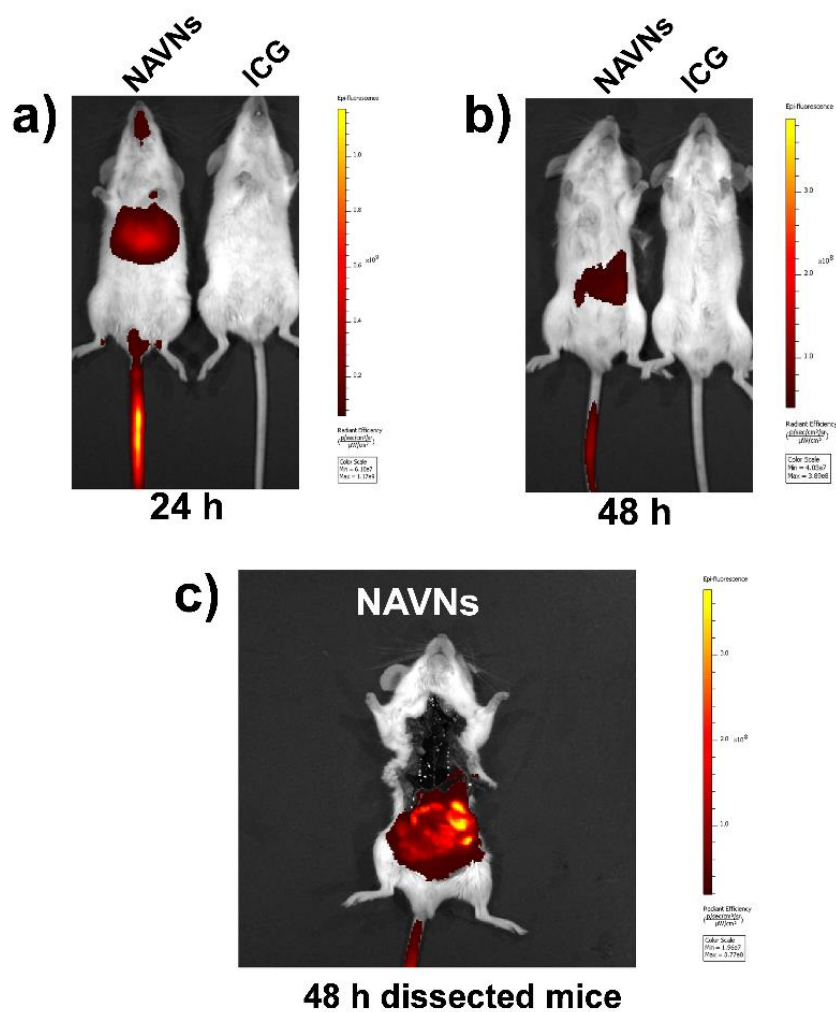


Figure 4.8 *In vivo* whole body NIR imaging of biodistribution of free ICG and NAVNs injected intravenously in BALB/c mice. (a) NIR fluorescence image of mice after 24 h post injection of ICG and NAVNs. (b) NIR fluorescence image of mice after 48 h post injection of ICG and NAVNs. (c) NIR fluorescence image of mice dissected after 48 h post injection of NAVNs.

4.3 Summary

The viral fusion protein-based nanocarriers are promising tools to enhance the cellular uptake and endolysosomal release of theranostic agents. In the present study, for the first time, we fabricated novel NIR active viral nanoconstructs by loading ICG within the VSV-G VNPs for NIR bioimaging. Our findings show that the fusogenic VSV-G induces the enhanced cellular uptake of NAVNs to release ICG within the cytoplasm of the host cells. This might be due to distinctive sites within the VSV-G protein that allow them to integrate with the targeted cells. Additionally, these nanoconstructs are safe as they are not cytotoxic in both *in vitro* and *in vivo* systems. These VNPs improved the optical stability of ICG and showed a controlled release of ICG. The NAVNs-incubated cells showed superior NIR fluorescence emission, and thus, they can be used as an exogenous contrast agent for NIR bioimaging. Therefore, bioengineered VSV-G-based VNPs can be fabricated by loading diverse payloads that are suitable for medical imaging and targeted therapy.

Chapter 5

Membrane Fusogenic Viral Protein-based Fluorescent Nanocarrier for Two-Photon Bioimaging

5.1 Introduction

Optical imaging techniques have become indispensable for detecting the dynamics of cellular, molecular processes, and disease diagnosis.[250] However, detection of early-stage cancer and metastasized tumor cells located at a deeper layer of tissue still remains as a great challenge.[251] In this context, two-photon excited fluorescence imaging has received greater attention for high-resolution deep-tissue optical imaging over the past decades.[252,253] Two-photon excitation (TPE) with NIR photons is beneficial over single-photon excitation (SPE) fluorescence imaging for deep tissue penetration with negligible auto-fluorescence, higher spatial resolution, lesser photodamage, and photobleaching effects.[254,255] To date, a wide range of TPE exogenous contrast agents have been successfully developed to improve the SNR of optical imaging for diagnostic purposes.[256,257]

Among various available fluorophores, ICG has potential for deep-tissue optical imaging as it displays both absorption and fluorescence emission in the NIR range at which the tissue autofluorescence is negligible.[43,236,258] Moreover, the TPE of the ICG involving the second singlet state (S_2) has gained attention for its application in TPE fluorescence imaging in the NIR window (650 to 950 nm).[120,259,260] In this direction, we previously reported a nonlinear excitation of ICG molecules to the S_2 state and relaxation to the S_0 state for *in vitro* TPE fluorescence bioimaging.[55]

For site specific delivery and packaging of ICG, there is a need to engineer a naturally derived biocompatible and biodegradable nanoconstruct for biomedical applications. Contextually, virus-derived nanoparticles are being explored as a nanocarrier for drug delivery.[201,261,262] Also, these virus nanoparticles (VNPs), constituting only viral structural proteins, are becoming an attractive platform for delivering theranostic agent.[207,208] VNPs derived from the fusogenic envelope protein of the animal virus are of greater interest for use as a DDS.[263,264] These VNPs enter the target cell by receptor-mediated endocytosis, where the low pH-induced conformation change in the envelope proteins mediate fusion with the endosomal membrane to deliver cargo within the cytoplasm.[265,266]

VSV-G based VNPs are regarded as efficient delivery system due to its broader tissue tropism. These VNPs facilitate endolysosomal escape, which allow cytoplasmic delivery of the cargo.[217,218] Moreover, the overexpression of VSV-G alone in mammalian cells produces VSV-G VNPs.[267] Interestingly, VSV-G-based VNPs have already been used for DNA, RNA, protein, enzyme, and CRISPR-Cas9 delivery to several types of cells and tissues.[264,268–271] In a recent study, NAVNs were fabricated for NIR optical imaging by doping ICG within VSV-G VNPs.[272] These NAVNs improved the optical stability of ICG and exhibited controlled release behavior. Moreover, NIR imaging revealed that NAVNs are efficiently uptaken by the cells and exhibited high fluorescence emission than free ICG treated cells. Additionally, the VSV-G based VNPs are biocompatible in both *in vitro* and *in vivo* experimental models. This makes the VSV-G VNPs a potential nanocarrier for use in biomedicine.

In this study, we have demonstrated the application of ICG loaded fusogenic VSV-G VNPs for multiphoton deep tissue bioimaging. The two-photon excitation of NAVNs with a femtosecond laser at ~790 nm emits bright fluorescence in the visible range enabling clear visualization of tissue microstructures at ~350 μm depth in a chicken breast tissue sample. Also, the NAVNs are efficiently uptaken by the treated cells and displayed enhancement in SNR in TPE fluorescence imaging than the free form of ICG. These results suggest that the NAVNs encapsulating ICG hold excellent promises for deep-tissue optical imaging. Thus, NAVNs encapsulating an FDA

approved contrast agent would be a potential candidate for TPE fluorescence bioimaging for early-stage cancer detection.

5.2 Results and discussions

5.2.1 Spectroscopic analysis of NAVNs

Further, the optical properties of free form of ICG (35 μM) and NAVNs (encapsulating equivalent amount of ICG) are studied by measuring the absorption spectra in the ultraviolet (UV)-NIR spectral range (350-950 nm). The free ICG displays absorption peaks at 393 nm in the visible range and at 710 nm and 780 nm in the NIR wavelength range. This is in accordance with well-established absorbance spectrums of free ICG in an aqueous solution (**Fig. 5.1a**).[187] Here, the absorption mechanism of ICG is described in the Jablonski diagram (**Fig. 5.1b**). The absorption of photons by fluorescent molecule moves electron from their ground state (S_0) to different excited state (S_1 and S_2 state). Once excited, numerous pathways were used for decaying absorbed energy to return the electron to their S_0 state. The migration of electrons from $S_1 \rightarrow S_0$ and $S_2 \rightarrow S_0$ results in the release of energy in the form of fluorescence emission. Here, the transition of ICG from its $S_0 \rightarrow S_1$ state upon absorption of a photon with 780 nm wavelength is depicted using Jablonski diagram. In addition, the absorption of 393 nm wavelength leads to the transition from $S_0 \rightarrow S_2$ excitation state (**Fig. 5.1b**). Further, the excited state of ICG releases energy by emitting fluorescence during transition of electrons from $S_1 \rightarrow S_2$ state and $S_2 \rightarrow S_0$ state. Due to the fluorescence emission during $S_2 \rightarrow S_0$ state transition, ICG violates Kasha's rule. As per Kasha's rule, the fluorescence will always originate from the vibrational ground state of the lowest excited electronic level (S_1), irrespective of the level a molecule is excited.[273] Likewise, the NAVNs also showed a similar absorption spectrum of ICG in the 300-900 nm range with broadening and suppression of the absorption band at 780 nm wavelength, confirming the fabrication of ICG loaded optically active VNPs (**Fig. 5.1a**). Furthermore, the fluorescence spectra of NAVNs upon excitation with 680 nm exhibited a reduction in the fluorescence emission as compared to free form of ICG in the 700-900 nm spectral band, as shown in **fig. 5.1c**.

The decrease in NAVNs emission may be due to aggregation-induced quenching, which indicates there is an interaction between ICG and viral protein.[274] Interestingly, the fluorescence emission of NAVNs upon 420 nm excitation also showed a reduction in fluorescence intensity and redshift in the peak compared to free ICG. Also, a significant water Raman scattering peak is observed at 520 nm (**Fig. 5.1d**). The fluorescence emission in this spectral range depicts the transition of electrons from $S_2 \rightarrow S_0$ state of ICG.

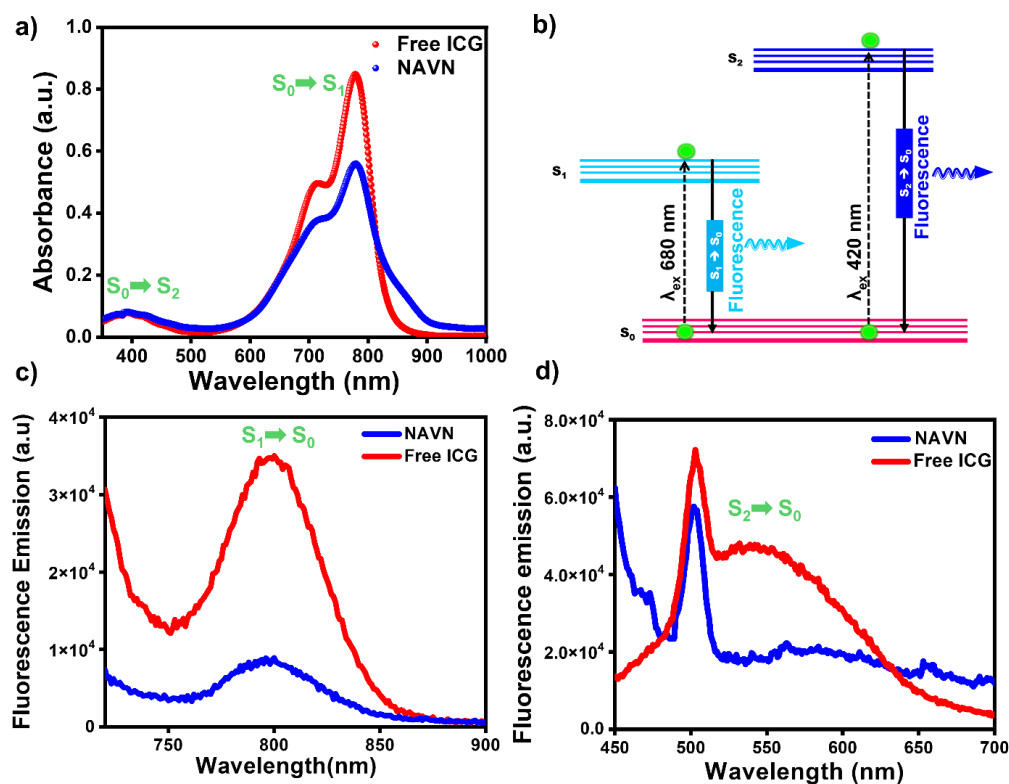


Figure 5.1 Spectroscopic analysis of free ICG and NAVNs (a) absorption spectra, (b) Jablonski diagram depicting mechanism of possible transitions from and to S_0 state to excited states, (c) fluorescence emission spectra upon 680 nm excitation (d) fluorescence emission spectra upon 420 nm excitation. S_0 is ground state, S_1 and S_2 are first and second electronic excited singlet state.

5.2.2 *In vitro* TPE fluorescence imaging using NAVNs

Earlier, our group had reported nonlinear excitation of free ICG to the S_2 state causes fluorescence emission upon relaxation to S_0 state for multiphoton optical imaging with improved SNR.[55] Subsequently, the cellular uptake and efficacy of TPE fluorescence imaging of NAVNs were explored by analyzing the TPE fluorescence image of HeLa cells after giving treatment with free ICG and NAVNs (constituting equal amount of ICG) for four hours. The TPE with λ_{ex} 790 nm showed a significant increase in fluorescence intensity in cells incubated with NAVNs than free ICG (**Fig. 5.2a**). This indicates that NAVNs are efficiently uptaken by the HeLa cells as compared to free ICG. This might be due to the cellular fusogenic property of VSV-G, which binds with the target cells to facilitate the release of cargo within the cytoplasm through the endocytotic pathway.[268,269] As expected, the control cells did not show any fluorescence emission in TPE fluorescence imaging. Importantly, NAVNs and free ICG treated cells display fluorescence emission due to direct $S_2 \rightarrow S_0$ electron transition upon linear excitation with λ_{ex} 790 nm (two-photon). The MFI of TPE images of control, free ICG, and NAVNs incubated cells indicates that the fluorescence emission from NAVNs-treated cells is ~ 1.3 fold greater than free ICG-treated cells. (**Fig. 5.2b**). These results together confirmed the effectiveness of NAVNs as a contrast agent for TPE fluorescence cellular imaging, which can be used further for *in vivo* deep-tissue optical imaging for disease diagnosis.

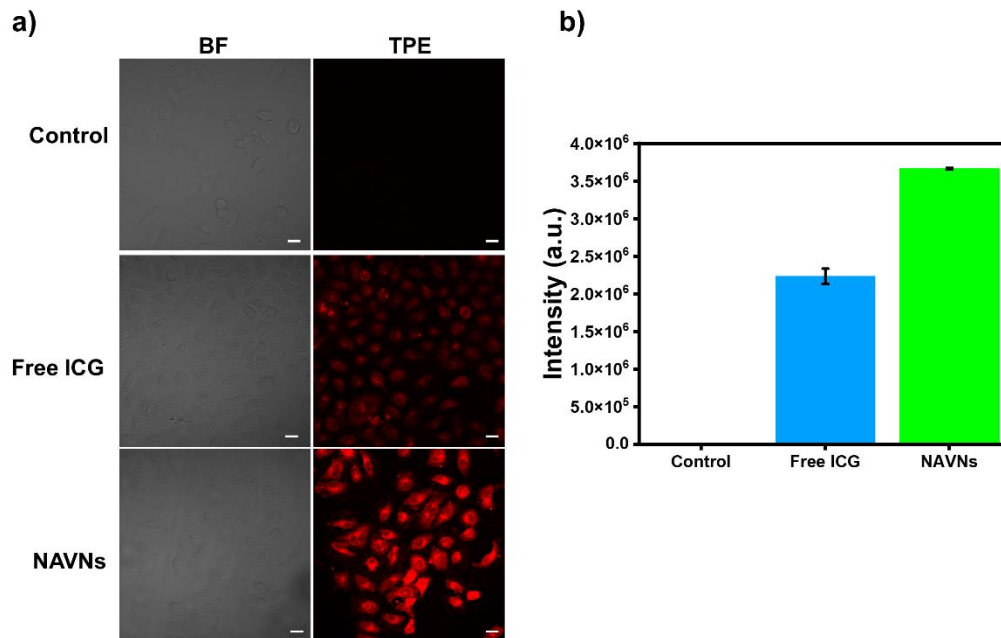


Figure 5.2 Cellular uptake study of NAVNs by TPE bioimaging. (a) TPE (λ_{ex} 790 nm) fluorescence images of HeLa cells treated with NAVNs and free form of ICG, first column signifies bright field images, and the second column signifies TPE fluorescence images ($S_2 \rightarrow S_0$ state transition) captured using multiphoton imaging system with $40 \times$ objective, scale bar, 20 μ m. (b) MFI of TPE (λ_{ex} 790 nm) fluorescence images of control, free ICG, and NAVNs treated HeLa cells.

5.2.3 Ex vivo TPE fluorescence imaging of chicken breast tissue

The TPE fluorescence bioimaging provides superior optical penetration, improved 3D spatial localization, and higher imaging resolution due to reduced autofluorescence background and optical scattering.[275] **Fig. 5.3a** depicts the visible light image of three different chicken breast tissue cuboid of ~ 350 μ m thickness treated with $1 \times$ PBS, free ICG and NAVNs for TPE fluorescence imaging. For TPE fluorescence imaging, the three different chicken tissue were treated with $1 \times$ PBS, 20 μ M of ICG (100 μ L), and NAVNs for 30 minutes. **Fig. 5.3b** demonstrates the bright field and fluorescence distribution of ICG and NAVNs in chicken tissue using two-photon laser scanning techniques. The result displayed enormous difference in

fluorescence emission in three different samples. The tissue treated with NAVNs exhibited a detectable fluorescence signal in TPE fluorescence imaging when excited by λ_{ex} 790 nm (**Fig. 5.3b**). Comparatively, free ICG treated tissue showed minimal fluorescence emission, which can be attributed to the removal of most of the unbound ICG after washing steps. In accordance with this, the NAVNs enhanced the retention of ICG within the chicken tissue even after washing steps. However, chicken tissue treated with $1\times$ PBS did not show any fluorescence emission in TPE fluorescence images. Further, the quantification of the integral fluorescence intensity suggests that the tissue section treated with NAVNs showed ~ 1.5 -fold higher fluorescence intensity as compared to the tissue treated with free ICG (**Fig. 5.3c**). The result suggests that the nanoencapsulated ICG has enhanced the contrast of TPE fluorescence images as the NAVNs improved the retention and penetration depth of ICG within the chicken tissue compared to free ICG. Thus, NAVNs could offer a promising platform for deep tissue multiphoton imaging to visualize inaccessible tissue microstructures for biomedical applications.

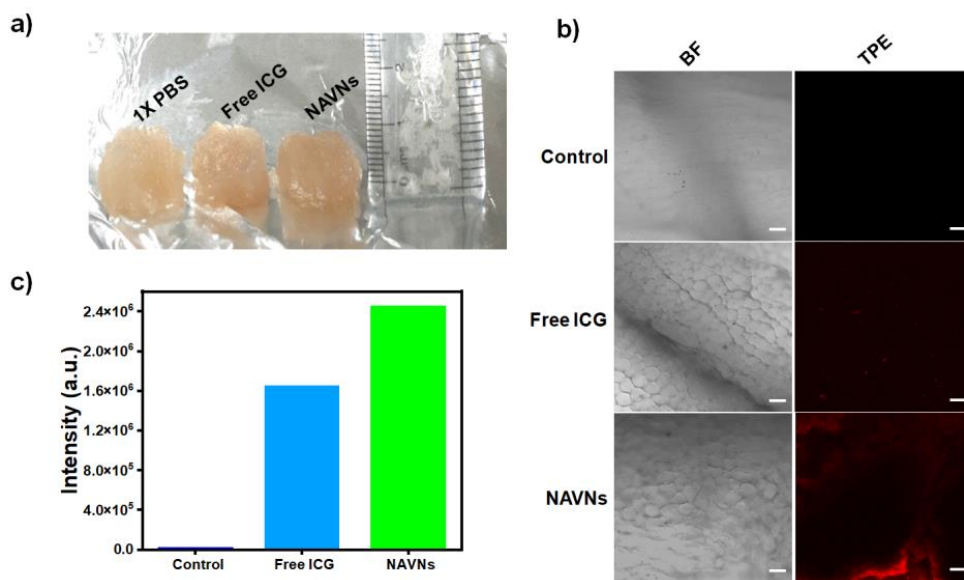


Figure 5.3 (a) Visible light image of three different chicken breast tissue cuboid of $\sim 350 \mu\text{m}$ thickness used for treatment with $1\times$ PBS, free ICG and NAVNs. (b) TPE fluorescence images of control, free ICG and NAVNs treated chicken breast tissue excited with λ_{ex} 790 nm, λ_{em} 575-630 nm. Magnification $10\times$, scale bar $100 \mu\text{m}$ (c)

MFI of TPE fluorescent images (λ_{ex} 790 nm) of control, free ICG, and NAVNs treated chicken breast tissue.

5.2.4 Z-stack of TPE fluorescence imaging of NAVNs treated chicken breast tissue

Fig. 5.4 demonstrates the fluorescence 3D distribution of NAVNs using a two-photon laser scanning method in different optical sections of chicken breast tissue. The distribution of fluorescence emission signals throughout the NAVNs treated tissue observed in montage slices indicates superior penetration ability of two-photon and fluorescence emission (**Fig. 5.4a**). Moreover, the TPE property of ICG loaded NAVNs and fluorescence emission during $S_2 \rightarrow S_0$ state transition enables deep tissue penetration for visualizing tissue's detailed morphology. Further, a 3D surface plot acquired from the mid-section of NAVNs treated chicken tissue ($Z=387/772$) showed high fluorescence signal illustrating the high penetration ability of TPE (λ_{ex} 790 nm) and fluorescence emission through the 350 μm thick tissue (**Fig. 5.4b**). Additionally, 3D rendering from Z-stack images of NAVNs treated tissue showed uniform distribution of ICG throughout the tissue enabling the visualization of the overall microstructure of tissue (**Fig. 5.4c**). Further, the merged Z-stack images of two-photon scans of this tissue showed clear architecture of the different layers (**Fig. 5.4d**). In addition, the study of fluorescence intensity profile throughout the 350 μm tissue showed maximum fluorescence intensity peak at 250 μm depth of the tissue. However, a nominal level of fluorescence intensity at other tissue section is observed (**Fig. 5.4e**). Henceforth, the tremendous tissue penetration capability of NAVNs distributed through the depth of the tissue can be explored for disease diagnosis by visualizing the change in the morphology of the tissue in clinics by using the TPE property of ICG for optical imaging.

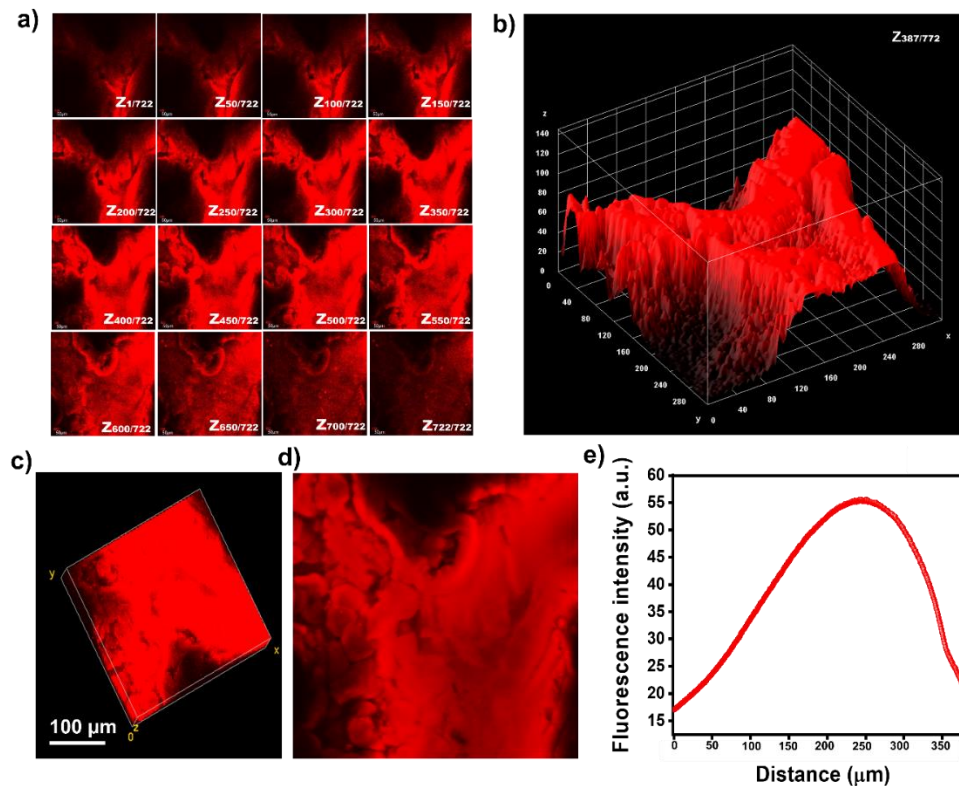


Figure 5.4 Uptake analysis of NAVNs by chicken breast tissue (a) *ex vivo* TPE fluorescence images at different depths as indicated. (b) 3D surface plot of Z-stack image. (c) 3D visualization of Z-stack image. (d) Z-projection image with average intensity. (e) fluorescence intensity profile throughout the tissue depth (350 μm).

5.3 Summary

In summary, we report the application of membrane fusogenic NAVNs for multiphoton deep tissue bioimaging using femtosecond laser. The two-photon excitation of NAVNs in the NIR region enabled clear visualization of tissue microstructures upto ~350 μm depth in a chicken breast tissues. Thus, the results of these exploratory experiments both *in vitro* and *ex vivo* settings suggest that the NAVNs are internalized into the human cervical cancer cells likely through endocytosis, demonstrating the multiphoton bioimaging potential of the NAVNs. Also, these NAVNs shows higher SNR in TPE fluorescence optical imaging compared to free form ICG. These results suggests that the NAVNs encapsulating ICG hold great

promise for deep-tissue optical imaging. Thus, the overall results open a new avenue for biomedical application of nanoencapsulated FDA approved dye for TPE fluorescence microscopy with potential applications in early-stage cancer detection.

Chapter 6

Conclusion and Scope of Future Work

6.1 Conclusion

NIR imaging gained considerable interest in clinical diagnosis due to its significant benefits, such as deep tissue imaging with high spatial resolution, minimal autofluorescence, and high SNR. High-quality NIR imaging requires biocompatible NIR active exogenous contrast agents. Specifically, ICG is an extensively investigated NIR fluorophore approved by the FDA for clinical use. However, using the free form of ICG has several drawbacks, including a short circulation half-life, poor photostability, aqueous instability, and concentration-dependent aggregation. The presented research proposes to encapsulate ICG within a biocompatible bioinspired and biomimetic NPs formulation to overcome some of its current limitations and extend their possible applications for bioimaging. This thesis demonstrates the successful fabrication of novel ICG encapsulated NIR active bioinspired and biomimetic niosomes and VSV-G based VNPs. We demonstrated the utilization of these NPs in deep tissue NIR and multiphoton optical imaging. Based on the results in this thesis, these NPs are biocompatible and improved the optical properties of ICG. These NIR active NPs also enhanced the ICG cellular uptake and fluorescence contrast of *in vitro* NIR imaging compared to the free form of ICG. Moreover, these NPs penetrate deep into the chicken breast tissue and enable clear visualization of cellular microstructures using NIR and TPE bioimaging. The results exemplified in this thesis demonstrate the applications of these biocompatible NIR active NPs with maximal NIR emission for *in vivo* bioimaging applications in clinics for disease diagnosis.

Bioinspired novel NIR active ICGNios encapsulating ICG were fabricated using cost-effective non-ionic surfactants (Tween 80, Span 80) and cholesterol as

constituting material for NIR bioimaging. The ICGNios exhibit enhanced absorption and fluorescence emission with a redshift in their spectra compared to free ICG. The redshift in fluorescence emission of ICGNios may allow for greater penetration depth than free ICG, which is beneficial for deep-tissue NIR imaging. In addition, the ICGNios improved the optical stability and fluorescence quantum yield of ICG. The ICGNios are biologically compatible and are suitable for use in the biomedical field. Through NIR fluorescence imaging, ~1.5 times enhanced cellular uptake of ICGNios compared to free ICG was investigated. Furthermore, ICGNios displayed ~7-fold enhancement in the fluorescence intensity and enabled the clear visualization of cellular structures through ~1 cm thick chicken breast tissue than free ICG. Based on our results, ICGNios could become a promising platform for deep tissue *in vivo* NIR imaging to visualize inaccessible tissue microstructures for disease diagnosis and therapeutics.

The efficient DDS must bypass endosomal mediated degradation of the payload to ensure effective delivery of contrast agents to cells. Such advancements can be made by utilizing virus-inspired NPs, as viruses have the inherent ability to successfully enter and deliver their genetic material into the cells. Inspired by this, a novel biomimetic viral structural protein-based nanovesicles encapsulating ICG were successfully fabricated in this thesis. Herein, the VSV-G protein is genetically engineered to produce VNPs from mammalian systems and was further used to encapsulate ICG for NAVNs fabrication. The bioengineered VSV-G VNPs successfully entered the cells as confirmed by the immunostaining method. The results suggest that these VNPs have inherent fusogenic properties like VSV-G protein. In addition, both *in vitro* and *in vivo* cytotoxic studies utilizing VSV-G-based nanoconstructs indicated that these NPs are biocompatible and are suitable for bioimaging applications. Morphological examination of the fabricated NAVNs using TEM displayed spherical shape vesicles with ~200 nm size. In addition, NAVNs enhanced the optical properties of ICG and exhibited controlled drug release behavior showing their effectiveness as DDS. The *in vitro* NIR imaging demonstrated that fusogenic VSV-G facilitated ~1.5-fold higher uptake of NAVNs by the cells than the free ICG. This could be attributed to specific motifs present in the VSV-G protein that

binds with the cellular receptor of the targeted cells. Subsequently, the *in vivo* NIR imaging results suggest that NAVNs have overcome the limitations of ICG by enhancing its retention time within the mice for upto two days.

The two-photon excited (TPE) NIR active fluorophores have gained significant attention due to their superior tissue penetration, high spatial resolution, and reduced optical scattering. ICG exhibits second excited singlet (S_2) state mediated two-photon excitation property which is advantageous for two-photon bioimaging. In this thesis, TPE NAVNs are used for multiphoton deep tissue bioimaging utilizing a femtosecond laser. The two-photon *in vitro* fluorescence imaging result displayed superior contrast (~1.3 fold) in the samples incubated with NAVNs, suggesting their efficient binding and cellular uptake compared to the free ICG. This demonstrates the potential of the NAVNs for multiphoton bioimaging. The two-photon *ex vivo* imaging using NAVNs as contrast agent showed high penetration capability in chicken breast tissue (~350 μm tissue depth) with the clear visualization of tissue microstructures. Also, these NAVNs improved the SNR ratio of TPE fluorescence imaging than free ICG. Notably, NAVNs encapsulating ICG holds excellent promise as an exogenous chromophore for achieving *in vivo* deep-tissue optical images with high resolution for early-stage disease diagnosis. The overall study emphasizes the efficacy of NAVNs as an efficient nanoconstruct for NIR and deep tissue multiphoton bioimaging.

6.2 Scope of Future Work

This research opens a new avenue to use bioinspired and biomimetic NPs encapsulating an FDA-approved dye for NIR and multiphoton optical imaging for early-stage disease diagnosis. Therefore, in the future, as seen in **Fig. 6.1**, the capabilities of these NIR active NPs will be evaluated for deep tissue *in vivo* optical imaging and can be implemented in clinical practice for early-stage disease diagnosis.

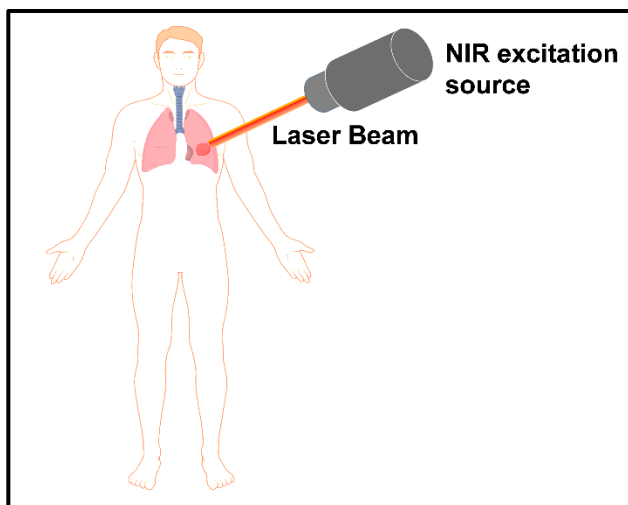


Figure 6.1 Application of bioinspired and biomimetic ICG encapsulated NPs for *in vivo* deep tissue NIR and multiphoton bioimaging.

The present study demonstrates that these NIR-active biocompatible NPs worked as effective DDS for superior NIR and multiphoton bioimaging. These NIR-active biocompatible and biodegradable NPs could be used for targeted drug delivery by conjugating the targeting moieties on their surface. In this direction the future crucial goal is to functionalize the NAVNs with cyclin RGD (cRGD), which binds specifically with cancer-cell integrins for cancer cell detection and tumor targeting. In this perspective, as illustrated in **Fig. 6.2**, the tumor-targeting peptide was displayed on the VNPs surface by inserting cRGD peptide (CDCRGDCFC) at the N-terminal region of VSV-G using recombinant DNA technology. Here the cRGD peptide was successfully inserted in the VSV-G gene and was confirmed by the Sanger sequencing method. Future efforts would be to utilize these VSVGRGD VNPs for *in vivo* targeted NIR imaging in a mouse tumor model. Therefore, this study could provide a rational basis for the development of fully targeted bioinspired and biomimetic VSV-G VNPs for preclinical and clinical applications for early-stage tumor detection and treatment.

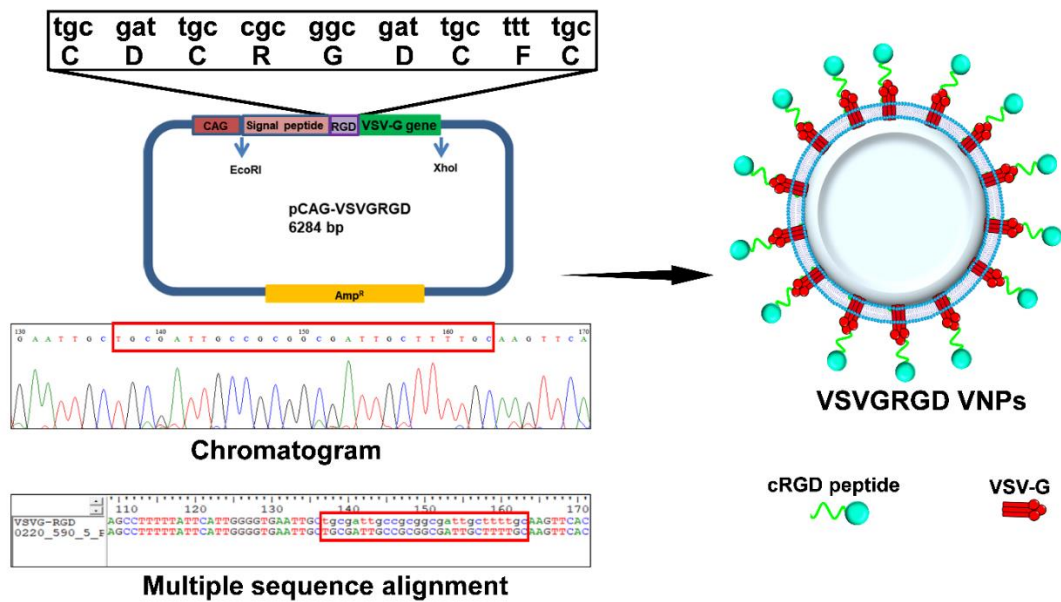


Figure 6.2 Vector map of VSV-G displaying insertion of cRGD peptide at N-terminal of VSV-G for the synthesis of VSVGRGD VNPs.

Additionally, it would also be exciting to fabricate virosomes by anchoring VSV-G/VSV-GRGD fusion protein in niosomes membrane to develop versatile, cost-effective nanovesicles for targeted delivery of contrast agents. The redshift in fluorescence emission of ICGNios and targeting peptides of VSVGRGD VNPs may facilitate the use of virosomes for deep tissue NIR and multiphoton imaging.

Appendix A

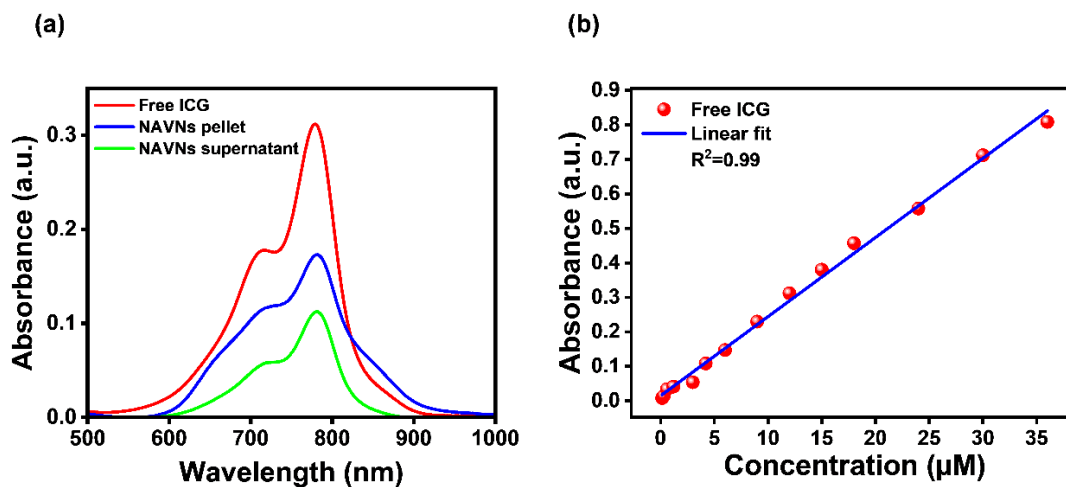


Figure A.1 Estimation of encapsulation efficiency of ICG within NAVNs (a) Absorption spectra of free ICG (12 μM), NAVNs pellet, and NAVNs supernatant (b) Calibration curve of indocyanine green (ICG) dye in water.

For estimation of EE of NAVNs, the absorption spectrum of free ICG, NAVNs pellet and NAVNs supernatant was recorded using a UV-Vis-NIR spectrophotometer (**Fig A1.a**). For preparing the calibration curve, the absorption spectra of different concentrations of free ICG were acquired. The calibration curve was plotted by absorbance versus different concentrations of free ICG using Origin 8.0 software (**Fig. A1.b**). This calibration curve was used to estimate the EE of ICG within NAVNs using equation (v).

References

1. Kang, Y.; Wu, Y.Z.; Hu, X.; Xu, X.; Sun, J.; Geng, R.; Huang, T.; Liu, X.; Ma, Y.; Chen, Y.; et al. Multicolor Bioimaging with Biosynthetic Zinc Nanoparticles and Their Application in Tumor Detection. *Sci. Rep.* **2017**, *7*, 1–11, doi:10.1038/srep45313.
2. Wallyn, J.; Anton, N.; Akram, S.; Vandamme, T.F. Biomedical Imaging: Principles, Technologies, Clinical Aspects, Contrast Agents, Limitations and Future Trends in Nanomedicines. *Pharm. Res.* **2019**, *36*, 78, doi:10.1007/s11095-019-2608-5.
3. Karatas, O.H.; Toy, E. Three-Dimensional Imaging Techniques: A Literature Review. *Eur. J. Dent.* **2014**, *08*, 132–140, doi:10.4103/1305-7456.126269.
4. Raghavendra, P.; Pullaiah, T. Biomedical Imaging Role in Cellular and Molecular Diagnostics. *Adv. Cell Mol. Diagnostics* **2018**, 85–111, doi:10.1016/b978-0-12-813679-9.00004-x.
5. Gore, J.C. Foreword. *Biomed. Imaging Appl. Adv.* **2014**, xix–xxi, doi:10.1016/B978-0-85709-127-7.50015-6.
6. Bombardieri, E.; Aktolun, C.; Baum, R.P.; Bishof-Delaloye, A.; Buscombe, J.; Chatal, J.F.; Maffioli, L.; Moncayo, R.; Mortelmans, L.; Reske, S.N. FDG-PET: Procedure Guidelines for Tumour Imaging. *Eur. J. Nucl. Med. Mol. Imaging* **2003**, *30*, doi:10.1007/s00259-003-1355-2.
7. Bertagna, F.; Biasiotto, G.; Giubbini, R. The Role of F-18-Fluorothymidine PET in Oncology. *Clin. Transl. Imaging* **2013**, *1*, 77–97, doi:10.1007/s40336-013-0014-2.
8. Alauddin, M.M. Positron Emission Tomography (PET) Imaging with (18)F-Based Radiotracers. *Am. J. Nucl. Med. Mol. Imaging* **2012**, *2*, 55–76.
9. Rieffel, J.; Chitgupi, U.; Lovell, J.F. Recent Advances in Higher-Order, Multimodal, Biomedical Imaging Agents. *Small* **2015**, *11*, 4445–4461, doi:10.1002/smll.201500735.
10. Beyer, T.; Bidaut, L.; Dickson, J.; Kachelriess, M.; Kiessling, F.; Leitgeb, R.;

- Ma, J.; Shiyam Sundar, L.K.; Theek, B.; Mawlawi, O. What Scans We Will Read: Imaging Instrumentation Trends in Clinical Oncology. *Cancer Imaging* **2020**, *20*, 1–38, doi:10.1186/s40644-020-00312-3.
11. Mettler, F.A.; Huda, W.; Yoshizumi, T.T.; Mahesh, M. Effective Doses in Radiology and Diagnostic Nuclear Medicine: A Catalog. *Radiology* **2008**, *248*, 254–263, doi:10.1148/radiol.2481071451.
 12. Estelrich, J.; Sánchez-Martín, M.J.; Busquets, M.A. Nanoparticles in Magnetic Resonance Imaging: From Simple to Dual Contrast Agents. *Int. J. Nanomedicine* **2015**, *10*, 1727–1741, doi:10.2147/IJN.S76501.
 13. Leighton, T.G. What Is Ultrasound? *Prog. Biophys. Mol. Biol.* **2007**, *93*, 3–83, doi:10.1016/j.pbiomolbio.2006.07.026.
 14. Maulik, D.; Heitmann, E.; Maulik, D. New Horizons in Doppler Ultrasound Technology: Relevance for Obstetrical Applications. *Clin. Obstet. Gynecol.* **2010**, *53*, 831–841, doi:10.1097/GRF.0b013e3181fbad5e.
 15. Nguyen, C.D.; Correia-branco, A.; Adhikari, N.; Mallidi, S.; Wallingford, M.C. New Frontiers in Placenta Tissue Imaging. *EMJ Radiol.* **2020**, *54*–62, doi:10.33590/emjradiol/19-00210.
 16. Popescu, D.P.; Choo-Smith, L.-P.; Fluerau, C.; Mao, Y.; Chang, S.; Disano, J.; Sherif, S.; Sowa, M.G. Optical Coherence Tomography: Fundamental Principles, Instrumental Designs and Biomedical Applications. *Biophys. Rev.* **2011**, *3*, 155–169, doi:10.1007/s12551-011-0054-7.
 17. Leitgeb, R.A.; Baumann, B. Multimodal Optical Medical Imaging Concepts Based on Optical Coherence Tomography. *Front. Phys.* **2018**, *6*, 1–17, doi:10.3389/fphy.2018.00114.
 18. Ying, X.; Barlow, N.J.; Feuston, M.H. Micro-Computed Tomography and Volumetric Imaging in Developmental Toxicology. *Reprod. Dev. Toxicol.* **2017**, 1183–1205, doi:10.1016/B978-0-12-804239-7.00063-9.
 19. Enslow, M.S.; Zollinger, L. V.; Morton, K.A.; Butterfield, R.I.; Kadrmas, D.J.; Christian, P.E.; Boucher, K.M.; Heilbrun, M.E.; Jensen, R.L.; Hoffman, J.M. Comparison of ¹⁸F-Fluorodeoxyglucose and ¹⁸F-Fluorothymidine PET in Differentiating Radiation Necrosis from Recurrent Glioma. *Clin. Nucl. Med.*

- 2012**, 37, 854–861, doi:10.1097/RLU.0b013e318262c76a.
20. Koudrina, A.; Derosa, M.C. Advances in Medical Imaging: Aptamer- And Peptide-Targeted MRI and CT Contrast Agents. *ACS Omega* **2020**, 5, 22691–22701, doi:10.1021/acsomega.0c02650.
 21. Lim, J.-W.; Son, S.U.; Lim, E.-K. Recent Advances in Bioimaging for Cancer Research. *State Art Nano-bioimaging* **2018**, doi:10.5772/intechopen.72725.
 22. Gautam, R.; Samuel, A.; Sil, S.; Chaturvedi, D.; Dutta, A.; Ariese, F.; Umopathy, S. Raman and Mid-Infrared Spectroscopic Imaging: Applications and Advancements. *Curr. Sci.* **2015**, 108, 341–356, doi:10.18520/cs/v108/i3/341-356.
 23. Kosaka, N.; McCann, T.E.; Mitsunaga, M.; Choyke, P.L.; Kobayashi, H. Real-Time Optical Imaging Using Quantum Dot and Related Nanocrystals. *Nanomedicine* **2010**, 5, 765–776, doi:10.2217/nnm.10.49.
 24. Wang, C.; Wang, Z.; Zhao, T.; Li, Y.; Huang, G.; Sumer, B.D.; Gao, J. Optical Molecular Imaging for Tumor Detection and Image-Guided Surgery. *Biomaterials* **2018**, 157, 62–75, doi:10.1016/j.biomaterials.2017.12.002.
 25. Gayen, S.; Alfano, R. Sensing Lesions in Tissues with Light. *Opt. Express* **1999**, 4, 475, doi:10.1364/oe.4.000475.
 26. Balas, C. Review of Biomedical Optical Imaging - A Powerful, Non-Invasive, Non-Ionizing Technology for Improving in Vivo Diagnosis. *Meas. Sci. Technol.* **2009**, 20, doi:10.1088/0957-0233/20/10/104020.
 27. Goth, W.; Lesicko, J.; Sacks, M.S.; Tunnell, J.W. Optical-Based Analysis of Soft Tissue Structures. *Annu. Rev. Biomed. Eng.* **2016**, 18, 357–385, doi:10.1146/annurev-bioeng-071114-040625.
 28. Taruttis, A.; Ntziachristos, V. Translational Optical Imaging. *Am. J. Roentgenol.* **2012**, 199, 263–271, doi:10.2214/AJR.11.8431.
 29. Lifante, J.; Shen, Y.; Ximendes, E.; Martín Rodríguez, E.; Ortgies, D.H. The Role of Tissue Fluorescence in in Vivo Optical Bioimaging. *J. Appl. Phys.* **2020**, 128, 1–17, doi:10.1063/5.0021854.
 30. Cordina, N.M.; Sayyadi, N.; Parker, L.M.; Everest-Dass, A.; Brown, L.J.; Packer, N.H. Reduced Background Autofluorescence for Cell Imaging Using

- Nanodiamonds and Lanthanide Chelates. *Sci. Rep.* **2018**, *8*, 1–14, doi:10.1038/s41598-018-22702-1.
31. Stelzle, F.; Knipfer, C.; Adler, W.; Rohde, M.; Oetter, N.; Nkenke, E.; Schmidt, M.; Tangermann-Gerk, K. Tissue Discrimination by Uncorrected Autofluorescence Spectra: A Proof-of-Principle Study for Tissue-Specific Laser Surgery. *Sensors (Switzerland)* **2013**, *13*, 13717–13731, doi:10.3390/s131013717.
 32. Lu, L.; Li, B.; Ding, S.; Fan, Y.; Wang, S.; Sun, C.; Zhao, M.; Zhao, C.X.; Zhang, F. NIR-II Bioluminescence for in Vivo High Contrast Imaging and in Situ ATP-Mediated Metastases Tracing. *Nat. Commun.* **2020**, *11*, 1–11, doi:10.1038/s41467-020-18051-1.
 33. Benninger, R.K.P.; Piston, D.W. *Two-Photon Excitation Microscopy for Unit 4.11 the Study of Living Cells and Tissues*; 2013; ISBN 0471143030.
 34. Hong, G.; Antaris, A.L.; Dai, H. Near-Infrared Fluorophores for Biomedical Imaging. *Nat. Biomed. Eng.* **2017**, *1*, doi:10.1038/s41551-016-0010.
 35. Mallidi, S.; Anbil, S.; Bulin, A.L.; Obaid, G.; Ichikawa, M.; Hasan, T. Beyond the Barriers of Light Penetration: Strategies, Perspectives and Possibilities for Photodynamic Therapy. *Theranostics* **2016**, *6*, 2458–2487, doi:10.7150/thno.16183.
 36. Chen, Y.; Bai, Y.; Han, Z.; He, W.; Guo, Z. Photoluminescence Imaging of Zn²⁺ in Living Systems. *Chem. Soc. Rev.* **2015**, *44*, 4517–4546, doi:10.1039/c5cs00005j.
 37. Pansare, V.J.; Hejazi, S.; Faenza, W.J.; Prud, R.K. 2012 Chem. Mater. V. J. Pansare.Pdf. **2012**, *24*, 812–827.
 38. Sevick-Muraca, E.M.; Houston, J.P.; Gurfinkel, M. Fluorescence-Enhanced, near Infrared Diagnostic Imaging with Contrast Agents. *Curr. Opin. Chem. Biol.* **2002**, *6*, 642–650, doi:10.1016/S1367-5931(02)00356-3.
 39. Mir, S.H.; Nagahara, L.A.; Thundat, T.; Mokarian-Tabari, P.; Furukawa, H.; Khosla, A. Review—Organic-Inorganic Hybrid Functional Materials: An Integrated Platform for Applied Technologies. *J. Electrochem. Soc.* **2018**, *165*, B3137–B3156, doi:10.1149/2.0191808jes.

40. Liu, T.M.; Conde, J.; Lipiński, T.; Bednarkiewicz, A.; Huang, C.C. Revisiting the Classification of NIR-Absorbing/Emitting Nanomaterials for in Vivo Bioapplications. *NPG Asia Mater.* **2016**, *8*, 1–25, doi:10.1038/am.2016.106.
41. Escobedo, J.O.; Rusin, O.; Lim, S.; Strongin, R.M. NIR Dyes for Bioimaging Applications. *Curr. Opin. Chem. Biol.* **2010**, *14*, 64–70, doi:10.1016/j.cbpa.2009.10.022.
42. Black, K.; Tang, R.; Egbulefu, C.; Tsen, S.W.D.; Akers, W.J.; Achilefu, S. *Fluorescence Cancer Imaging*; Second Edi.; Elsevier, 2017; Vol. 8; ISBN 9780128031988.
43. Yuan, B.; Chen, N.; Zhu, Q. Emission and Absorption Properties of Indocyanine Green in Intralipid Solution. *J. Biomed. Opt.* **2004**, *9*, 497, doi:10.1117/1.1695411.
44. Sevick-Muraca, E.M.; Sharma, R.; Rasmussen, J.C.; Marshall, M. V; Wendt, J.A.; Pham, H.Q.; Bonefas, E.; Houston, J.P.; Adams, K.E.; Blanchard, D.K.; et al. Imaging of Lymph Flow in Breast Cancer Patients after Microdose Administration of a Methods : Feasibility Study. *Radiology* **2008**, *246*, 734–741.
45. Crane, L.M.A.; Themelis, G.; Arts, H.J.G.; Buddingh, K.T.; Brouwers, A.H.; Ntziachristos, V.; Van Dam, G.M.; Van Der Zee, A.G.J. Intraoperative Near-Infrared Fluorescence Imaging for Sentinel Lymph Node Detection in Vulvar Cancer: First Clinical Results. *Gynecol. Oncol.* **2011**, *120*, 291–295, doi:10.1016/j.ygyno.2010.10.009.
46. Van Der Vorst, J.R.; Schaafsma, B.E.; Verbeek, F.P.R.; Swijnenburg, R.J.; Hutteman, M.; Liefers, G.J.; Van De Velde, C.J.H.; Frangioni, J. V.; Vahrmeijer, A.L. Dose Optimization for Near-Infrared Fluorescence Sentinel Lymph Node Mapping in Patients with Melanoma. *Br. J. Dermatol.* **2013**, *168*, 93–98, doi:10.1111/bjd.12059.
47. Frangioni, J. V. In Vivo Near-Infrared Fluorescence Imaging. *Curr. Opin. Chem. Biol.* **2003**, *7*, 626–634, doi:10.1016/j.cbpa.2003.08.007.
48. Hope-Ross, M.; Yannuzzi, L.A.; Gragoudas, E.S.; Guyer, D.R.; Slakter, J.S.; Sorenson, J.A.; Krupsky, S.; Orlock, D.A.; Puliafito, C.A. Adverse Reactions

- Due to Indocyanine Green. *Ophthalmology* **1994**, *101*, 529–533, doi:10.1016/S0161-6420(94)31303-0.
49. Bahmani, B.; Bacon, D.; Anvari, B. Erythrocyte-Derived Photo-Theranostic Agents: Hybrid Nano-Vesicles Containing Indocyanine Green for near Infrared Imaging and Therapeutic Applications. *Sci. Rep.* **2013**, *3*, 1–7, doi:10.1038/srep02180.
50. Peiretti, E.; Iovino, C. Indocyanine Green Angiography. *Cent. Serous Chorioretinopathy* **2019**, 97–113, doi:10.1016/B978-0-12-816800-4.00009-7.
51. Xiao, Q.; Chen, T.; Chen, S. Fluorescent Contrast Agents for Tumor Surgery (Review). *Exp. Ther. Med.* **2018**, *16*, 1577–1585, doi:10.3892/etm.2018.6401.
52. Bahmani, B.; Lytle, C.Y.; Walker, A.M.; Gupta, S.; Vullev, V.I.; Anvari, B. Effects of Nanoencapsulation and PEGylation on Biodistribution of Indocyanine Green in Healthy Mice: Quantitative Fluorescence Imaging and Analysis of Organs. *Int. J. Nanomedicine* **2013**, *8*, 1609–1620, doi:10.2147/IJN.S42511.
53. Zhang, X.; Li, N.; Liu, Y.; Ji, B.; Wang, Q.; Wang, M.; Dai, K.; Gao, D. On-Demand Drug Release of ICG-Liposomal Wedelolactone Combined Photothermal Therapy for Tumor. *Nanomedicine Nanotechnology, Biol. Med.* **2016**, *12*, 2019–2029, doi:10.1016/j.nano.2016.05.013.
54. Björnsson, Ó.G.; Murphy, R.; Chadwick, V.S. Physicochemical Studies of Indocyanine Green (ICG): Absorbance/Concentration Relationship, PH Tolerance and Assay Precision in Various Solvents. *Experientia* **1982**, *38*, 1441–1442, doi:10.1007/BF01955757.
55. Kumari, A.; Gupta, S. Two-Photon Excitation and Direct Emission from S2 State of U.S. Food and Drug Administration Approved near-Infrared Dye: Application of Anti-Kasha's Rule for Two-Photon Fluorescence Imaging. *J. Biophotonics* **2019**, *12*, doi:10.1002/jbio.201800086.
56. West, W.; Pearce, S. The Dimeric State of Cyanine Dyes. *J. Phys. Chem.* **1965**, *69*, 1894–1903, doi:10.1021/j100890a019.
57. Haritoglou, C.; Gandorfer, A.; Schaumberger, M.; Tadayoni, R.; Gandorfer, A.; Kampik, A. Light-Absorbing Properties and Osmolarity of Indocyanine-Green

- Depending on Concentration and Solvent Medium. *Investig. Ophthalmol. Vis. Sci.* **2003**, *44*, 2722–2729, doi:10.1167/iovs.02-1283.
58. Weigand, R.; Rotermund, F.; Penzkofer, A. Aggregation Dependent Absorption Reduction of Indocyanine Green. *J. Phys. Chem. A* **1997**, *101*, 7729–7734, doi:10.1021/jp9700894.
59. Kirchherr, A.K.; Briel, A.; Mäder, K. Stabilization of Indocyanine Green by Encapsulation within Micellar Systems. *Mol. Pharm.* **2009**, *6*, 480–491, doi:10.1021/mp8001649.
60. Landsman, M.L.J.; Kwant, G.; Mook, G.A.; Zijlstra, W.G. Light Absorbing Properties, Stability, and Spectral Stabilization of Indocyanine Green. *J. Appl. Physiol.* **1976**, *40*, 575–583, doi:10.1152/jappl.1976.40.4.575.
61. Berlepsch, H. V.; Böttcher, C. Cryo-Transmission Electron Microscopy Reveals Mesoscopic H- and J-Aggregates of near Infrared Cyanine Dyes. *J. Photochem. Photobiol. A Chem.* **2010**, *214*, 16–21, doi:10.1016/j.jphotochem.2010.05.025.
62. Ogawa, M.; Kosaka, N.; Choyke, P.L.; Kobayashi, H. H-Type Dimer Formation of Fluorophores: A Mechanism for Activatable, in Vivo Optical Molecular Imaging. *ACS Chem. Biol.* **2009**, *4*, 535–546, doi:10.1021/cb900089j.
63. Neckers, D.C. Aggregation Phenomena in Xanthene Dyed OSCAR VALDES-AGUILERA" and. *Acc. Chem. Res* **1989**, *22*, 171–177.
64. J-Aggregates - Takayoshi Kobayashi - Google Books.
65. Bricks, J.L.; Slominskii, Y.L.; Panas, I.D.; Demchenko, A.P. Fluorescent J-Aggregates of Cyanine Dyes: Basic Research and Applications Review. *Methods Appl. Fluoresc.* **2018**, *6*, doi:10.1088/2050-6120/aa8d0d.
66. Holzer, W.; Mauerer, M.; Penzkofer, A.; Szeimies, R.M.; Abels, C.; Landthaler, M.; Bäuml, W. Photostability and Thermal Stability of Indocyanine Green. *J. Photochem. Photobiol. B Biol.* **1998**, *47*, 155–164, doi:10.1016/S1011-1344(98)00216-4.
67. Sutterer, W.F.; Hardin, S.E.; Benson, R.W.; Jerome Krovetz, L.; Schiebler, G.L. Optical Behavior of Indocyanine Green Dye in Blood and in Aqueous Solution. *Am. Heart J.* **1966**, *72*, 345–350, doi:10.1016/S0002-8703(66)80008-

- X.
68. Engel, E.; Schraml, R.; Maisch, T.; Kobuch, K.; Konig, B.; Szeimies, R.M.; Hillenkamp, J.; Bäuml, W.; Vasold, R. Light-Induced Decomposition of Indocyanine Green. *Investig. Ophthalmol. Vis. Sci.* **2008**, *49*, 1777–1783, doi:10.1167/iovs.07-0911.
 69. Zhou, J.; Yang, F.; Jiang, G.; Wang, J. Applications of Indocyanine Green Based Near-Infrared Fluorescence Imaging in Thoracic Surgery. *J. Thorac. Dis.* **2016**, *8*, S738–S743, doi:10.21037/jtd.2016.09.49.
 70. Alander, J.T.; Kaartinen, I.; Laakso, A.; Pätilä, T.; Spillmann, T.; Tuchin, V. V.; Venermo, M.; Välisuo, P. A Review of Indocyanine Green Fluorescent Imaging in Surgery. *Int. J. Biomed. Imaging* **2012**, *2012*, doi:10.1155/2012/940585.
 71. Chen, Q.; Chen, J.; He, M.; Bai, Y.; Yan, H.; Zeng, N.; Liu, F.; Wen, S.; Song, L.; Sheng, Z.; et al. Novel Small Molecular Dye-Loaded Lipid Nanoparticles with Efficient near-Infrared-II Absorption for Photoacoustic Imaging and Photothermal Therapy of Hepatocellular Carcinoma. *Biomater. Sci.* **2019**, *7*, 3165–3177, doi:10.1039/c9bm00528e.
 72. Kim, Y.Y.; Shin, H.J.; Kim, M.J.; Lee, M.J. Comparison of Effective Radiation Doses from X-Ray, CT, and PET/ CT in Pediatric Patients with Neuroblastoma Using a Dose Monitoring Program. *Diagnostic Interv. Radiol.* **2016**, *22*, 390–394, doi:10.5152/dir.2015.15221.
 73. Yan, H.; Chen, J.; Li, Y.; Bai, Y.; Wu, Y.; Sheng, Z.; Song, L.; Liu, C.; Zhang, H. Ultrasmall Hybrid Protein-Copper Sulfide Nanoparticles for Targeted Photoacoustic Imaging of Orthotopic Hepatocellular Carcinoma with a High Signal-to-Noise Ratio. *Biomater. Sci.* **2019**, *7*, 92–103, doi:10.1039/c8bm00767e.
 74. Brunner, J.; Yao, J.; Laufer, J.; Bohndiek, S.E. Photoacoustic Imaging Using Genetically Encoded Reporters: A Review. *J. Biomed. Opt.* **2017**, *22*, 070901, doi:10.1117/1.jbo.22.7.070901.
 75. Wilson, K.E.; Bachawal, S. V.; Abou-Elkacem, L.; Jensen, K.; Machtaler, S.; Tian, L.; Willmann, J.K. Spectroscopic Photoacoustic Molecular Imaging of

- Breast Cancer Using a B7-H3-Targeted ICG Contrast Agent. *Theranostics* **2017**, *7*, 1463–1476, doi:10.7150/thno.18217.
76. Zhang, J.; Zhen, X.; Upputuri, P.K.; Pramanik, M.; Chen, P.; Pu, K. Activatable Photoacoustic Nanoprobes for In Vivo Ratiometric Imaging of Peroxynitrite. *Adv. Mater.* **2017**, *29*, 2–9, doi:10.1002/adma.201604764.
 77. Ferrauto, G.; Carniato, F.; Di Gregorio, E.; Tei, L.; Botta, M.; Aime, S. Large Photoacoustic Effect Enhancement for ICG Confined inside MCM-41 Mesoporous Silica Nanoparticles. *Nanoscale* **2017**, *9*, 99–103, doi:10.1039/c6nr08282c.
 78. Okumura, K.; Yoshida, K.; Yoshioka, K.; Aki, S.; Yoneda, N.; Inoue, D.; Kitao, A.; Ogi, T.; Kozaka, K.; Minami, T.; et al. Photoacoustic Imaging of Tumour Vascular Permeability with Indocyanine Green in a Mouse Model. *Eur. Radiol. Exp.* **2018**, *2*, doi:10.1186/s41747-018-0036-7.
 79. Guan, T.; Shang, W.; Li, H.; Yang, X.; Fang, C.; Tian, J.; Wang, K. From Detection to Resection: Photoacoustic Tomography and Surgery Guidance with Indocyanine Green Loaded Gold Nanorod@liposome Core-Shell Nanoparticles in Liver Cancer. *Bioconjug. Chem.* **2017**, *28*, 1221–1228, doi:10.1021/acs.bioconjchem.7b00065.
 80. Capozza, M.; Blasi, F.; Valbusa, G.; Oliva, P.; Cabella, C.; Buonsanti, F.; Cordaro, A.; Pizzuto, L.; Maiocchi, A.; Poggi, L. Photoacoustic Imaging of Integrin-Overexpressing Tumors Using a Novel ICG-Based Contrast Agent in Mice. *Photoacoustics* **2018**, *11*, 36–45, doi:10.1016/j.pacs.2018.07.007.
 81. Gao, C.; Deng, Z.J.; Peng, D.; Jin, Y.S.; Ma, Y.; Li, Y.Y.; Zhu, Y.K.; Xi, J.Z.; Tian, J.; Dai, Z.F.; et al. Near-Infrared Dye-Loaded Magnetic Nanoparticles as Photoacoustic Contrast Agent for Enhanced Tumor Imaging. *Cancer Biol. Med.* **2016**, *13*, 349–359, doi:10.20892/j.issn.2095-3941.2016.0048.
 82. Zerda, A. De; Bodapati, S.; Teed, R.; May, S.Y.; Tabakman, S.M.; Liu, Z.; Khuri-yakub, B.T.; Chen, X.; Dai, H.; Sanjiv, S. Sensitivity and Multiplexing Studies in Living Mice. **2013**, *6*, 4694–4701, doi:10.1021/nn204352r.Family.
 83. Wang, H.; Li, X.; Tse, B.W.-C.; Yang, H.; Thorling, C.A.; Liu, Y.; Touraud, M.; Chouane, J.B.; Liu, X.; Roberts, M.S.; et al. Indocyanine Green-

- Incorporating Nanoparticles for Cancer Theranostics. *Theranostics* **2018**, *8*, 1227–1242, doi:10.7150/thno.22872.
84. Wang, H.; Liu, C.; Gong, X.; Hu, D.; Lin, R.; Sheng, Z.; Zheng, C.; Yan, M.; Chen, J.; Cai, L.; et al. In Vivo Photoacoustic Molecular Imaging of Breast Carcinoma with Folate Receptor-Targeted Indocyanine Green Nanoprobes. *Nanoscale* **2014**, *6*, 14270–14279, doi:10.1039/c4nr03949a.
85. Sano, K.; Ohashi, M.; Kanazaki, K.; Ding, N.; Deguchi, J.; Kanada, Y.; Ono, M.; Saji, H. In Vivo Photoacoustic Imaging of Cancer Using Indocyanine Green-Labeled Monoclonal Antibody Targeting the Epidermal Growth Factor Receptor. *Biochem. Biophys. Res. Commun.* **2015**, *464*, 820–825, doi:10.1016/j.bbrc.2015.07.042.
86. Lv, R.; Wang, D.; Xiao, L.; Chen, G.; Xia, J.; Prasad, P.N. Stable ICG-Loaded Upconversion Nanoparticles: Silica Core/Shell Theranostic Nanoplatfrom for Dual-Modal Upconversion and Photoacoustic Imaging Together with Photothermal Therapy. *Sci. Rep.* **2017**, *7*, 1–11, doi:10.1038/s41598-017-16016-x.
87. Higbee-Dempsey, E.; Amirshaghghi, A.; Case, M.J.; Miller, J.; Busch, T.M.; Tsourkas, A. Indocyanine Green-Coated Gold Nanoclusters for Photoacoustic Imaging and Photothermal Therapy. *Adv. Ther.* **2019**, *2*, 1–12, doi:10.1002/adtp.201900088.
88. Morita, Y.; Sakaguchi, T.; Unno, N.; Shibasaki, Y.; Suzuki, A.; Fukumoto, K.; Inaba, K.; Baba, S.; Takehara, Y.; Suzuki, S.; et al. Detection of Hepatocellular Carcinomas with Near-Infrared Fluorescence Imaging Using Indocyanine Green: Its Usefulness and Limitation. *Int. J. Clin. Oncol.* **2013**, *18*, 232–241, doi:10.1007/s10147-011-0367-3.
89. Schaafsma, B.E.; Mieog, J.S.D.; Hutteman, M.; Van Der Vorst, J.R.; Kuppen, P.J.K.; Löwik, C.W.G.M.; Frangioni, J. V.; Van De Velde, C.J.H.; Vahrmeijer, A.L. The Clinical Use of Indocyanine Green as a Near-Infrared Fluorescent Contrast Agent for Image-Guided Oncologic Surgery. *J. Surg. Oncol.* **2011**, *104*, 323–332, doi:10.1002/jso.21943.
90. Sevick-Muraca, E.M. Translation of Near-Infrared Fluorescence Imaging

- Technologies: Emerging Clinical Applications. *Annu. Rev. Med.* **2012**, *63*, 217–231, doi:10.1146/annurev-med-070910-083323.
91. Song, S.; Shen, H.; Yang, T.; Wang, L.; Fu, H.; Chen, H.; Zhang, Z. Indocyanine Green Loaded Magnetic Carbon Nanoparticles for Near Infrared Fluorescence/Magnetic Resonance Dual-Modal Imaging and Photothermal Therapy of Tumor. *ACS Appl. Mater. Interfaces* **2017**, *9*, 9484–9495, doi:10.1021/acsami.7b00490.
 92. Barth, B.M.; Sharma, K.R.; Erhan, K.I.; Morgan, T.T.; Shanmugavelandy, S.S.; Kaiser, J.M.; McGovern, C.; Matters, G.L.; Smith, J.P.; Kester, M.; et al. Bioconjugation of Calcium Phosphosilicate Composite Nanoparticles. *ACS Nano* **2010**, *4*, 1279–1287.
 93. Tsuchimochi, M.; Hayama, K.; Toyama, M.; Sasagawa, I.; Tsubokawa, N. Dual-Modality Imaging with ^{99m}Tc and Fluorescent Indocyanine Green Using Surface-Modified Silica Nanoparticles for Biopsy of the Sentinel Lymph Node: An Animal Study. *EJNMMI Res.* **2013**, *3*, 1–11, doi:10.1186/2191-219X-3-33.
 94. Zeng, C.; Shang, W.; Wang, K.; Chi, C.; Jia, X.; Feng, C.; Yang, D.; Ye, J.; Fang, C.; Tian, J. Intraoperative Identification of Liver Cancer Microfoci Using a Targeted Near-Infrared Fluorescent Probe for Imaging-Guided Surgery. *Sci. Rep.* **2016**, *6*, 1–10, doi:10.1038/srep21959.
 95. Nakamura, T.; Sugihara, F.; Matsushita, H.; Yoshioka, Y.; Mizukami, S.; Kikuchi, K. Mesoporous Silica Nanoparticles for ¹⁹F Magnetic Resonance Imaging, Fluorescence Imaging, and Drug Delivery. *Chem. Sci.* **2015**, *6*, 1986–1990, doi:10.1039/c4sc03549f.
 96. Zhao, J.Y.; Chen, G.; Gu, Y.P.; Cui, R.; Zhang, Z.L.; Yu, Z.L.; Tang, B.; Zhao, Y.F.; Pang, D.W. Ultrasmall Magnetically Engineered Ag₂Se Quantum Dots for Instant Efficient Labeling and Whole-Body High-Resolution Multimodal Real-Time Tracking of Cell-Derived Microvesicles. *J. Am. Chem. Soc.* **2016**, *138*, 1893–1903, doi:10.1021/jacs.5b10340.
 97. Song, G.; Liang, C.; Gong, H.; Li, M.; Zheng, X.; Cheng, L.; Yang, K.; Jiang, X.; Liu, Z. Core-Shell MnSe@Bi₂Se₃ Fabricated via a Cation Exchange Method as Novel Nanotheranostics for Multimodal Imaging and Synergistic

- Thermoradiotherapy. *Adv. Mater.* **2015**, *27*, 6110–6117, doi:10.1002/adma.201503006.
98. Nie, L.; Chen, X. Structural and Functional Photoacoustic Molecular Tomography Aided by Emerging Contrast Agents. *Chem. Soc. Rev.* **2014**, *43*, 7132–7170, doi:10.1039/c4cs00086b.
99. Shin, T.H.; Choi, Y.; Kim, S.; Cheon, J. Recent Advances in Magnetic Nanoparticle-Based Multi-Modal Imaging. *Chem. Soc. Rev.* **2015**, *44*, 4501–4516, doi:10.1039/c4cs00345d.
100. Weissleder, R.; Nahrendorf, M.; Pittet, M.J. Imaging Macrophages with Nanoparticles. *Nat. Mater.* **2014**, *13*, 125–138, doi:10.1038/nmat3780.
101. Doolittle, E.; Peiris, P.M.; Doron, G.; Goldberg, A.; Tucci, S.; Rao, S.; Shah, S.; Sylvestre, M.; Govender, P.; Turan, O.; et al. Spatiotemporal Targeting of a Dual-Ligand Nanoparticle to Cancer Metastasis. *ACS Nano* **2015**, *9*, 8012–8021, doi:10.1021/acsnano.5b01552.
102. Li, Z.; Yin, S.; Cheng, L.; Yang, K.; Li, Y.; Liu, Z. Magnetic Targeting Enhanced Theranostic Strategy Based on Multimodal Imaging for Selective Ablation of Cancer. *Adv. Funct. Mater.* **2014**, *24*, 2312–2321, doi:10.1002/adfm.201303345.
103. Santra, S.; Kaittanis, C.; Grimm, J.; Perez, J.M. Drug/Dye-Loaded, Multifunctional Iron Oxide Nanoparticles for Combined Targeted Cancer Therapy and Dual Optical/Magnetic Resonance Imaging. *Small* **2009**, *5*, 1862–1868, doi:10.1002/smll.200900389.
104. Fang, C.; Zhang, M. Multifunctional Magnetic Nanoparticles for Medical Imaging Applications. *J. Mater. Chem.* **2009**, *19*, 6258–6266, doi:10.1039/b902182e.
105. Sharma, P.; Bengtsson, N.E.; Walter, G.A.; Sohn, H.B.; Zhou, G.; Iwakuma, N.; Zeng, H.; Grobmyer, S.R.; Scott, E.W.; Moudgil, B.M. Gadolinium-Doped Silica Nanoparticles Encapsulating Indocyanine Green for near Infrared and Magnetic Resonance Imaging. *Small* **2012**, *8*, 2856–2868, doi:10.1002/smll.201200258.
106. Ito, A.; Ito, Y.; Matsushima, S.; Tsuchida, D.; Ogasawara, M.; Hasegawa, J.;

- Misawa, K.; Kondo, E.; Kaneda, N.; Nakanishi, H. New Whole-Body Multimodality Imaging of Gastric Cancer Peritoneal Metastasis Combining Fluorescence Imaging with ICG-Labeled Antibody and MRI in Mice. *Gastric Cancer* **2014**, *17*, 497–507, doi:10.1007/s10120-013-0316-0.
107. You, Q.; Zhang, K.; Liu, J.; Liu, C.; Wang, H.; Wang, M.; Ye, S.; Gao, H.; Lv, L.; Wang, C.; et al. Persistent Regulation of Tumor Hypoxia Microenvironment via a Bioinspired Pt-Based Oxygen Nanogenerator for Multimodal Imaging-Guided Synergistic Phototherapy. *Adv. Sci.* **2020**, *7*.
108. Shi, X.; Wang, S.H.; Swanson, S.D.; Ge, S.; Cao, Z.; Van Antwerp, M.E.; Landmark, K.J.; Baker, J.R. Dendrimer-Functionalized Shell-Crosslinked Iron Oxide Nanoparticles for in-Vivo Magnetic Resonance Imaging of Tumors. *Adv. Mater.* **2008**, *20*, 1671–1678, doi:10.1002/adma.200702770.
109. Ravoori, M.K.; Singh, S.; Bhavane, R.; Sood, A.K.; Anvari, B.; Bankson, J.; Annapragada, A.; Kundra, V. Multimodal Magnetic Resonance and Near-Infrared-Fluorescent Imaging of Intraperitoneal Ovarian Cancer Using a Dual-Mode-Dual-Gadolinium Liposomal Contrast Agent. *Sci. Rep.* **2016**, *6*, 1–11, doi:10.1038/srep38991.
110. Park, H.; Yang, J.; Seo, S.; Kim, K.; Suh, J.; Kim, D.; Haam, S.; Yoo, K.H. Multifunctional Nanoparticles for Photothermally Controlled Drug Delivery and Magnetic Resonance Imaging Enhancement. *Small* **2008**, *4*, 192–196, doi:10.1002/smll.200700807.
111. Chen, Q.; Shang, W.; Zeng, C.; Wang, K.; Liang, X.; Chi, C.; Liang, X.; Yang, J.; Fang, C.; Tian, J. Theranostic Imaging of Liver Cancer Using Targeted Optical/MRI Dual-Modal Probes. *Oncotarget* **2017**, *8*, 32741–32751, doi:10.18632/oncotarget.15642.
112. Ntziachristos, V.; Yodh, A.G.; Schnall, M.; Chance, B. Concurrent MRI and Diffuse Optical Tomography of Breast after Indocyanine Green Enhancement. *Proc. Natl. Acad. Sci. U. S. A.* **2000**, *97*, 2767–2772, doi:10.1073/pnas.040570597.
113. Amos, W.B.; White, J.G.; Fordham, M. Use of Confocal Imaging in the Study of Biological Structures. *Appl. Opt.* **1987**, *26*, 3239, doi:10.1364/ao.26.003239.

114. Piston, D.W. Imaging Living Cells and Tissues by Two-Photon Excitation Microscopy. *Trends Cell Biol.* **1999**, *9*, 66–69, doi:10.1016/S0962-8924(98)01432-9.
115. Boustany, N.N.; Thakor, N. V. Light Scattering Spectroscopy and Imaging of Cellular and Subcellular Events. *Biomed. Photonics Handbook, Second Ed. Fundam. Devices, Tech.* **2014**, 461–488, doi:10.1201/b17290.
116. Denk, W.; Strickler, J.; Webb, W. Two-Photon Laser Scanning Fluorescence Microscopy. *Science (80-.).* **1990**, *248*, 73–76, doi:10.1126/science.2321027.
117. Guo, Y.; Ho, P.P.; Liu, F.; Wang, Q.Z.; Alfano, R.R. Noninvasive Two-Photon-Excitation Imaging of Tryptophan Distribution in Highly Scattering Biological Tissues. *Opt. Commun.* **1998**, *154*, 383–389, doi:10.1016/S0030-4018(98)00207-7.
118. Berezin, M.Y.; Zhan, C.; Lee, H.; Joo, C.; Akers, W.J.; Yazdanfar, S.; Achilefu, S. Two-Photon Optical Properties of Near-Infrared Dyes at 1.55 Mm Excitation. *J. Phys. Chem. B* **2011**, *115*, 11530–11535, doi:10.1021/jp207618e.
119. Pu, Y.; Wang, W.; Yang, Y.; Alfano, R.R. Native Fluorescence Spectra of Human Cancerous and Normal Breast Tissues Analyzed with Non-Negative Constraint Methods. *Appl. Opt.* **2013**, *52*, 1293–1301, doi:10.1364/AO.52.001293.
120. Pu, Y.; Shi, L.; Pratavieira, S.; Alfano, R.R. Two-Photon Excitation Microscopy Using the Second Singlet State of Fluorescent Agents within the “Tissue Optical Window.” *J. Appl. Phys.* **2013**, *114*, 153102, doi:10.1063/1.4825319.
121. Yaseen, M.A.; Yu, J.; Jung, B.; Wong, M.S.; Anvari, B. Biodistribution of Encapsulated Indocyanine Green in Healthy Mice. *Mol. Pharm.* **2009**, *6*, 1321–1332, doi:10.1021/mp800270t.
122. Han, Y.; Kankala, R.K. Leveraging Engineering of Indocyanine Green-Encapsulated Polymeric Nanocomposites for Biomedical Applications., doi:10.3390/nano8060360.
123. Shi, J.; Votruba, A.R.; Farokhzad, O.C.; Langer, R. Nanotechnology in Drug Delivery and Tissue Engineering: From Discovery to Applications. *Nano Lett.*

- 2010**, *10*, 3223–3230, doi:10.1021/nl102184c.
124. Dai, Q.; Ren, E.; Xu, D.; Zeng, Y.; Chen, C.; Liu, G. Indocyanine Green-Based Nanodrugs: A Portfolio Strategy for Precision Medicine. *Prog. Nat. Sci. Mater. Int.* **2020**, *30*, 577–588, doi:10.1016/j.pnsc.2020.08.002.
125. Sevieri, M.; Silva, F.; Bonizzi, A.; Sitia, L.; Truffi, M.; Mazzucchelli, S.; Corsi, F. Indocyanine Green Nanoparticles: Are They Compelling for Cancer Treatment? *Front. Chem.* **2020**, *8*, 1–9, doi:10.3389/fchem.2020.00535.
126. Xu, P.-Y.; Zheng, X.; Kankala, R.K.; Wang, S.-B.; Chen, A.-Z. Advances in Indocyanine Green-Based Codelivery Nanoplatforms for Combinatorial Therapy. *ACS Biomater. Sci. Eng.* **2021**, *7*, 939–962, doi:10.1021/acsbiomaterials.0c01644.
127. Russin, T.J.; Kaiser, J.M.; Barth, B.M.; Eklund, P.C.; Kester, M.; Adair, J.H. Near-Infrared Emitting Fluorophore- Doped Calcium Phosphate Nanoparticles for In Vivo Imaging of Human Breast Cancer. *ACS Nano* **2008**, *2*, 2075–2084.
128. Jiang, C.; Cheng, H.; Yuan, A.; Tang, X.; Wu, J.; Hu, Y. Hydrophobic IR780 Encapsulated in Biodegradable Human Serum Albumin Nanoparticles for Photothermal and Photodynamic Therapy. *Acta Biomater.* **2015**, *14*, 61–69, doi:10.1016/j.actbio.2014.11.041.
129. Pokhrel, S.; Nel, A.E.; Mädler, L. Custom-Designed Nanomaterial Libraries for Testing Metal Oxide Toxicity. *Acc. Chem. Res.* **2013**, *46*, 632–641, doi:10.1021/ar300032q.
130. Hong, S.; Choi, D.W.; Kim, H.N.; Park, C.G.; Lee, W.; Park, H.H. Protein-Based Nanoparticles as Drug Delivery Systems. *Pharmaceutics* **2020**, *12*, 1–28, doi:10.3390/pharmaceutics12070604.
131. Wang, Y.; Bansal, V.; Zelikin, A.N.; Caruso, F. Templated Synthesis of Single-Component Polymer Capsules and Their Application in Drug Delivery. *Nano Lett.* **2008**, *8*, 1741–1745, doi:10.1021/nl080877c.
132. Ashley, C.E.; Carnes, E.C.; Phillips, G.K.; Durfee, P.N.; Buley, M.D.; Lino, C.A.; Padilla, D.P.; Phillips, B.; Carter, M.B.; Willman, C.L.; et al. Cell-Specific Delivery of Diverse Cargos by Bacteriophage MS2 Virus-like Particles. *ACS Nano* **2011**, *5*, 5729–5745, doi:10.1021/nn201397z.

133. Maruyama, K. Intracellular Targeting Delivery of Liposomal Drugs to Solid Tumors Based on EPR Effects. *Adv. Drug Deliv. Rev.* **2011**, *63*, 161–169, doi:10.1016/j.addr.2010.09.003.
134. Sabu, C.; Rejo, C.; Kotta, S.; Pramod, K. *Bioinspired and Biomimetic Systems for Advanced Drug and Gene Delivery*; Elsevier B.V, 2018; Vol. 287; ISBN 0000000286893.
135. Li, R.; He, Y.; Zhang, S.; Qin, J.; Wang, J. Cell Membrane-Based Nanoparticles: A New Biomimetic Platform for Tumor Diagnosis and Treatment. *Acta Pharm. Sin. B* **2018**, *8*, 14–22, doi:10.1016/j.apsb.2017.11.009.
136. Nilapwar, S.M.; Nardelli, M.; Westerhoff, H. V.; Verma, M. *Absorption Spectroscopy*; 1st ed.; Elsevier Inc., 2011; Vol. 500; ISBN 9780123851185.
137. Swinehart, D.F. The Beer-Lambert Law. *J. Chem. Educ.* **1962**, *39*, 333–335, doi:10.1021/ed039p333.
138. Lohman, F.H. The Mathematical Combination of Lambert's Law and Beer's Law. *J. Chem. Educ.* 1955, *32*, 155.
139. Senesi, N.; D'Orazio, V. Fluorescence Spectroscopy. *Encycl. Soils Environ.* **2004**, *4*, 35–52, doi:10.1016/B0-12-348530-4/00211-3.
140. Michael, K. Characterization of Electronic Transitions in Complex Molecules. *Discuss. Faraday Soc.* **1950**, *9*, 14–19.
141. Stetefeld, J.; McKenna, S.A.; Patel, T.R. Dynamic Light Scattering: A Practical Guide and Applications in Biomedical Sciences. *Biophys. Rev.* **2016**, *8*, 409–427, doi:10.1007/s12551-016-0218-6.
142. Singh, A.K. *Experimental Methodologies for the Characterization of Nanoparticles*; 2016; ISBN 9780128014066.
143. Kowoll, T.; Müller, E.; Fritsch-Decker, S.; Hettler, S.; Störmer, H.; Weiss, C.; Gerthsen, D. Contrast of Backscattered Electron SEM Images of Nanoparticles on Substrates with Complex Structure. *Scanning* **2017**, *2017*, doi:10.1155/2017/4907457.
144. Tizro, P.; Choi, C.; Khanlou, N. Sample Preparation for Transmission Electron Microscopy. *Methods Mol. Biol.* **2019**, *1897*, 417–424, doi:10.1007/978-1-4939-8935-5_33.

145. Lichtman, J.W.; Conchello, J.A. Fluorescence Microscopy. *Nat. Methods* **2005**, *2*, 910–919, doi:10.1038/nmeth817.
146. Dunn, K.W.; Young, P.A. Principles of Multiphoton Microscopy. *Nephron - Exp. Nephrol.* **2006**, *103*, 33–40, doi:10.1159/000090614.
147. Young, M.D.; Field, J.J.; Sheetz, K.E.; Bartels, R.A.; Squier, J. A Pragmatic Guide to Multiphoton Microscope Design. *Adv. Opt. Photonics* **2015**, *7*, 276, doi:10.1364/AOP.7.000276.
148. Walker, J.M. *P53 Protocols - IN MOLECULAR BIOLOGY™ Series Editor*; 2009; Vol. 531; ISBN 9781627032384.
149. Dulbecco, R. Production of Plaques in Monolayer Tissue Cultures by Single Particles of an Animal Virus. *Proc. Natl. Acad. Sci.* **1952**, *38*, 747–752, doi:10.1073/pnas.38.8.747.
150. Präbst, K.; Engelhardt, H.; Ringgeler, S.; Hübner, H. Basic Colorimetric Proliferation Assays: MTT, WST, and Resazurin. *Methods Mol. Biol.* **2017**, *1601*, 1–17, doi:10.1007/978-1-4939-6960-9_1.
151. Zhao, Y.; Van Rooy, I.; Hak, S.; Fay, F.; Tang, J.; Davies, C.D.L.; Skobe, M.; Fisher, E.A.; Radu, A.; Fayad, Z.A.; et al. Near-Infrared Fluorescence Energy Transfer Imaging of Nanoparticle Accumulation and Dissociation Kinetics in Tumor-Bearing Mice. *ACS Nano* **2013**, *7*, 10362–10370, doi:10.1021/nn404782p.
152. Smith, A.M.; Mancini, M.C.; Nie, S. Bioimaging: Second Window for in Vivo Imaging. *Nat. Nanotechnol.* **2009**, *4*, 710–711, doi:10.1038/nnano.2009.326.
153. Hill, T.K.; Abdulahad, A.; Kelkar, S.S.; Marini, F.C.; Long, T.E.; Provenzale, J.M.; Mohs, A.M. Indocyanine Green-Loaded Nanoparticles for Image-Guided Tumor Surgery. *Bioconjug. Chem.* **2015**, *26*, 294–303, doi:10.1021/bc5005679.
154. Zheng, X.; Zhou, F.; Wu, B.; Chen, W.R.; Xing, D. Enhanced Tumor Treatment Using Biofunctional Indocyanine Green-Containing Nanostructure by Intratumoral or Intravenous Injection. *Mol. Pharm.* **2012**, *9*, 514–522, doi:10.1021/mp200526m.
155. Yoneya, S.; Saito, T.; Komatsu, Y.; Koyama, I.; Takahashi, K.; Duvoll-Young, J. Binding Properties of Indocyanine Green in Human Blood. *Investig.*

- Ophthalmol. Vis. Sci.* **1998**, *39*, 1286–1290.
156. Tan, X.; Wang, J.; Pang, X.; Liu, L.; Sun, Q.; You, Q.; Tan, F.; Li, N. Indocyanine Green-Loaded Silver Nanoparticle@Polyaniline Core/Shell Theranostic Nanocomposites for Photoacoustic/Near-Infrared Fluorescence Imaging-Guided and Single-Light-Triggered Photothermal and Photodynamic Therapy. *ACS Appl. Mater. Interfaces* **2016**, *8*, 34991–35003, doi:10.1021/acsami.6b11262.
 157. Li, W.; Zhang, H.; Guo, X.; Wang, Z.; Kong, F.; Luo, L.; Li, Q.; Zhu, C.; Yang, J.; Lou, Y.; et al. Gold Nanospheres-Stabilized Indocyanine Green as a Synchronous Photodynamic-Photothermal Therapy Platform That Inhibits Tumor Growth and Metastasis. *ACS Appl. Mater. Interfaces* **2017**, *9*, 3354–3367, doi:10.1021/acsami.6b13351.
 158. Miranda, D.; Wan, C.; Kilian, H.I.; Mabrouk, M.T.; Zhou, Y.; Jin, H.; Lovell, J.F. Indocyanine Green Binds to DOTAP Liposomes for Enhanced Optical Properties and Tumor Photoablation. *Biomater. Sci.* **2019**, *7*, 3158–3164, doi:10.1039/c9bm00551j.
 159. Bar-David, S.; Larush, L.; Goder, N.; Aizic, A.; Zigmond, E.; Varol, C.; Klausner, J.; Magdassi, S.; Nizri, E. Size and Lipid Modification Determine Liposomal Indocyanine Green Performance for Tumor Imaging in a Model of Rectal Cancer. *Sci. Rep.* **2019**, *9*, 1–8, doi:10.1038/s41598-019-45038-w.
 160. Ege, Z.R.; Akan, A.; Oktar, F.N.; Lin, C.C.; Kuruca, D.S.; Karademir, B.; Sahin, Y.M.; Erdemir, G.; Gunduz, O. Indocyanine Green Based Fluorescent Polymeric Nanoprobes for in Vitro Imaging. *J. Biomed. Mater. Res. - Part B Appl. Biomater.* **2020**, *108*, 538–554, doi:10.1002/jbm.b.34410.
 161. Sitia, L.; Sevieri, M.; Bonizzi, A.; Allevi, R.; Morasso, C.; Foschi, D.; Corsi, F.; Mazzucchelli, S. Development of Tumor-Targeted Indocyanine Green-Loaded Ferritin Nanoparticles for Intraoperative Detection of Cancers. *ACS Omega* **2020**, *5*, 12035–12045, doi:10.1021/acsomega.0c00244.
 162. Kumar, G.P.; Rajeshwarrao, P. Nonionic Surfactant Vesicular Systems for Effective Drug Delivery—an Overview. *Acta Pharm. Sin. B* **2011**, *1*, 208–219, doi:10.1016/j.apsb.2011.09.002.

163. Gao, M.; Du, N.; Yao, Z.; Li, Y.; Chen, N.; Hou, W. Vesicle Formation of Single-Chain Amphiphilic 4-Dodecylbenzene Sulfonic Acid in Water and Micelle-to-Vesicle Transition Induced by Wet–Dry Cycles. *Soft Matter* **2021**, 2490–2499, doi:10.1039/d0sm02229b.
164. Arshad, M.; Pradhan, R.A.; Zubair, M.; Ullah, A. *Lipid-Derived Renewable Amphiphilic Nanocarriers for Drug Delivery, Biopolymer-Based Formulations: Biomedical and Food Applications*; Elsevier Inc., 2020; ISBN 9780128168981.
165. Akbarzadeh, A.; Rezaei-sadabady, R.; Davaran, S.; Joo, S.W.; Zarghami, N. Liposome: Classification, Preparation, New Aspects of Liposome Formation, and Applications. *Nanoscale Res. Lett.* **2013**, 8, 1–9.
166. Bartelds, R.; Nematollahi, M.H.; Pols, T.; Stuart, M.C.A.; Pardakhty, A.; Asadikaram, G.; Poolman, B. Niosomes, an Alternative for Liposomal Delivery. *PLoS One* **2018**, 13, 1–18, doi:10.1371/journal.pone.0194179.
167. Alonso, L.; Roque, L.; Escudero, I.; Benito, J.M.; Sanz, M.T.; Beltrán, S. Solubilization of Span 80 Niosomes by Sodium Dodecyl Sulfate. *ACS Sustain. Chem. Eng.* **2016**, 4, 1862–1869, doi:10.1021/acssuschemeng.6b00148.
168. Moghassemi, S.; Hadjizadeh, A. Nano-Niosomes as Nanoscale Drug Delivery Systems: An Illustrated Review. *J. Control. Release* **2014**, 185, 22–36, doi:10.1016/j.jconrel.2014.04.015.
169. Davarpanah, F.; Khalili Yazdi, A.; Barani, M.; Mirzaei, M.; Torkzadeh-Mahani, M. Magnetic Delivery of Antitumor Carboplatin by Using PEGylated-Niosomes. *DARU, J. Pharm. Sci.* **2018**, 26, 57–64, doi:10.1007/s40199-018-0215-3.
170. Muzzalupo, R.; Trombino, S.; Iemma, F.; Puoci, F.; La Mesa, C.; Picci, N. Preparation and Characterization of Bolaform Surfactant Vesicles. *Colloids Surfaces B Biointerfaces* **2005**, 46, 78–83, doi:10.1016/j.colsurfb.2005.09.003.
171. Crook, K.; Stevenson, B.J.; Dubouchet, M.; Porteous, D.J. Inclusion of Cholesterol in DOTAP Transfection Complexes Increases the Delivery of DNA to Cells in Vitro in the Presence of Serum. *Gene Ther.* **1998**, 5, 137–143, doi:10.1038/sj.gt.3300554.

172. Nematollahi, M.H.; Pardakhty, A.; Torkzadeh-Mahanai, M.; Mehrabani, M.; Asadikaram, G. Changes in Physical and Chemical Properties of Niosome Membrane Induced by Cholesterol: A Promising Approach for Niosome Bilayer Intervention. *RSC Adv.* **2017**, *7*, 49463–49472, doi:10.1039/c7ra07834j.
173. Demir, B.; Barlas, F.B.; Gumus, Z.P.; Unak, P.; Timur, S. Theranostic Niosomes as a Promising Tool for Combined Therapy and Diagnosis: “All-in-One” Approach. *ACS Appl. Nano Mater.* **2018**, *1*, 2827–2835, doi:10.1021/acsanm.8b00468.
174. Manosroi, A.; Jantrawut, P.; Akazawa, H.; Akihisa, T.; Manosroi, W.; Manosroi, J. Transdermal Absorption Enhancement of Gel Containing Elastic Niosomes Loaded with Gallic Acid from Terminalia Chebula Galls. *Pharm. Biol.* **2011**, *49*, 553–562, doi:10.3109/13880209.2010.528432.
175. Ribier, A.; Abstracts, C.; Kight, P.E. 4830857 Cosmetic and Pharmaceutical Compositions Containing Niosomes and a Water-Soluble Polyamide, and a Process for Preparing These Compositions. *Gen. Pharmacol. Vasc. Syst.* **1990**, *21*, iii, doi:10.1016/0306-3623(90)90667-b.
176. Xu, Y.Q.; Chen, W.R.; Tsosie, J.K.; Xie, X.; Li, P.; Wan, J.B.; He, C.W.; Chen, M.W. Niosome Encapsulation of Curcumin: Characterization and Cytotoxic Effect on Ovarian Cancer Cells. *J. Nanomater.* **2016**, *2016*, doi:10.1155/2016/6365295.
177. Al Qtaish, N.; Gallego, I.; Villate-Beitia, I.; Sainz-Ramos, M.; López-Méndez, T.B.; Grijalvo, S.; Eritja, R.; Soto-Sánchez, C.; Martínez-Navarrete, G.; Fernández, E.; et al. Niosome-Based Approach for in Situ Gene Delivery to Retina and Brain Cortex as Immune-Privileged Tissues. *Pharmaceutics* **2020**, *12*, 1–29, doi:10.3390/pharmaceutics12030198.
178. Seleci, D.A.; Seleci, M.; Jochums, A.; Walter, J.G.; Stahl, F.; Scheper, T. Aptamer Mediated Niosomal Drug Delivery. *RSC Adv.* **2016**, *6*, 87910–87918, doi:10.1039/c6ra19525c.
179. Lemoine, C.; Thakur, A.; Krajišnik, D.; Guyon, R.; Longet, S.; Razim, A.; Górska, S.; Pantelić, I.; Ilić, T.; Nikolić, I.; et al. Technological Approaches for

- Improving Vaccination Compliance and Coverage. *Vaccines* **2020**, *8*, 1–29, doi:10.3390/vaccines8020304.
180. Yang, C.; Gao, S.; Song, P.; Dagnæs-Hansen, F.; Jakobsen, M.; Kjems, J. Theranostic Niosomes for Efficient SiRNA/MicroRNA Delivery and Activatable Near-Infrared Fluorescent Tracking of Stem Cells. *ACS Appl. Mater. Interfaces* **2018**, *10*, 19494–19503, doi:10.1021/acsami.8b05513.
181. Niu, C.; Xu, Y.; An, S.; Zhang, M.; Hu, Y.; Wang, L.; Peng, Q. Near-Infrared Induced Phase-Shifted ICG/Fe₃O₄ Loaded PLGA Nanoparticles for Photothermal Tumor Ablation. *Sci. Rep.* **2017**, *7*, 1–10, doi:10.1038/s41598-017-06122-1.
182. Rotermund, F.; Weigand, R.; Penzkofer, A. J-Aggregation and Disaggregation of Indocyanine Green in Water. *Chem. Phys.* **1997**, *220*, 385–392, doi:10.1016/S0301-0104(97)00151-1.
183. Liu, R.; Tang, J.; Xu, Y.; Zhou, Y.; Dai, Z. Nano-Sized Indocyanine Green j-Aggregate as a One-Component Theranostic Agent. *Nanotheranostics* **2017**, *1*, 430–439, doi:10.7150/ntno.19935.
184. Devoisselle, J.-M.; Soulie-Begu, S.; Mordon, S.R.; Desmettre, T.; Maillols, H. <title>Fluorescence Properties of Indocyanin Green: I. In-Vitro Study with Micelles and Liposomes</Title>; Thompson, R.B., Ed.; May 7 1997; Vol. 2980, pp. 453–460.
185. Desmettre, T.; Devoisselle, J.M.; Mordon, S. Fluorescence Properties and Metabolic Features of Indocyanine Green (ICG) as Related to Angiography. *Surv. Ophthalmol.* **2000**, *45*, 15–27, doi:10.1016/S0039-6257(00)00123-5.
186. Sevick-Muraca, E.M.; Lopez, G.; Reynolds, J.S.; Troy, T.L.; Hutchinson, C.L. Fluorescence and Absorption Contrast Mechanisms for Biomedical Optical Imaging Using Frequency-Domain Techniques. *Photochem. Photobiol.* **1997**, *66*, 55–64, doi:10.1111/j.1751-1097.1997.tb03138.x.
187. Philip, R.; Penzkofer, A.; Bäuml, W.; Szeimies, R.M.; Abels, C. Absorption and Fluorescence Spectroscopic Investigation of Indocyanine Green. *J. Photochem. Photobiol. A Chem.* **1996**, *96*, 137–148, doi:10.1016/1010-6030(95)04292-X.

188. Mindt, S.; Karampinis, I.; John, M.; Neumaier, M.; Nowak, K. Stability and Degradation of Indocyanine Green in Plasma, Aqueous Solution and Whole Blood. *Photochem. Photobiol. Sci.* **2018**, *17*, 1189–1196, doi:10.1039/c8pp00064f.
189. Wolfbeis, O.S. An Overview of Nanoparticles Commonly Used in Fluorescent Bioimaging. *Chem. Soc. Rev.* **2015**, *44*, 4743–4768, doi:10.1039/c4cs00392f.
190. Sharker, S.M.; Lee, J.E.; Kim, S.H.; Jeong, J.H.; In, I.; Lee, H.; Park, S.Y. PH Triggered in Vivo Photothermal Therapy and Fluorescence Nanoplatform of Cancer Based on Responsive Polymer-Indocyanine Green Integrated Reduced Graphene Oxide. *Biomaterials* **2015**, *61*, 229–238, doi:10.1016/j.biomaterials.2015.05.040.
191. Meng, H.; Mai, W.X.; Zhang, H.; Xue, M.; Xia, T.; Lin, S.; Wang, X.; Zhao, Y.; Ji, Z.; Zink, J.I.; et al. Codelivery of an Optimal Drug/SiRNA Combination Using Mesoporous Silica Nanoparticles to Overcome Drug Resistance in Breast Cancer in Vitro and in Vivo. *ACS Nano* **2013**, *7*, 994–1005, doi:10.1021/nm3044066.
192. Tam, F.; Goodrich, G.P.; Johnson, B.R.; Halas, N.J. Plasmonic Enhancement of Molecular Fluorescence. *Nano Lett.* **2007**, *7*, 496–501, doi:10.1021/nl062901x.
193. Malicka, J.; Gryczynski, I.; Geddes, C.D.; Lakowicz, J.R. Metal-Enhanced Emission from Indocyanine Green: A New Approach to in Vivo Imaging. *J. Biomed. Opt.* **2003**, *8*, 472, doi:10.1117/1.1578643.
194. Saxena, V.; Sadoqi, M.; Shao, J. Polymeric Nanoparticulate Delivery System for Indocyanine Green: Biodistribution in Healthy Mice. *Int. J. Pharm.* **2006**, *308*, 200–204, doi:10.1016/j.ijpharm.2005.11.003.
195. Kłyszczko, C.; Bazalak, D.; Sypniewski, J. [Evaluation of the Management of Cervical Cancer of Grade O with Consideration of Simple Hysterectomy. II]. *Ginekol. Pol.* **1979**, *Suppl*, 227–228, doi:10.1155/2012/548389.
196. Buzea, C.; Pacheco, I.I.; Robbie, K. Nanomaterials and Nanoparticles: Sources and Toxicity. *Biointerphases* **2007**, *2*, MR17-71, doi:10.1116/1.2815690.
197. Hoet, P.H.M.; Brüske-Hohlfeld, I.; Salata, O. V. Nanoparticles - Known and

- Unknown Health Risks. *J. Nanobiotechnology* **2004**, 2, 12, doi:10.1186/1477-3155-2-12.
198. Qin, Y.T.; Feng, Y.S.; Ma, Y.J.; He, X.W.; Li, W.Y.; Zhang, Y.K.; Zhang, Y.K. Tumor-Sensitive Biodegradable Nanoparticles of Molecularly Imprinted Polymer-Stabilized Fluorescent Zeolitic Imidazolate Framework-8 for Targeted Imaging and Drug Delivery. *ACS Appl. Mater. Interfaces* **2020**, 12, 24585–24598, doi:10.1021/acsami.0c05154.
199. Far, J.; Abdel-Haq, M.; Gruber, M.; Abu Ammar, A. Developing Biodegradable Nanoparticles Loaded with Mometasone Furoate for Potential Nasal Drug Delivery. *ACS Omega* **2020**, 5, 7432–7439, doi:10.1021/acsomega.0c00111.
200. Kydd, J.; Jadia, R.; Velpurisiva, P.; Gad, A.; Paliwal, S.; Rai, P. Targeting Strategies for the Combination Treatment of Cancer Using Drug Delivery Systems. *Pharmaceutics* **2017**, 9, 46, doi:10.3390/pharmaceutics9040046.
201. Zhu, S.; Huang, A.-G.; Luo, F.; Li, J.; Li, J.; Zhu, L.; Zhao, L.; Zhu, B.; Ling, F.; Wang, G.-X. Application of Virus Targeting Nanocarrier Drug Delivery System in Virus-Induced Central Nervous System Disease Treatment. *ACS Appl. Mater. Interfaces* **2019**, 11, 19006–19016, doi:10.1021/acsami.9b06365.
202. Wen, A.M.; Steinmetz, N.F. Design of Virus-Based Nanomaterials for Medicine, Biotechnology, and Energy. *Chem. Soc. Rev.* **2016**, 45, 4074–4126, doi:10.1039/C5CS00287G.
203. Cheng, F.; Mukhopadhyay, S. Generating Enveloped Virus-like Particles with in Vitro Assembled Cores. *Virology* **2011**, 413, 153–160, doi:10.1016/j.virol.2011.02.001.
204. Akita, H.; Kudo, A.; Minoura, A.; Yamaguti, M.; Khalil, I.A.; Moriguchi, R.; Masuda, T.; Danev, R.; Nagayama, K.; Kogure, K.; et al. Multi-Layered Nanoparticles for Penetrating the Endosome and Nuclear Membrane via a Step-Wise Membrane Fusion Process. *Biomaterials* **2009**, 30, 2940–2949, doi:10.1016/j.biomaterials.2009.02.009.
205. Dimitrov, D.S. Virus Entry: Molecular Mechanisms and Biomedical Applications. *Nat. Rev. Microbiol.* **2004**, 2, 109–122, doi:10.1038/nrmicro817.
206. Rohovie, M.J.; Nagasawa, M.; Swartz, J.R. Virus-like Particles: Next-

- Generation Nanoparticles for Targeted Therapeutic Delivery. *Bioeng. Transl. Med.* **2017**, *2*, 43–57, doi:10.1002/btm2.10049.
207. Tagit, O.; De Ruiter, M. V.; Brasch, M.; Ma, Y.; Cornelissen, J.J.L.M. Quantum Dot Encapsulation in Virus-like Particles with Tuneable Structural Properties and Low Toxicity. *RSC Adv.* **2017**, *7*, 38110–38118, doi:10.1039/c7ra06684h.
208. Zhang, W.; Xu, C.; Yin, G.Q.; Zhang, X.E.; Wang, Q.; Li, F. Encapsulation of Inorganic Nanomaterials inside Virus-Based Nanoparticles for Bioimaging. *Nanotheranostics* **2017**, *1*, 358–368, doi:10.7150/ntno.21384.
209. van der Goot, F.G.; Gruenberg, J. Intra-Endosomal Membrane Traffic. *Trends Cell Biol.* **2006**, *16*, 514–521, doi:10.1016/j.tcb.2006.08.003.
210. Mothes, W.; Boerger, A.L.; Narayan, S.; Cunningham, J.M.; Young, J.A.T. Retroviral Entry Mediated by Receptor Priming and Low PH Triggering of an Envelope Glycoprotein. *Cell* **2000**, *103*, 679–689, doi:10.1016/S0092-8674(00)00170-7.
211. Flexman, J.A.; Cross, D.J.; Lewellen, B.L.; Miyoshi, S.; Kim, Y.; Minoshima, S. Magnetically Targeted Viral Envelopes: A PET Investigation of Initial Biodistribution. *IEEE Trans. Nanobioscience* **2008**, *7*, 223–232, doi:10.1109/TNB.2008.2002288.
212. Flexman, J.A.; Minoshima, S.; Kim, Y.; Miyoshi, S.; Lewellen, B.L.; Cross, D.J. A Viral Envelope as a Vehicle for Tracer, Drug, and Gene Delivery. *IEEE Eng. Med. Biol. Mag.* **2006**, *25*, 70–75, doi:10.1109/MEMB.2006.1657790.
213. Miyoshi, S.; Flexman, J.A.; Cross, D.J.; Maravilla, K.R.; Kim, Y.; Anzai, Y.; Oshima, J.; Minoshima, S. Transfection of Neuroprogenitor Cells with Iron Nanoparticles for Magnetic Resonance Imaging Tracking: Cell Viability, Differentiation, and Intracellular Localization. *Mol. Imaging Biol.* **2005**, *7*, 286–295, doi:10.1007/s11307-005-0008-1.
214. Ogino, T.; Green, T.J. RNA Synthesis and Capping by Nonsegmented Negative Strand RNA Viral Polymerases: Lessons from a Prototypic Virus. *Front. Microbiol.* **2019**, *10*, 1–28, doi:10.3389/fmicb.2019.01490.
215. Bishnoi, S.; Tiwari, R.; Gupta, S.; Byraredy, S.; Nayak, D. Oncotargeting by Vesicular Stomatitis Virus (VSV): Advances in Cancer Therapy. *Viruses* **2018**,

- 10, 90, doi:10.3390/v10020090.
216. Lin, H.; Zheng, D.; Li, Y.; Wang, N.; Chen, S.; Fu, Y.; Xu, W.; Wei, C. Incorporation of VSV-G Produces Fusogenic Plasma Membrane Vesicles Capable of Efficient Transfer of Bioactive Macromolecules and Mitochondria. *Biomed. Microdevices* **2016**, *18*, 41, doi:10.1007/s10544-016-0066-y.
217. Blumenthal, R.; Bali-Puri, A.; Walter, A.; Covell, D.; Eidelman, O. PH-Dependent Fusion of Vesicular Stomatitis Virus with Vero Cells. Measurement by Dequenching of Octadecyl Rhodamine Fluorescence. *J. Biol. Chem.* **1987**, *262*, 13614–13619.
218. Eslahi, N.K.; Muller, S.; Nguyen, L.; Wilson, E.; Thull, N.; Rolland, A.; Pericle, F. Fusogenic Activity of Vesicular Stomatitis Virus Glycoprotein Plasmid in Tumors as an Enhancer of IL-12 Gene Therapy. *Cancer Gene Ther.* **2001**, *8*, 55–62, doi:10.1038/sj.cgt.7700270.
219. Mangeot, P.-E.; Dollet, S.; Girard, M.; Ciancia, C.; Joly, S.; Peschanski, M.; Lotteau, V. Protein Transfer into Human Cells by VSV-G-Induced Nanovesicles. *Mol. Ther.* **2011**, *19*, 1656–1666, doi:10.1038/mt.2011.138.
220. Wang, L.; Zheng, J.; Yang, S.; Wu, C.; Liu, C.; Xiao, Y.; Li, Y.; Qing, Z.; Yang, R. Two-Photon Sensing and Imaging of Endogenous Biological Cyanide in Plant Tissues Using Graphene Quantum Dot/Gold Nanoparticle Conjugate. *ACS Appl. Mater. Interfaces* **2015**, *7*, 19509–19515, doi:10.1021/acsami.5b06352.
221. Abe, A.; Miyahara, A.; Friedmann, T. Enhanced Gene Transfer with Fusogenic Liposomes Containing Vesicular Stomatitis Virus G Glycoprotein. *J. Virol.* **1998**, *72*, 6159–6163, doi:10.1128/JVI.72.7.6159-6163.1998.
222. Zhitnyuk, Y.; Gee, P.; Lung, M.S.Y.; Sasakawa, N.; Xu, H.; Saito, H.; Hotta, A. Biochemical and Biophysical Research Communications Efficient MRNA Delivery System Utilizing Chimeric VSVG-L7Ae Virus-like Particles. *Biochem. Biophys. Res. Commun.* **2018**, 1–6, doi:10.1016/j.bbrc.2018.09.113.
223. Kaczmarczyk, S.J.; Sitaraman, K.; Young, H.A.; Hughes, S.H.; Chatterjee, D.K. Protein Delivery Using Engineered Virus-like Particles. *Proc. Natl. Acad. Sci. U. S. A.* **2011**, *108*, 16998–17003, doi:10.1073/pnas.1101874108.

224. Miyanohara, A. Preparation of Vesicular Stomatitis Virus-G (VSV-G) Conjugate and Its Use in Gene Transfer. *Cold Spring Harb. Protoc.* **2012**, *7*, 453–456, doi:10.1101/pdb.prot068528.
225. Hilderbrand, S.A.; Weissleder, R. Near-Infrared Fluorescence: Application to in Vivo Molecular Imaging. *Curr. Opin. Chem. Biol.* **2010**, *14*, 71–79, doi:10.1016/j.cbpa.2009.09.029.
226. Kumari, A.; Kumari, K.; Gupta, S. Protease Responsive Essential Amino-Acid Based Nanocarriers for Near-Infrared Imaging. *Sci. Rep.* **2019**, *9*, 1–12, doi:10.1038/s41598-019-56871-4.
227. Weissleder, R. A Clearer Vision for in Vivo Imaging. *Nat. Biotechnol.* **2001**, *19*, 316–317, doi:10.1038/86684.
228. Owens, E.A.; Lee, S.; Choi, J.; Henary, M.; Choi, H.S. NIR Fluorescent Small Molecules for Intraoperative Imaging. *Wiley Interdiscip. Rev. Nanomedicine Nanobiotechnology* **2015**, *7*, 828–838, doi:10.1002/wnan.1337.
229. Carr, J.A.; Aellen, M.; Franke, D.; So, P.T.C.; Bruns, O.T.; Bawendi, M.G. Absorption by Water Increases Fluorescence Image Contrast of Biological Tissue in the Shortwave Infrared. *Proc. Natl. Acad. Sci. U. S. A.* **2018**, *115*, 9080–9085, doi:10.1073/pnas.1803210115.
230. Kumari, A.; Kumari, K.; Gupta, S. The Effect of Nanoencapsulation of ICG on Two-Photon Bioimaging. *RSC Adv.* **2019**, *9*, 18703–18712, doi:10.1039/c9ra03152a.
231. Resch-Genger, U.; Grabolle, M.; Cavaliere-Jaricot, S.; Nitschke, R.; Nann, T. Quantum Dots versus Organic Dyes as Fluorescent Labels. *Nat. Methods* **2008**, *5*, 763–775, doi:10.1038/nmeth.1248.
232. WHEELER, H.O.; CRANSTON, W.I.; MELTZER, J.I. Hepatic Uptake and Biliary Excretion of Indocyanine Green in the Dog. *Proc. Soc. Exp. Biol. Med.* **1958**, *99*, 11–14, doi:10.3181/00379727-99-24229.
233. Benson, R.C.; Kues, H.A. Fluorescence Properties of Indocyanine Green as Related to Angiography. *Phys. Med. Biol.* **1978**, *23*, 017, doi:10.1088/0031-9155/23/1/017.
234. Rodriguez, V.B.; Henry, S.M.; Hoffman, A.S.; Stayton, P.S.; Li, X.; Pun, S.H.

- Encapsulation and Stabilization of Indocyanine Green within Poly(Styrene-Alt-Maleic Anhydride) Block-Poly(Styrene) Micelles for near-Infrared Imaging. *J. Biomed. Opt.* **2008**, *13*, 014025, doi:10.1117/1.2834296.
235. Jung, B.; Rao, A.L.N.; Anvari, B. Optical Nano-Constructs Composed of Genome-Depleted Brome Mosaic Virus Doped with a near Infrared Chromophore for Potential Biomedical Applications. *ACS Nano* **2011**, *5*, 1243–1252, doi:10.1021/nn1028696.
236. Zhao, P.; Zheng, M.; Yue, C.; Luo, Z.; Gong, P.; Gao, G.; Sheng, Z.; Zheng, C.; Cai, L. Improving Drug Accumulation and Photothermal Efficacy in Tumor Depending on Size of ICG Loaded Lipid-Polymer Nanoparticles. *Biomaterials* **2014**, *35*, 6037–6046, doi:10.1016/j.biomaterials.2014.04.019.
237. Saxena, V.; Sadoqi, M.; Shao, J. Enhanced Photo-Stability, Thermal-Stability and Aqueous-Stability of Indocyanine Green in Polymeric Nanoparticulate Systems. *J. Photochem. Photobiol. B Biol.* **2004**, *74*, 29–38, doi:10.1016/j.jphotobiol.2004.01.002.
238. Nayak, D.; Panda, D.; Das, S.C.; Luo, M.; Pattnaik, A.K. Single-Amino-Acid Alterations in a Highly Conserved Central Region of Vesicular Stomatitis Virus N Protein Differentially Affect the Viral Nucleocapsid Template Functions. *J. Virol.* **2009**, *83*, 5525–5534, doi:10.1128/jvi.02289-08.
239. Farah, M.E.; Maia, M.; Penha, F.M.; Rodrigues, E.B. *The Use of Vital Dyes during Vitreoretinal Surgery – Chromovitrectomy*; First Edit.; © 2010, Elsevier Inc. All rights reserved., 2010;
240. Farah, M.E.; Maia, M.; Penha, F.M.; Rodrigues, E.B. The Use of Vital Dyes during Vitreoretinal Surgery-Chromovitrectomy. *Dev. Ophthalmol.* **2015**, *55*, 365–375, doi:10.1159/000438963.
241. Mao, F.; Wu, Y.; Tang, X.; Kang, J.; Zhang, B.; Yan, Y.; Qian, H.; Zhang, X.; Xu, W. Exosomes Derived from Human Umbilical Cord Mesenchymal Stem Cells Relieve Inflammatory Bowel Disease in Mice. *Biomed Res. Int.* **2017**, *2017*, 1–12, doi:10.1155/2017/5356760.
242. Villa, A.; Garofalo, M.; Crescenti, D.; Rizzi, N.; Brunialti, E.; Vingiani, A.; Belotti, P.; Sposito, C.; Franzè, S.; Cilurzo, F.; et al. Transplantation of

- Autologous Extracellular Vesicles for Cancer-Specific Targeting. *Theranostics* **2021**, *11*, 2034–2047, doi:10.7150/thno.51344.
243. Garofalo, M.; Villa, A.; Brunialti, E.; Crescenti, D.; Dell'omo, G.; Kuryk, L.; Vingiani, A.; Mazzaferro, V.; Ciana, P. Cancer-Derived EVs Show Tropism for Tissues at Early Stage of Neoplastic Transformation. *Nanotheranostics* **2021**, *5*, 1–7, doi:10.7150/ntno.47226.
244. Tung, C.H.; Mahmood, U.; Bredow, S.; Weissleder, R. In Vivo Imaging of Proteolytic Enzyme Activity Using a Novel Molecular Reporter. *Cancer Res.* **2000**, *60*, 4953–4958.
245. Yeroslavsky, G.; Umezawa, M.; Okubo, K.; Nigoghossian, K.; Dung, D.T.K.; Kamimura, M.; Soga, K. Photostabilization of Indocyanine Green Dye by Energy Transfer in Phospholipid-Peg Micelles. *J. Photopolym. Sci. Technol.* **2019**, *32*, 115–121, doi:10.2494/photopolymer.32.115.
246. Kima, I.S.; Jenni, S.; Stanifer, M.L.; Roth, E.; Whelan, S.P.J.; Van Oijen, A.M.; Harrison, S.C. Mechanism of Membrane Fusion Induced by Vesicular Stomatitis Virus G Protein. *Proc. Natl. Acad. Sci. U. S. A.* **2017**, *114*, E28–E36, doi:10.1073/pnas.1618883114.
247. Commins, S.P.; Borish, L.; Steinke, J.W. Immunologic Messenger Molecules: Cytokines, Interferons, and Chemokines. *J. Allergy Clin. Immunol.* **2010**, *125*, S53–S72, doi:10.1016/j.jaci.2009.07.008.
248. Yin, Y.; Hu, Q.; Xu, C.; Qiao, Q.; Qin, X.; Song, Q.; Peng, Y.; Zhao, Y.; Zhang, Z. Co-Delivery of Doxorubicin and Interferon- γ by Thermosensitive Nanoparticles for Cancer Immunotherapy. *Mol. Pharm.* **2018**, *15*, 4161–4172, doi:10.1021/acs.molpharmaceut.8b00564.
249. Marrache, S.; Tundup, S.; Harn, D.A.; Dhar, S. Ex Vivo Programming of Dendritic Cells by Mitochondria-Targeted Nanoparticles to Produce Interferon-Gamma for Cancer Immunotherapy. *ACS Nano* **2013**, *7*, 7392–7402, doi:10.1021/nn403158n.
250. Cheng, K.; Chen, H.; Jenkins, C.H.; Zhang, G.; Zhao, W.; Zhang, Z.; Han, F.; Fung, J.; Yang, M.; Jiang, Y.; et al. Synthesis, Characterization, and Biomedical Applications of a Targeted Dual-Modal Near-Infrared-II Fluorescence and

- Photoacoustic Imaging Nanoprobe. *ACS Nano* **2017**, *11*, 12276–12291, doi:10.1021/acsnano.7b05966.
251. Wender, R.C.; Brawley, O.W.; Fedewa, S.A.; Gansler, T.; Smith, R.A. A Blueprint for Cancer Screening and Early Detection: Advancing Screening's Contribution to Cancer Control. *CA. Cancer J. Clin.* **2019**, *69*, 50–79, doi:10.3322/caac.21550.
252. Murfin, L.C.; Weber, M.; Park, S.J.; Kim, W.T.; Lopez-Alled, C.M.; McMullin, C.L.; Pradaux-Caggiano, F.; Lyall, C.L.; Kociok-Köhn, G.; Wenk, J.; et al. Azulene-Derived Fluorescent Probe for Bioimaging: Detection of Reactive Oxygen and Nitrogen Species by Two-Photon Microscopy. *J. Am. Chem. Soc.* **2019**, *141*, 19389–19396, doi:10.1021/jacs.9b09813.
253. Zou, Y.; Li, M.; Xing, Y.; Duan, T.; Zhou, X.; Yu, F. Bioimaging of Glutathione with a Two-Photon Fluorescent Probe and Its Potential Application for Surgery Guide in Laryngeal Cancer. *ACS Sensors* **2020**, *5*, 242–249, doi:10.1021/acssensors.9b02118.
254. Wang, L.; Zheng, J.; Yang, S.; Wu, C.; Liu, C.; Xiao, Y.; Li, Y.; Qing, Z.; Yang, R. Two-Photon Sensing and Imaging of Endogenous Biological Cyanide in Plant Tissues Using Graphene Quantum Dot/Gold Nanoparticle Conjugate. *ACS Appl. Mater. Interfaces* **2015**, *7*, 19509–19515, doi:10.1021/acсами.5b06352.
255. PARTHENOPOULOS, D.A.; RENTZEPIS, P.M. Three-Dimensional Optical Storage Memory. *Science (80-.)*. **1989**, *245*, 843–845, doi:10.1126/science.245.4920.843.
256. Zhang, W.; Li, P.; Yang, F.; Hu, X.; Sun, C.; Zhang, W.; Chen, D.; Tang, B. Dynamic and Reversible Fluorescence Imaging of Superoxide Anion Fluctuations in Live Cells and in Vivo. *J. Am. Chem. Soc.* **2013**, *135*, 14956–14959, doi:10.1021/ja408524j.
257. Kang, D.E.; Lim, C.S.; Kim, J.Y.; Kim, E.S.; Chun, H.J.; Cho, B.R. Two-Photon Probe for Cu²⁺ with an Internal Reference: Quantitative Estimation of Cu²⁺ in Human Tissues by Two-Photon Microscopy. *Anal. Chem.* **2014**, *86*, 5353–5359, doi:10.1021/ac500329k.

258. Wang, X.; Ku, G.; Wegiel, M.A.; Bornhop, D.J.; Stoica, G.; Wang, L. V. Noninvasive Photoacoustic Angiography of Animal Brains in Vivo with Near-Infrared Light and an Optical Contrast Agent. *Opt. Lett.* **2004**, *29*, 730, doi:10.1364/ol.29.000730.
259. Jayabalan, G.S.; Wu, Y.K.; Bille, J.F.; Kim, S.; Mao, X.W.; Gimbel, H. V.; Rauser, M.E.; Fan, J.T. In Vivo Two-Photon Imaging of Retina in Rabbits and Rats. *Exp. Eye Res.* **2018**, *166*, 40–48, doi:10.1016/j.exer.2017.04.009.
260. Smith, A.M.; Mancini, M.C.; Nie, S. Second Window for in Vivo Imaging Andrew. *Nat. Nanotechnol.* **2009**, *4*, 710–711, doi:10.1038/nnano.2009.326.Second.
261. Chung, Y.H.; Cai, H.; Steinmetz, N.F. Viral Nanoparticles for Drug Delivery, Imaging, Immunotherapy, and Theranostic Applications. *Adv. Drug Deliv. Rev.* **2020**, *156*, 214–235, doi:10.1016/j.addr.2020.06.024.
262. Somiya, M.; Liu, Q.; Kuroda, S. Current Progress of Virus-Mimicking Nanocarriers for Drug Delivery. *Nanotheranostics* **2017**, *1*, 415–429, doi:10.7150/ntno.21723.
263. Mizuguchi, H.; Nakanishi, M.; Nakanishi, T.; Nakagawa, T.; Nakagawa, S.; Mayumi, T. Application of Fusogenic Liposomes Containing Fragment A of Diphtheria Toxin to Cancer Therapy. *Br. J. Cancer* **1996**, *73*, 472–476, doi:10.1038/bjc.1996.83.
264. Yang, Y.; Hong, Y.; Nam, G.H.; Chung, J.H.; Koh, E.; Kim, I.S. Virus-Mimetic Fusogenic Exosomes for Direct Delivery of Integral Membrane Proteins to Target Cell Membranes. *Adv. Mater.* **2017**, *29*, doi:10.1002/adma.201605604.
265. Kunisawa, J.; Masuda, T.; Katayama, K.; Yoshikawa, T.; Tsutsumi, Y.; Akashi, M.; Mayumi, T.; Nakagawa, S. Fusogenic Liposome Delivers Encapsulated Nanoparticles for Cytosolic Controlled Gene Release. *J. Control. Release* **2005**, *105*, 344–353, doi:10.1016/j.jconrel.2005.03.020.
266. Bullough, P.A.; Hughson, F.M.; Skehel, J.J.; Wiley, D.C. Structure of Influenza HA at the PH of Membrane Fusion. *Nature* **1994**, *371*, 37–43.
267. Cronin, J.; Zhang, X.-Y.; Reiser, J. Altering the Tropism of Lentiviral Vectors through Pseudotyping. *Curr. Gene Ther.* **2005**, *5*, 387–398,

doi:10.2174/1566523054546224.

268. Liu, X.; Li, Y.; Zhong, Z.; Tan, H.; Lin, H.; Chen, S.; Fu, Y.; Xu, W.; Wei, C. Incorporation of Viral Glycoprotein VSV-G Improves the Delivery of DNA by Erythrocyte Ghost into Cells Refractory to Conventional Transfection. *Appl. Biochem. Biotechnol.* **2017**, *181*, 748–761, doi:10.1007/s12010-016-2246-x.
269. Mangeot, P.-E.; Dollet, S.; Girard, M.; Ciancia, C.; Joly, S.; Peschanski, M.; Lotteau, V. Protein Transfer Into Human Cells by VSV-G-Induced Nanovesicles. *Mol. Ther.* **2011**, *19*, 1656–1666, doi:10.1038/mt.2011.138.
270. Asadikaram, G.; Poustforoosh, A.; Pardakhty, A.; Torkzadeh-Mahani, M.; Nematollahi, M.H. Niosomal Virosome Derived by Vesicular Stomatitis Virus Glycoprotein as a New Gene Carrier. *Biochem. Biophys. Res. Commun.* **2021**, *534*, 980–987, doi:10.1016/j.bbrc.2020.10.054.
271. Montagna, C.; Petris, G.; Casini, A.; Maule, G.; Franceschini, G.M.; Zanella, I.; Conti, L.; Arnoldi, F.; Burrone, O.R.; Zentilin, L.; et al. VSV-G-Enveloped Vesicles for Traceless Delivery of CRISPR-Cas9. *Mol. Ther. - Nucleic Acids* **2018**, *12*, 453–462, doi:10.1016/j.omtn.2018.05.010.
272. Bishnoi, S.; Kumari, A.; Rehman, S.; Minz, A.; Senapati, S.; Nayak, D.; Gupta, S. Fusogenic Viral Protein-Based Near-Infrared Active Nanocarriers for Biomedical Imaging. *ACS Biomater. Sci. Eng.* **2021**, *0*, acsbiomaterials.1c00267, doi:10.1021/acsbiomaterials.1c00267.
273. Lewis, G.N.; Kasha, M. Phosphorescence and the Triplet State. *J. Am. Chem. Soc.* **1944**, *66*, 2100–2116, doi:10.1021/ja01240a030.
274. Tung, C.H.; Mahmood, U.; Bredow, S.; Weissleder, R. In Vivo Imaging of Proteolytic Enzyme Activity Using a Novel Molecular Reporter. *Cancer Res.* **2000**, *60*, 4953–4958.
275. Naidu Bobba, K.; Won, M.; Shim, I.; Velusamy, N.; Yang, Z.; Qu, J.; Kim, J.S.; Bhuniya, S. A BODIPY-Based Two-Photon Fluorescent Probe Validates Tyrosinase Activity in Live Cells. *Chem. Commun.* **2017**, *53*, 11213–11216, doi:10.1039/C7CC05043G.

